Winter 12-5-2013

POLARIZATION-COUPLED TRANSPORT BEHAVIOR IN ULTRATHIN FERROELECTRIC HETEROSTRUCTURES

Haidong Lu
University of Nebraska-Lincoln, s-hlu4@unl.edu

POLARIZATION-COUPLED TRANSPORT BEHAVIOR IN ULTRATHIN FERROELECTRIC HETEROSTRUCTUERS

by

Haidong Lu

A DISSERTATION

Presented to the Faculty of

The Graduate College at the University of Nebraska

In Partial Fulfilment of Requirements

For the Degree of Doctor of Philosophy

Major: Physics and Astronomy

Under the Supervision of Professor Alexei Gruverman

Lincoln, Nebraska

December, 2013

POLARIZATION-COUPLED TRANSPORT BEHAVIOR IN ULTRATHIN FERROELECTRIC HETEROSTRUCTUERS

Haidong Lu, Ph.D.

University of Nebraska, 2013

Adviser: Alexei Gruverman

Ferroelectric polarization-coupled resistive switching behavior in ferroelectric tunnel junctions (FTJs), the tunneling electroresistance (TER) effect, is a recently predicted new phenomenon, which attracts interest due to potential application in the next generation non-volatile ferroelectric random access memories (FeRAMs). In this dissertation, we demonstrate the TER effect in FTJ devices by means of scanning probe microscopy (SPM) techniques. We have investigated several device configurations for enhancement of polarization stability and for demonstration of the resistive switching behavior: (i) using the SPM probe as a top electrode; (ii) using heterostructures with engineered interfacial atomic terminations; (iii) using metal electrodes; (iv) adding an additional polar molecular layer at the interface. Stable and switchable resistance states with a ratio over three orders of magnitude have been achieved in these FTJs. These results are promising for employing FTJs in non-volatile memory and logic devices.

Furthermore, for the first time, ferroelectric polarization reversal by pure mechanical force—a fundamentally new phenomenon—predicted almost 50 years ago, has been demonstrated. We show that the strain gradient generated by an atomic force microscope (AFM) tip pressing onto an ultrathin ferroelectric film can result in polarization reversal in a nanoscale volume without application of an external bias due to the flexoelectric effect. The mechanically generated ferroelectric domains are more

localized than electrically generated domains, enabling much higher density of data storage. Pure mechanical force can therefore be used as a dynamic tool for polarization control and enable applications in which memory bits are written mechanically and read electrically.

Multiferroic materials and magnetoelectric coupling between ferroelectric and ferromagnetic order parameters are attracting great interest both due to the fundamental physical insight that these systems give and due to the vast potential for applications such as the electrical control of magnetism and vice versa. In this dissertation we also demonstrate the existence of a large room-temperature ferroelectric polarization modulation of magnetization at the ferroelectric-ferromagnetic interface upon polarization reversal.

To my parents and my wife

PREFACE

The non-volatile random-access memory (NVRAM) is very important for modern information processing and storage, where non-volatility means that information retains when power is turned off. Currently flash memory is the dominant technology for non-volatile solid state memories, which is based on charge storage in the floating-gate transistors. The main problems of the flash memories are their slow write operation and limited write-erase cycles. An alternative technology is ferroelectric random-access memories (FeRAMs), which is based on information storage in the ferroelectric materials. The advantages of FeRAMs are due to their non-volatility, low power consumption, faster write performance, and greater write-erase cycle lifetimes. However, there are also several limitations, e.g., their relatively complicated structure, their destructive read-out (which requires rewrite after readout, and leads to faster material fatigue), and their low storage density. An improvement in device structure is required for a ferroelectric-based memory technology to compete with other blossoming technologies.

In the meantime, resistive random-access memories (RRAMs) emerged as a competitive candidate for the next generation NVRAM devices. RRAMs are based on the resistive switching phenomenon observed in many transition metal oxides, where the resistance abruptly changes under the action of a strong electric field. The non-volatility and reversibility of the resistance states make this effect suitable for data storage with a simple structure, low power consumption and fast performance.

Recent theoretical calculations predict a specific type of resistive switching phenomenon that is based on quantum tunneling effect through an ultrathin ferroelectric barrier. Such a metal-ferroelectric-metal structure is called a ferroelectric tunnel junction (FTJ), where the tunneling conductance of the junction is coupled to the

polarization orientation: reversal of the polarization in the ultrathin ferroelectric layer leads to a change of the tunneling conductance in the junction—an effect called the tunneling electroresistance (TER) effect. The relative structural simplicity and the capability for non-destructive read-out have made the FTJ an ideal element for ultra-high density memory and logic devices with improved performance.

One of the main objectives of this dissertation is to experimentally demonstrate the polarization-coupled resistive switching behavior in FTJs, and to develop FTJ devices with improved performance that is suitable for memory applications.

Recent experimental developments have made possible fabrication of epitaxial single-crystalline ferroelectric thin films with a thickness down to several unit cells. Stable ferroelectric polarization in these ultrathin ferroelectric films has been demonstrated both theoretically and experimentally. One of the main problem in realization of FTJs is polarization relaxation in FTJ-based ultrathin ferroelectric barriers. In this work, several approaches have been investigated to enhance polarization stability. The first approach involves engineering of atomic terminations at the electrode-ferroelectric interfaces based on first-principle calculations. The second approach involves the use of metal electrodes to provide more effective screening of the depolarizing field. In the third approach, we introduce a polar molecular layer at the electrode-ferroelectric interface to provide additional screening dipoles. Stable and switchable polarization and enhanced electroresistance effects have been achieved in the FTJs.

Flexoelectricity at the nanoscale is another main objective for this dissertation. Electromechanical properties play an essential role in the physics of solids and their practical applications. The most well-known electromechanical coupling properties are piezoelectricity and electrostriction. However, it has become clear that the flexoelectric effect, which is a linear coupling between polarization and strain gradient, can

play a pivotal role, especially in nanoscale devices. Since strain gradient is inversely proportional to relaxation length, which can lead to a strong flexoelectric effect in nanoscale structures. Flexoelectricity is a universal property that is allowed by symmetry in any structure. Therefore, it is more general than piezoelectricity and can exist in all materials. Furthermore, flexoelectricity breaks the inversion symmetry, which offers an additional degree of freedom to control not just polarization magnitude but the polarization orientation. The main purpose of using flexoelectricity in this dissertation is to use the highly amplified and localized strain gradient generated via an atomic force microscope (AFM) tip pressing onto an ultrathin ferroelectric film, for control of polarization and electroresistance effect by pure mechanical force.

Magnetoelectric coupling between ferroelectric and ferromagnetic order parameters offers an additional degree for controlling functional properties, for instance, using electric field to control magnetism (which has recently become a hot research area). In a ferroelectric/ferromagnetic heterostructure, charge screening of ferroelectric polarization influences charge carrier concentration in the ferromagnetic conducting layer. Thus by switching the ferroelectric polarization, the magnetization may also be modulated due to the change in charge carrier density, providing an avenue for realizing electrical control of magnetism.

For a clear view of the organization of this dissertation, a thesis outline is shown below.

Chapter 1 is a general introduction to ferroelectrics.

Chapter 2 is an introduction of experimental techniques, which reviews various scanning probe microscopy (SPM) techniques used in this study with an emphasis on piezoresponse force microscopy (PFM).

Chapter 3 demonstrates polarization-coupled resistive switching behavior in nanometer thick $BaTiO_3$ films by using the conductive SPM probe as top electrode. Simul-

taneous monitoring of polarization reversal and resistive switching has been demonstrated in these FTJs.

Chapter 4 considers the role of interfacial engineering in $SrRuO_3/BaTiO_3/SrRuO_3$ heterostructures in the enhancement of ferroelectric polarization retention. An additional layer of $SrTiO_3$ inserted at the top interface of the heterostructures modifies the interfacial atomic terminations and enhances the remnant polarization.

Chapter 5 describes the use of metal electrodes for enhancement of polarization stability in $Co/BaTiO_3/(La,Sr)MnO_3$ FTJs. Strong retention of the electroresistance effect has been achieved in these junctions. In addition, memrestive (tunable resistance) switching behavior has been demonstrated in these types of heterostructures.

Chapter 6 demonstrates another approach of interface control for enhancement of polarization stability in graphene/$BaTiO_3$/$(La,Sr)MnO_3$ tunnel junctions by adding a polar molecular layer at the graphene-ferroelectric interface. This layer not only stabilizes the ferroelectric polarization, but also significantly enhances the tunneling electroresistance effect.

Chapter 7 deals with mechanical switching of ferroelectric polarization in ultrathin ferroelectrics due to the amplified flexoelectric effect at the nanoscale. The strain gradient generated by pressing the ultra-sharp atomic force microscope (AFM) tip onto a ferroelectric film results in a flexoelectric field higher than the coercive field of the film, yielding polarization reversal by pure mechanical means. In addition, targeted poling of nanoscale areas in graphene/$BaTiO_3$/$(La,Sr)MnO_3$ ferroelectric capacitor structures is realized for the first time.

Chapter 8 presents the work of mechanical control of resistive switching in nanometer thick $BaTiO_3$ tunnel junctions. Polarization-coupled resistive switching is realized by mechanical control of polarization reversal due to the flexoelectric effect. Additional comparison shows an enhancement of electroresistance effect for polarization

switched mechanically compared to polarization switched electrically.

Chapter 9 presents the work of modulation of magnitization in ferromagnetic films upon polarization reversal in ferroelectric/ferromagnetic heterostructures. Reversal of $BaTiO_3$ polarization results in a large modulation of magnetization at the interface in $BaTiO_3$/(La,Sr)MnO_3 heterostructures.

Chapter 10 summarizes the main results of this dissertation and discusses future plans.

ACKNOWLEDGMENTS

I would like to express my sincere appreciation to those who have helped, supported and guided me during my doctoral research studies. Most of the work done during this period is a result of collaboration and efforts of many people, without whom it would certainly not have been possible for me to complete all this work toward a doctoral degree. In addition, I would like to thank the following people who have especially provided me with help for this research.

First of all, I would like to thank my supervisor Prof. Alexei Gruverman for providing me with support, guidance, and being an invaluable mentor during all the research time. His keen insight into physics has strongly inspired me toward solving research problems. Under his guidance I have learned how to look at a research project from the big picture, to have a more profound understanding of the significance and the underlying physics. I have learned how to look into a problem from every angle, and solve it step by step. It simply would not be possible to complete this research work without his guidance and inspiration in every research step. Also, I would like to thank him for leading me to this research career that has challenged, excited and inspired me toward my future research.

I would like to thank all the advisory committee members, Prof. Alexei Gruverman, Prof. Evgeny Tsymbal, Prof. Peter Dowben, Prof. Timothy Gay and Prof. Alexander Sinitskii, for their guidance during this research and reading through of this dissertation.

I would like to thank those who have collaborated with me in this research, in particular, Prof. Evgeny Tsymbal for help with discussion and interpretation of the research results, and for providing theoretical support to the research work, Prof. Chang-Beom Eom of the University of Wisconsin-Madison for providing ferroelectric

samples used in my research, Prof. Alexander Sinitskii and Prof. Xia Hong for help with sample preparation, Prof. Peter Dowben and Prof. Christian Binek for experimental support, Prof. Andrei Sokolov for various helpful discussions, Prof. Gustau Catalan from CIN2 in Barcelona, Spain for providing theoretical modeling and helpful discussions, and all their group members that have participated in this work.

I would also like to thank my current and former group members, Dr. Dong Wu, Dr. Pankaj Sharma, Alex Stamm, Dr. Alexandra Fursina, Dr. Dong Jik Kim, Shijie Li, for all the help, advice, suggestions, useful discussions and good times together. I am especially indebted to Dr. Dong Wu who has guided me with the experimental experiences, and Alex Stamm who spent lots of time reading through this dissertation.

Finally, I would like to express my sincere gratitude to my parents and my wife. I would not have succeeded in pursuing this degree without their support, encourage, and love. I dedicate all my achievements to them.

PUBLICATIONS RELATED TO THIS RESEARCH

1. D. J. Kim, **H. Lu**, S. Ryu, S. Lee, C. W. Bark, C. B. Eom, and A. Gruverman, *Retention of resistance states in ferroelectric tunnel memristors*, Appl. Phys. Lett. **103**, 142908 (2013).

2. J. Chen, **H. Lu**, H.-J. Liu, Y.-H. Chu, S. Dunn, K. Ostrikov, A. Gruverman, and V. Nagarajan, *Interface control of surface photochemical reactivity in ultrathin epitaxial ferroelectric films*, Appl. Phys. Lett. **102**, 182904 (2013).

3. S. Cao, P. Liu, J. Tang, **H. Lu**, C. W. Bark, S. Ryu, C.-B. Eom, A. Gruverman, and P. A. Dowben, *Magnetoelectric coupling at the $EuO/BaTiO_3$ interface*, Appl. Phys. Lett. **102**, 172402 (2013).

4. A. Stamm, D. J. Kim, **H. Lu**, C. W. Bark, C-B. Eom, and A. Gruverman, *Polarization Relaxation Kinetics in Ultrathin Ferroelectric Capacitors*, Appl. Phys. Lett. **102**, 092901 (2013).

5. E. A. Paisley, H. S. Craft, M. D. Losego, **H. Lu**, A. Gruverman, R. Collazo, Z. Sitar, and J. P. Maria, *Epitaxial $PbZr_xTi_{1-x}O_3$ on GaN*, J. App. Phys. **113**, 074107 (2013).

6. **H. Lu**, D. J. Kim, C-W. Bark, S. Ryu, C-B. Eom, E. Y. Tsymbal, and A. Gruverman, *Mechanically-induced Resistive Switching in Ferroelectric Tunnel Junctions*, Nano Lett. **12**, 6289 (2012).

7. D. J. Kim, **H. Lu**, S. Ryu, C-W. Bark, C-B. Eom, E. Y. Tsymbal, and A. Gruverman, *Ferroelectric Tunnel Memristor*, Nano Lett. **12**, 5697 (2012).

8. **H. Lu**, C.-W. Bark, D. Esque de los Ojos, J. Alcala, C. B. Eom, G. Catalan, and A. Gruverman, *Mechanical writing of ferroelectric polarization*, Science **336**, 59 (2012).

9. **H. Lu**, X. Liu, J. D. Burton, C.-W. Bark, Y. Wang, Y. Zhang, D. J. Kim, A. Stamm, P. Lukashev, D. A. Felker, C. M. Folkman, P. Gao, M. S. Rzchowski, X. Q. Pan, C.-B. Eom, E. Y. Tsymbal, and A. Gruverman, *Enhancement of Ferroelectric Polarization Stability by Interface Engineering*, Adv. Mater. **24**, 1209 (2012).

10. **H. Lu**, T. A. George, Y. Wang, I. Ketsman, J. D. Burton, C.-W. Bark, S. Ryu, D. J. Kim, J. Wang, C. Binek, P. A. Dowben, A. Sokolov, C.-B. Eom, E. Y. Tsymbal, and A. Gruverman, *Electric modulation of magnetization at the $BaTiO_3/La_{0.67}Sr_{0.33}MnO_3$ interface*, Appl. Phys. Lett. **100**, 232904 (2012).

11. D. Pantel, **H. Lu**, S. Goetze, P. Werner, D. J. Kim, A. Gruverman, D. Hesse, and M. Alexe, *Tunnel electroresistance in junctions with ultrathin ferroelectric $Pb(Zr_{0.2}Ti_{0.8})O_3$ barriers*, Appl. Phys. Lett. **100**, 232902 (2012).

12. A. Kumar, S. G. Shivareddy, M. Correa, O. Resto, Y. Choi, M. T. Cole, R. S. Katiyar, J. F. Scott, and G. A. J. Amaratunga, **H. Lu** and A. Gruverman, *Ferroelectric-carbon nanotube memory devices*, Nanotechnology **23**, 165702, (2012).

13. S. Kim, Y. Bastani, **H. Lu**, W. P. King, S. Marder, K. H. Sandhage, A. Gruverman, E. Riedo, and N. Bassiri-Gharb, *Direct Fabrication of Arbitrary-Shaped Ferroelectric Nanostructures on Plastic, Glass, and Silicon Substrates*, Adv. Mater. **23**, 3786 (2011).

14. X. Chen, S. Yang, J.-H. Kim, H.-D. Kim, J.-S. Kim, G. Rojas, R. Skomski, **H. Lu**, A. Bhattacharya, T. Santos, N. Guisinger, M. Bode, A. Gruverman, and A. Enders, *Ultrathin $BaTiO_3$ templates for multiferroic nanostructures*, New J. Phys. **13**, 083037 (2011).

15. A. Gruverman, D. Wu, **H. Lu**, Y. Wang, H. W. Jang, C. M. Folkman, M. Ye. Zhuravlev, D. Felker, M. Rzchowski, C. B. Eom, and E. Y. Tsymbal, *Tunneling electroresistance effect in ferroelectric tunnel junctions at the nanoscale*, Nano Lett. **9**, 3539 (2009).

CONFERENCE PRESENTATIONS RELATED TO THIS RESEARCH

1. *Calibration of Flexoelectric Coefficient in Ultrathin Ferroelectric Films*, MRS Spring Meeting, San Francisco, CA, Apr. 2013.

2. *Mechanical Writing of Ferroelectric Polarization*, MRS Fall Meeting, Boston, MA, Dec. 2012.

3. *Reversal of Ferroelectric Polarization in Ultrathin Ferroelectrics by Mechanical Means*, MRS Fall Meeting, Boston, MA, Dec. 2011.

4. *Electric Modulation of Magnetization in Ferro-electric/ferromagnetic Hetero-junctions*, ISIF Meeting, Cambridge, UK, Aug. 2011.

5. *Interface Engineering for Polarization Retention Enhancement in Ultrathin $SrRuO_3/BaTiO_3/SrRuO_3$ hetrostructures*, MRS Spring Meeting, San Francisco, CA, Apr. 2011.

Contents

Chapter 1

Introduction to Ferroelectricity

Ferroelectric materials are characterized by a spontaneous electric polarization that can be reversed by the application of an external electric field—a property that is referred to as ferroelectricity. Ferroelectric materials have already found large areas of applications in ferroelectric capacitors, piezoelectric transducers, non-volatile random access memories, medical ultrasound imaging devices, actuators, and new microelectro-mechanical systems (MEMS), etc. During the past two decades, revolutionary breakthroughs in new functionalities of ferroelectrics have been explored both from the perspective of theory and of experiment [1]. First principles approaches now allow accurate, quantitative predictions of material properties, and single crystalline thin films are now routinely available for fundamental studies of these materials. The general field of integrated ferroelectrics is not limited to conventional applications, but includes new developments in ferroelectric tunnel junctions [2, 3], ferroelectric-gated field effect transistors [4, 5], electrocaloric cooling devices [6, 7], THz emitters [8, 9], domain nanoelectronics [10], flexible polymetric ferroelectrics [11, 12], and photovoltaics [13, 14], etc. New functionalities, such as ferroelectricity in ultrathin ferroelectric films [15, 16, 17], electroresistance effect in tunnel junctions [18], domain

wall conductivity [10], multiferroicity and magnetoelectric coupling [19], pyroelectrics, etc. are under intensive investigation. Ferroelectrics have become one of the most important groups of functional materials that are not only of fundamental importance but also of practical interest for device applications.

1.1 History of Ferroelectrics

Ferroelectricity was first discovered in 1921 by Valasek who was investigating the dielectric properties of Rochelle salt ($KNaC_4H_4O_6{\cdot}4H_2O$) [20]. One of the major step in ferroelectricity came in 1940's when barium titanate ($BaTiO_3$) was discovered during World War II in the United States, Russia, and Japan, and soon found to be ferroelectric [21, 22]. $BaTiO_3$ became popular due to its simple perovskite structure and sizeable spontaneous polarization (~15 $\mu C/cm^2$) and ultimately gained the title of a "classical" ferroelectric. Devonshire developed a phenomenological model of ferroelectrics on the basis of the electromechanical, structural and thermal properties of $BaTiO_3$ in 1951 [23]. This approach built upon the earlier ideas of Landau which invoked the point group symmetry and nonlinear elasto-dielectric coupled interactions with electrostriction and piezoelectric coefficients. The resulting Landau-Devonshire theory of ferroelectrics is, to this day, a very useful tool for understanding ferroelectric properties. Since then, many other ferroelectric materials have been discovered; the most important of which include lead titanate ($PbTiO_3$), lead zirconate titanate ($Pb(Zr,Ti)O_3$), and lithium niobate ($LiNbO_3$), which are now widely used in piezoelectric applications, non-volatile memories and pyroelectric applications.

In recent years, with the advances in processing of high-quality thin films, epitaxial ferroelectric films have been successfully grown on various types of substrates with variable in-plane strain mismatches for allowing tuning of ferroelectric proper-

ties. Layer-by-layer growth has enabled realization of ferroelectric superlattices and interface control, providing additional freedom for tuning ferroelectric properties and functionalities. Also, with the general trend of decreasing device size, the ferroelectric size effect has generated additional research interest and has led to new application possibilities in nanotechnology.

1.2 Ferroelectric Properties

1.2.1 Polarization reversal and hysteresis loops

Ferroelectric polarization arises from a permanent electric dipole moment in the crystal structure due to the off-centering of cations and anions, and thus only exists in non-centrosymmetric crystal structures. The essential property of ferroelectrics is the electrically switchable ferroelectric polarization and its hysteretic behavior as a function of applied electric field.

A typical ferroelectric polarization hysteresis loop (P–E hysteresis loop), where polarization (P) is plotted as a function of electric field (E) is shown in Fig. 1.1. Suppose we start with a material where there are many polarization domains which are aligned randomly. When we start to apply an electric field (point A), the initial net polarization is zero. If we apply a small electric field, such that it is not able to switch domain alignment, then the material will behave as a normal dielectric, P increases nearly linearly with E (path AB). As E is increased, we start to flip domains and rapidly increase P (path BC). At even higher electric field when all domains are switched, polarization reaches saturation (path CD). Now when the electric field is gradually reduced, polarization remains non-zero even without electric field (path DE). The value of polarization at zero field is called the remnant polarization

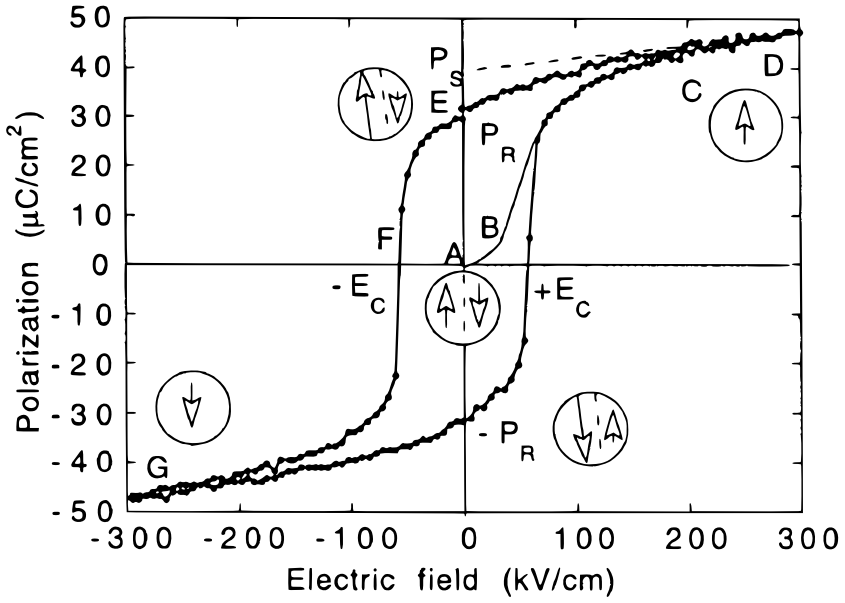

Figure 1.1: Ferroelectric P–E hysteresis loop. Figure adapted from ref. [24]

(P_r), and the value of polarization extrapolated back from the saturation limit is the spontaneous polarization (P_s). Reversal of the field, E, will eventually remove all polarization (path EF). The field required to bring the polarization to zero is known as the coercive field (E_c). Further increase in the reverse field will completely reverse the polarization (path FG). Upon removal of the electric field (zero field), the polarization will acquire a $-P_r$ value. Application of the positive field will switch the polarization back again. Thus a complete polarization hysteresis loop is formed.

The ferroelectric hysteresis arises from the energy needed to reverse the direction of electric dipoles, which represent two metastable states that can exist in ferroelectric materials, namely, polarization up and polarization down. These two states can be used in information storage. An ideal hysteresis loop is symmetrical so that $+E_c = -E_c$ and $+P_r = -P_r$. The coercive field, spontaneous and remanent polarization and shape of the loop may be affected by many factors including the thickness of the film, the presence of charged defects, mechanical stresses, preparation conditions, and

thermal treatment. The scaling of coercive field with film thickness is described by the Kay-Dunn Law, $E_c(d) \propto d^{-2/3}$, where d is the film thickness [25]. This law works pretty well for a great variety of ferroelectrics, and it has been used successfully to describe the thickness dependence of the coercive field in ferroelectric films ranging from hundreds of microns down to nanometers [26].

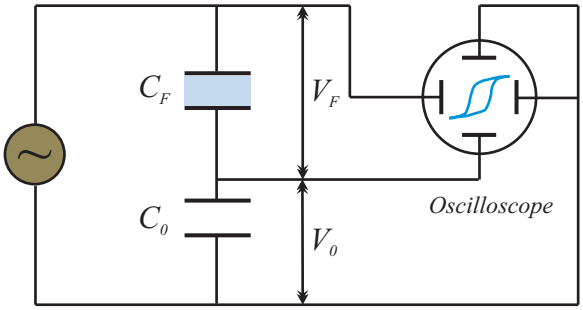

Figure 1.2: Sawyer-Tower method for measuring polarization–electric field (P–E) characteristics.

The P–E hysteresis loop is the characteristic of ferroelectricity. It is usually measured by the Sawyer-Tower method [27] as shown in Fig. 1.2, or by integration of the transient switching current. In the Sawyer-Tower method, an AC voltage is applied to the ferroelectric capacitor, and the switching charge due to polarization reversal is detected by measuring a voltage drop across a large reference capacitor placed in series with the sample. In the transient current method, switching charge is measured by integrating the current across a loading resistor in series with the ferroelectric sample induced by an external voltage pulse. The total current consists of two parts: dielectric charging current and transient polarization switching current. Integration of the meassured current gives:

$$\int_0^{t_s} i(t)\mathrm{d}t = \epsilon E A + 2P_r A, \tag{1.1}$$

where t_s is the switching time, ϵ the dielectric constant and A the area of electrodes.

This type of approach can be used to study the switching dynamics of a ferroelectric film. A description of switching models will be presented in section 1.3.

1.2.2 Piezoelectricity and electromechanical hysteresis

Another characteristic feature of ferroelectrics is their piezoelectric behavior. Piezoelectricity is a linear electromechanical coupling between the mechanical and the electrical state in crystalline materials without inversion symmetry. Piezoelectric materials exhibit both a direct piezoelectric effect, where an electrical charge is generated by an applied mechanical force, and a converse piezoelectric effect, where an applied electric field induces mechanical strain. Converse piezoelectric effect is the physical basis of piezoresponse force microscopy (PFM) developed for visualization and manipulation of ferroelectric domain structures, which will be discussed in Chapter 2.

For the direct piezoelectric effect, the relationship between stress and the resulting electric polarization can be described as

$$P_i = d_{ijk}\sigma_{jk}, \tag{1.2}$$

where P_i is the polarization; d_{ijk} is the direct piezoelectric coefficients, and σ_{ij} is the stress. For the converse piezoelectric effect, the strain (s_{ij}) developed in a piezoelectric material is related to the applied electric field as:

$$s_{ij} = d^t_{ijk}E_k, \tag{1.3}$$

where t denotes the transposed matrix. The piezoelectric coefficients d for the direct and converse piezoelectric effects are thermodynamically identical, i.e. $d_{ijk} = d^t_{ijk} =$

d_{kij}. The piezoelectric coefficient d can be either positive or negative. It is common to call a piezoelectric coefficient measured in the direction of an applied field the longitudinal coefficient, and that measured in the direction perpendicular to the field the transverse coefficient. Other piezoelectric coefficients are known as shear coefficients.

In addition to the P–E hysteresis loop, polarization switching by an electric field in ferroelectric materials leads to a strain–electric field (s–E) hysteresis (Fig. 1.3) due to the piezoelectric effect. The strain hysteresis loop is due to the converse

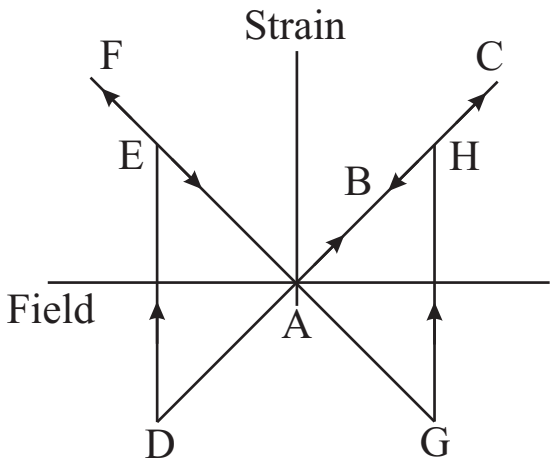

Figure 1.3: Strain–electric field s–E hysteresis loop (butterfly loop) in ferroelectrics.

piezoelectric effect and polarization switching in the ferroelectric film as a function of electric field. Increase of the electric field from zero (A-B-C in Fig. 1.3) leads to a monotonically increasing strain, followed by a monotonic decrease in strain upon decrease of the electric field (C-B-A-D). At point D, due to polarization reversal, the piezoelectric coefficient changes sign, so that the strain jumps from point D to E, and then moves along E-F upon continued decrease of the field. Increasing the field again, symmetrically reduces the strain (F-E-A-G) until polarization reversal at point G, which leads to a jump to point H. Continued increase of electric field to point C, and then decrease (C-B-A) is monotonic due to a consistent.

This electromechanical hysteresis loop is a reflection of ferroelectric polarization switching, which can be used for studying ferroelectric switching behavior, such as coercive fields, imprint fields, spatial switching inhomogeneity, etc.

1.2.3 Ferroelectric phase transition

Ferroelectric materials generally undergo a transition from the ferroelectric phase to a paraelectric phase upon changing temperature. Above a certain temperature (the critical temperature, T_c), the ferroelectric crystal loses spontaneous polarization and becomes paraelectric. This change in ferroelectric properties is associated with a change in the internal order of the crystal. Phase transitions are usually described by Landau's phenomenological theory based on symmetry principles [28]. A Landau theory of ferroelectric phase transitions was developed by Devonshire [23] and Ginzburg [29], and is referred to as Landau-Ginzburg-Devonshire (LGD) theory. For ferroelectrics, polarization (P) is used as the order parameter for phase transition analysis. There are two common types of phase transitions which are distinguished based upon how the order parameter changes during the transition. A first order transition is one which has a discontinuity in the order parameter itself, while a second order transition is one which has a discontinuity in the first derivative of the order parameter. Figure 1.4 illustrates the typical behavior of first and second order phase transitions.

In the LGD theory, the free energy can be expressed as:

$$\Delta G = \frac{1}{2}\alpha(T - T_0)P^2 + \frac{1}{4}\beta P^4 + \frac{1}{6}\gamma P^6, \tag{1.4}$$

where P is polarization, T_0 the Curie temperature, and α, β and γ are the expansion coefficients. In all known ferroelectrics, $\alpha > 0$ and $\gamma > 0$. These coefficients may

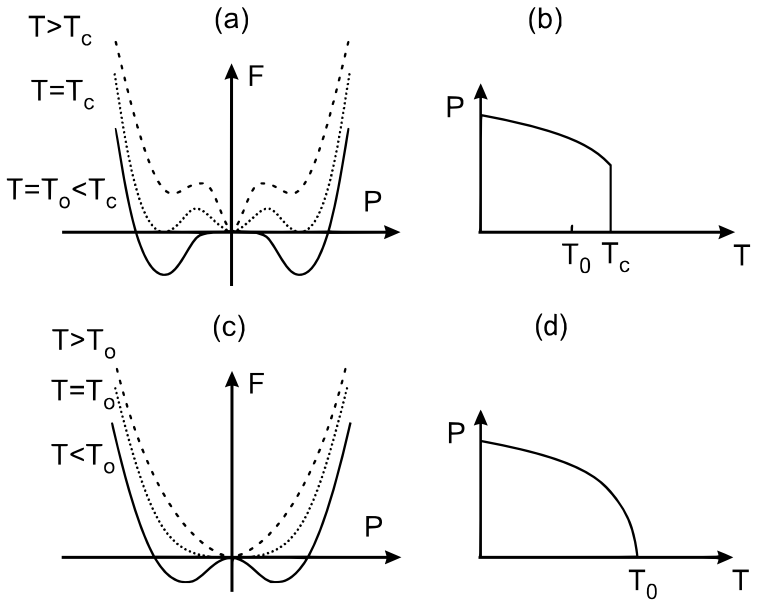

Figure 1.4: (a, b) First-order phase transition. (a) Free energy as a function of the polarization at $T > T_c$, $T = T_c$, and $T = T_0 < T_c$; (b) Spontaneous polarization $P_r(T)$ as a function of temperature. (c, d) Second-order phase transition. (c) Free energy as a function of the polarization at $T > T_0$, $T = T_0$, and $T < T_0$; (d) Spontaneous polarization $P_r(T)$ as a function of temperature.

be obtained experimentally or from *ab-initio* simulations. For ferroelectrics with a first order phase transition $\beta < 0$, and a second order phase transition $\beta > 0$. The minimum of free energy represents a stable phase of the system. At the minimum, the derivative of the free energy is zero, i.e.:

$$\frac{\partial \Delta G}{\partial P} = \alpha(T - T_0)P + \beta P^3 + \gamma P^5 = 0. \tag{1.5}$$

For a second order transition ($\beta > 0$), above T_0, the minimum of free energy occurs at $P = 0$, which means that the system is in paraelectric phase with no spontaneous polarization, while below T_0, the free energy in Eq. 1.4 has the shape of a double well potential with two free energy minima at $P = \pm P_s$, where P_s is the spontaneous polarization, and the system is in the ferroelectric phase. The spontaneous polarization,

P_s, is obtained from the solution of Eq. 1.5:

$$P_s = \sqrt{\frac{1}{2\gamma}[-\beta + \sqrt{\beta^2 - 4\alpha\gamma(T - T_0)}]}. \tag{1.6}$$

From Landau's phenomenological description, there is a phase transition taking place at temperature $T_c = T_0$, where the system goes from paraelectric phase to ferroelectric phase when decreasing temperature from above T_c to below T_c. At $T = T_c$, $P_s = 0$, which shows that the second order transition is continuous (Fig. 1.4(d)).

For a first order transition ($\beta < 0$), T_0 is different from the phase transition temperature T_c. Below $T = T_0 + \beta^2/4\alpha\gamma$ the free energy has two minima at $P = \pm P_s$ from Eq. 1.6, and one minimum at $P = 0$, where $\Delta G = 0$. The phase transition happens when the two minima go below zero, i.e. $\Delta G = 0$:

$$\Delta G = \frac{1}{2}\alpha(T_c - T_0)P_s^2 + \frac{1}{4}\beta P_s^4 + \frac{1}{6}\gamma P_s^6 = 0. \tag{1.7}$$

Solving Eq. 1.7, we get the actual phase transition at

$$T_c = T_0 + \frac{3}{16}\frac{\beta^2}{\alpha\gamma}. \tag{1.8}$$

Above T_c, the minimum of free energy is at $P = 0$, where the system is in paraelectric phase, while below T_c, the minimum of free energy goes to two minima at $P = \pm P_s$, where the system is in the ferroelectric phase. At transition temperature $T = T_c$, $P_s = \pm[3/4(-\beta/\gamma)]^{1/2}$, which shows a discontinuity for first order transition (Fig. 1.4(b)).

Near the Curie temperature T_0, the elastic, dielectric, optical and thermal properties of the material behave anomalously due to the distortion in the crystal as the phase transition occurs. The extremely high value of dielectric constant (ϵ_r) in the neighborhood of T_0 is known as the dielectric anomaly. For $T > T_0$, the behavior of

the dielectric constant is described by the Curie-Weiss relation:

$$\epsilon = \epsilon_0 + \frac{C}{T - T_0}, \tag{1.9}$$

where C is the Curie constant. This law predicts a singularity in the dielectric constant at $T = T_0$.

1.2.4 Ferroelectric domains and domain walls

In real ferroelectrics, the different polarization directions are usually energetically equivalent. When the sample is cooled down from the paraelectric phase, there are usually small regions with different polarity called ferroelectric domains, and the boundaries between adjacent domains are called domain walls. Depolarizing field (E_d) due to surface polarization charges is one of the main reasons for development of domains. The depolarizing field in a typical ferroelectric is an order of magnitude larger than the typical coercive field. So if the surface charges are not properly compensated, the depolarizing field will make ferroelectricity unstable. The depolarizing field in ferroelectrics is usually screened by surface screening charges provided by metal electrodes or ionic species from the ambient environment.

The formation of ferroelectric domains will further minimize the electrostatic energy of depolarizing fields. Domain size is determined by the competition between the energy of the domains and the energy of the domain walls. The energy density of the domains is proportional to the domain size: $\varepsilon = Uw$, where U is the volume energy density of the domain and w is the domain width. Smaller domains, therefore, have smaller energies, but increasing the number of domain walls is also energetically costly. The domain walls' energy density per unit area of thin film is $\varepsilon = \sigma d/w$, where σ is the energy density per unit area of the wall, and d is the sample thickness.

Adding up the energy costs of domains and domain walls, and minimizing the total energy with respect to the domain size, leads to the famous Kittel's law describing the square root thickness dependence of domain width [30, 31]:

$$w = \sqrt{\frac{\sigma}{U}d}. \tag{1.10}$$

In reality, for domain walls with a finite thickness δ, the square root dependence can be rewritten as [32]:

$$\frac{w^2}{\delta d} = G, \tag{1.11}$$

where G is a universal dimensionless constant [10].

1.3 Polarization Switching Mechanism

The polarization switching in ferroelectric materials is a multiple step process which includes the initial domain nucleation and the following forward and lateral domain wall motion (expansion) upon application of an external electric field. Investigation of polarization switching dynamics provides information for understanding the switching mechanisms in ferroelectrics. Theoretically, there are several models describing switching dynamics in different switching conditions: Kolmogorov-Avrami-Ishibashi (KAI) model and nucleation-limited switching (NLS) model.

The KAI model [33] considers ferroelectric domains, initiated from independent nucleation centers, growing unrestrictedly under the action of the applied electric field. It is assumed within this model that the nucleation is deterministic and occurs at predefined places, i.e., nucleation is inhomogeneous. At the early stages of switching, the appeared domains grow without overlapping, so that the volume where the polarization is reversed can be found as the sum of those of the individual do-

mains. However, when domain overlapping occurs, the switched volume requires an additional mathematical treatment. The KAI model predicts that the normalized switched polarization charge p as a function of time may be expressed as [33, 34]:

$$p(t) \equiv \frac{\Delta P(t)}{2P_s} = 1 - \mathrm{e}^{-(t/t_s)^n}, \tag{1.12}$$

where ΔP and P_s are switched polarization and spontaneous polarization, respectively; n is the dimensionality of the growth, and t_s is the characteristic switching time. In this model, t_s is assumed to be only dependent on the electric field, $t_s \propto \mathrm{e}^{\alpha/E}$, with α being the activation field.

The NLS model was developed by Tagantsev in 2002 [35] and independently by Du and Chen in 1998 [36]. It deals with a system where the switching is dominated by nucleation, which means that the system is regarded as an ensemble of independent microscopic regions where the switching process developed independently. The switching kinetics deals with the distribution of nuclei instead of domain wall motion. Since the waiting times for the first nucleation for these different regions are different, there is a distribution of local characteristic nucleation times t_s, $F(\log t_s)$. The normalized time dependent switched polarization charge is therefore:

$$p(t) = 1 - \int_{-\infty}^{\infty} F(\log t_s)\mathrm{e}^{-(t/t_s)^n} d(\log t_s). \tag{1.13}$$

Experimentally, the distribution function $F(\log t_s)$ shows a Lorentzian distribution [37, 38].

1.4 Perovskite Ferroelectrics

Perovskite materials have the same type of crystal structure as calcium titanate ($CaTiO_3$). Perovskite structure can be expressed as ABO_3, where A is one of the cation at eight corners of the psudocubic structure, and B is a different cation, commonly a transition metal, in the cubic center with six face centered oxygen anions forming a BO_6 octahedron (Fig. 1.5). Off-centering of the B cation within its oc-

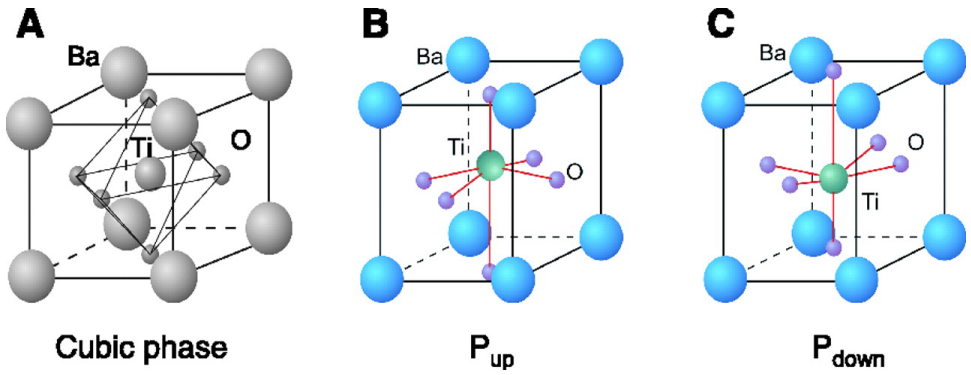

Figure 1.5: Crystal structure of the perovskite ferroelectric $BaTiO_3$. (A) High temperature, paraelectric, cubic phase. (B and C) Room temperature, ferroelectric, tetragonal phases, showing up and down polarization variants. The atomic displacements are scaled to be clearly visible. Figure adapted from ref. [39].

tahedron in a metastable bonding pattern results a net electric dipole, which is responsible for ferroelectricity in perovskite structures. Most of the perovskites are not ferroelectrics, as most of them undergo octahedral rotation distortions that suppress ferroelectricity. Examples of perovskite ferroelectrics include $BaTiO_3$, $PbTiO_3$, $Pb(Zr_xTi_{1-x})O_3$, $LiNbO_3$, $BiFeO_3$, etc.

Barium titanate ($BaTiO_3$) is a commonly studied prototype ferroelectric material. It is ferroelectric below Curie temperature of 120°C, with a spontaneous polarization about 15 $\mu C/cm^2$ and a very high dielectric constant of a few thousands at room temperature. At 120°C $BaTiO_3$ undergoes a first order phase transition from paraelectric cubic structure (space group $Pm\bar{3}m$) to ferroelectric tetragonal structure

(space group $P4mm$), with spontaneous polarization along one of the [001] directions in the pseudocubic structure. There are structural phase transitions at 5°C from high temperature tetragonal structure to low temperature orthorhombic structure (space group $Amm2$) with spontaneous polarization along one of the [011] directions, and at −90°C from orthorhombic structure to low temperature rhombohedral structure (space group $R3m$) with spontaneous polarization along one of the [111] directions.

Lead titanate ($PbTiO_3$) has a similar perovskite structure as $BaTiO_3$. It has a second order phase transition at Curie temperature 490°C, from high temperature cubic phase to low temperature tetragonal phase.

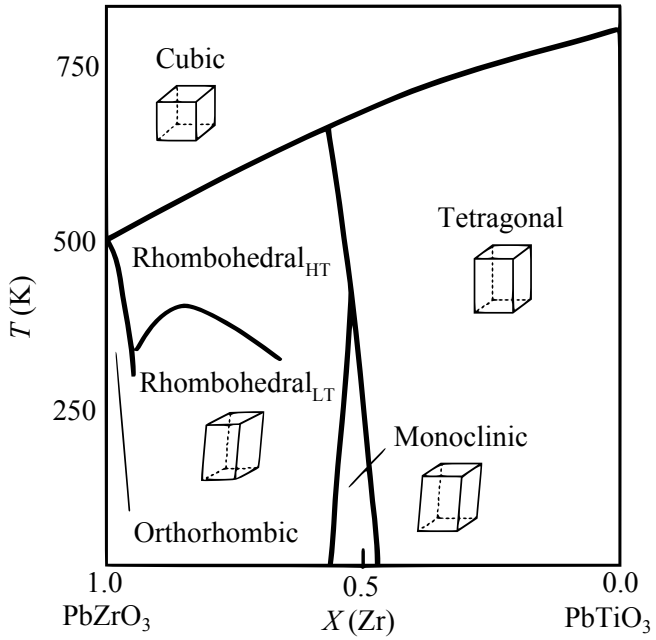

Figure 1.6: Phase diagram of $Pb(Zr_xTi_{1-x})O_3$.

Lead Zirconate Titanate ($Pb(Zr_xTi_{1-x})O_3$) is one of the most widely used ferroelectric materials for piezoelectric transducers, memory devices, etc. It has a perovskite structure with Zr^{4+} and Ti^{4+} ions randomly distributed in the B sites. The variation in composition by Zr doping level x greatly changes the properties and structures, as shown in the phase diagram in Fig. 1.6. Below the Curie temperature,

the crystal structure varies between orthorhombic, rhombohedral, monoclinic, and tetragonal strucures, depending on Zr doping level. The phase separation boundary is called a morphotropic phase boundary (MPB).

1.5 Applications

As mentioned at the beginning of this chapter, ferroelectric materials have already found applications in various fields due to their unique properties like dielectric, piezoelectric, pyroelectric and electro-optic properties. Here we will briefly discuss some of the applications.

One of the most prominent applications of ferroelectrics is in data storage. Ferroelectric random access memory (FeRAM) is a type of random access memory (RAM) similar in construction to dynamic random access memory (DRAM), except it utilizes a ferroelectric layer instead of a dielectric layer to achieve non-volatility. FeRAM makes use of the switchable spontaneous polarization, i.e., polarization up and polarization down in the unit cell which is referred to as "0" and "1", respectively. Currently, lead zirconate titanate and layer strontium bismuth tantalate are employed in ferroelectric RAMs [40, 41]. The FeRAM cell design is based on a capacitor structure

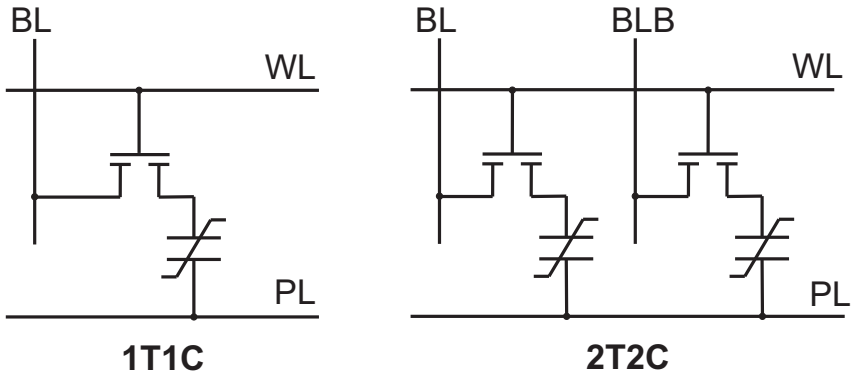

Figure 1.7: Schematic diagram of 1T1C (left) and 2T2C (right) FeRAM bit cells.

integrated with a transistor, i.e. a 1T1C or 2T2C architecture as shown in Fig. 1.7, where BL denotes Bit Line, WL denotes Word Line, PL denotes Plate Line, BLB denotes complementary Bit Line and FE denotes Ferroelectric capacitor. In addition to non-volatility, FeRAMs have a high writing speed, low energy consumption in comparison to conventional RAMs.

Another application area is in sensors, actuators, and microelectro-mechanical systems (MEMS) due to the fact that ferroelectric materials are required by symmetry considerations to also be piezoelectric. Piezoelectric sensors convert a mechanical pressure signal into an electrical signal that can be read by electronic devices. Detection of pressure variations in the form of sound is the most common sensor application, e.g. piezoelectric microphones, and piezoelectric pickups for acoustic-electric guitars. Piezoelectric sensors especially are used with high frequency sound in ultrasonic transducers for medical imaging. Piezoelectric actuators convert a voltage signal into mechanical displacement with better-than-μm precision, making piezo crystals the most important tool for positioning objects with extreme accuracy. It is also the basis of a number of scientific instrumental techniques with atomic resolution, the scanning probe microscopies (SPMs) that will be discussed in Chapter 2.

References

[1] M. Dawber, K. M. Rabe, and J. F. Scott, Rev. Mod. Phys. **77**, 1083 (2005).

[2] E. Y. Tsymbal and H. Kohlstedt, Science **313**, 181 (2006).

[3] A. Chanthbouala, A. Crassous, V. Garcia, K. Bouzehouane, S. Fusil, X. Moya, J. Allibe, B. Dlubak, J. Grollier, S. Xavier, C. Deranlot, A. Moshar, R. Proksch, N. D. Mathur, M. Bibes, and A. Barthélémy, Nat. Nanotechnol. **7**, 101 (2012).

[4] J. F. Scott and C. A. Paz De Araujo, Science **246**, 1400 (1989).

[5] E. Tokumitsu, R. I. Nakamura, and H. Ishiwara, IEEE Electron Device Lett. **18**, 160 (1997).

[6] A. S. Mischenko, Q. Zhang, J. F. Scott, R. W. Whatmore, and N. D. Mathur, Science **311**, 1270 (2006).

[7] A. S. Mischenko, Q. Zhang, R. W. Whatmore, J. F. Scott, and N. D. Mathur, Appl. Phys. Lett. **89**, 242912 (2006).

[8] K. Takahashi, N. Kida, and M. Tonouchi, Phys. Rev. Lett. **96**, 117402 (2006).

[9] J. F. Scott, H. J. Fan, S. Kawasaki, J. Banys, M. Ivanov, A. Krotkus, J. Macutkevic, R. Blinc, V. V. Laguta, P. Cevc, J. S. Liu, and A. L. Kholkin, Nano Lett. **8**, 4404 (2008).

[10] G. Catalan, J. Seidel, R. Ramesh, and J. F. Scott, Rev. Mod. Phys. **84**, 119 (2012).

[11] A. V. Bune, V. M. Fridkin, S. Ducharme, L. M. Blinov, S. P. Palto, A. V. Sorokin, S. G. Yudin, and A. Zlatkin, Nature **391**, 874 (1997).

[12] T. Furukawa, Phase Transit. **18**, 143 (1989).

[13] D. Daranciang, M. Highland, H. Wen, et al., Phys. Rev. Lett. **108**, 087601 (2012).

[14] R. M. Swanson, Science **324**, 891 (2009).

[15] D. D. Fong, G. B. Stephenson, S. K. Streiffer, J. A. Eastman, O. Auciello, P. H. Fuoss, and C. Thompson, Science **304**, 1650 (2004).

[16] S. K. Streiffer, J. A. Eastman, D. D. Fong, C. Thompson, A. Munkholm, M. V. R. Murty, O. Auciello, G. R. Bai, and G. B. Stephenson, Phys. Rev. Lett. **89**, 067601 (2002).

[17] J. Junquera and Ph. Ghosez, Nature **422**, 506 (2003).

[18] E. Y. Tsymbal, A. Gruverman, V. Garcia, M. Bibes, and A. Barthélémy, MRS Bull. **37**, 138 (2012).

[19] W. Eerenstein, N. D. Mathur, and J. F. Scott, Nature **442**, 759 (2006).

[20] J. Valasek, Phys. Rev. **17**, 475 (1921).

[21] A. Von Hippel, R. G. Breckenridge, F. G. Chesley, and L. Tisza, Ind. Eng. Chem. **38**, 1097 (1946).

[22] B. Wul and J. M. Goldman, C.R. Acad. Sci. URSS **51**, 21 (1946).

[23] A. F. Devonshire, Phil. Mag. **42**, 1065 (1951).

[24] D. Damjanovic, Rep. Prog. Phys. **61**, 1267 (1998).

[25] H. F. Kay and J. W. Dunn, Philos. Mag. **7**, 1962 (1962).

[26] J. F. Scott, J. Appl. Phys. **88**, 6092 (2000).

[27] C. B. Sawyer and C. H. Tower, Phys. Rev. **35**, 269 (1930).

[28] L. D. Landau, Phys. Z. Sowjet. **11**, 545 (1937).

[29] V. Ginzburg, Zh. Dksp. Teor. Fiz. **15**, 739 (1945).

[30] L. Landau and E. Lifshitz, Phys. Z. Sowjet. **8**, 153 (1935).

[31] C. Kittel, Phys. Rev. **70**, 965 (1946).

[32] J. F. Scott, J. Phys. Condens. Matter **18**, R361 (2006).

[33] Y. Ishibashi and Y. Takagi, J. Phys. Soc. Jpn. **31**, 506 (1971).

[34] H. Orihara, S. Hashimoto, and Y. Ishibashi, J. Phys. Soc. Jpn. **63**, 1031 (1994).

[35] A. K. Tagantsev, I. Stolichnov, N. Setter, J. S. Cross, and M. Tsukada, Phys. Rev. B **66**, 214109 (2002).

[36] X. Du and I.-W. Chen, Mater. Res. Soc. Symp. Proc. **493**, 311 (1998).

[37] J.-Y. Jo, H.-S. Han, J.-G. Yoon, T.-K. Song, S.-H. Kim, and T.-W. Noh, Phys. Rev. Lett. **99**, 267602 (2007).

[38] A. Gruverman, D. Wu, and J. F. Scott, Phys. Rev. Lett. **100**, 097601 (2008).

[39] C. H. Ahn, K. M. Rabe, and J.-M. Triscone, Science **303**, 488 (2004).

[40] H. Ishiwara, M. Okuyama, and Y. Arimoto, Topics Appl. Phys. **93**, 139 (2004).

[41] H. Kohlstedt, Y. Mustafa, A. Gerber, A. Petraru, M. Fitsilis, R. Meyer, U. Böttger, and R Waser, Microelec. Engg. **80**, 296 (2005).

Chapter 2

Experimental Techniques

Various types of scanning probe microscopy (SPM) techniques have been utilized for this research for the characterization and manipulation of ferroelectric and electronic transport properties of ferroelectric heterostructures. Here, we briefly describe these SPM techniques, which include atomic force microscopy (AFM), piezoresponse force microscopy (PFM), conductive atomic force microscopy (C-AFM), and electrostatic force microscopy (EFM).

2.1 Scanning Probe Microscopy

2.1.1 Introduction

SPM are techniques which uses a very fine probe which scans over a sample surface and measures a certain property of that surface by detecting various types of probe-sample interactions. They have become a mainstream technique of nanoscience and nanotechnology due to their ability to image materials at the nanometer and atomic scales and manipulate their properties thereby opening a door to the nanoworld and allowing deeper understanding of material functionality and interactions [1]. These

techniques have an extremely broad range of applications in nanoscale electrical, magnetic, optical and mechanical properties.

The first SPM technique, scanning tunneling microscopy (STM), was invented at the IBM Research Lab in 1981 by Binnig and Rohrer [2], who share the 1986 Nobel Prize in physics for this invention. STM is based on the quantum tunneling phenomenon. It works by scanning a very sharp metal wire tip (ultimately, reducing to a single atom at the tip apex), over a conductive surface. Bringing the electrically biased tip very close to the surface, typically several Å, results in tunneling current flowing from the tip to sample surface. The tip-sample vacuum gap plays the role of a potential barrier. From quantum mechanics, it is known that there is a non-zero probability for electrons to overcome this barrier and tunnel through the vacuum gap. The tunneling current is exponentially dependent on the barrier thickness (tip-sample separation):

$$I \propto V\rho_s(E_f)e^{-2\kappa z}, \tag{2.1}$$

where I is the tunneling current; V the applied voltage; $\rho_s(E_f)$ the local density of states (LDOS) near the Fermi level of the sample; κ the wave vector related to the energy of electrons and barrier hight, and z the tip-sample barrier distance. A feedback loop constantly monitors the tunneling current and makes adjustments to the tip-sample distance to maintain a constant tunneling current. These adjustments are recorded and presented as a two-dimensional surface topographic image when the tip scans over the sample surface.

2.1.2 Atomic Force Microscopy

STM became the first instrument to generate real-space images of surfaces with atomic resolution by precisely positioning the tip in three dimensions [3]. The main limitation

of STM is that it is applicable only to conducting or semiconducting samples. In 1986, Binnig, Quate and Gerber invented the first atomic force microscope (AFM) [4]. Instead of using tunneling *current* for feedback control, AFM senses the tip-sample interaction *forces* to determine the tip-sample separation, which can be used for imaging both conductive and non-conductive material surfaces with nanoscale resolution. Since then, various AFM-based techniques have been developed, with the ability to sense and manipulate electrical, magnetic or mechanical properties of materials.

AFM also relies on a sharp tip that is scanned over a surface. This tip is mounted on a cantilever that can detect forces down to the pN range by monitoring the deflection of the cantilever, which can be done with sub-Å precision. A typical set up

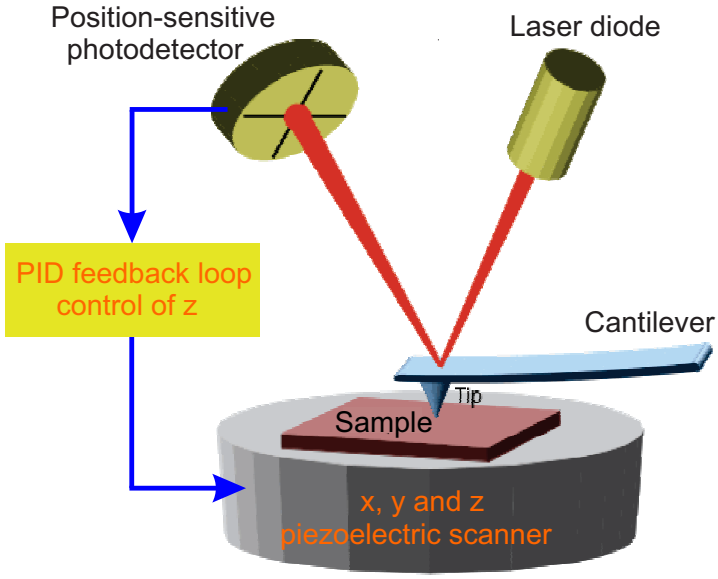

Figure 2.1: Schematic of basic AFM set-up.

of an AFM system is shown in Fig. 2.1. It consists of a cantilever with a sharp tip at its end, a scanner with a three-dimensional positioning system, a position-sensitive photo-detector for sensing the cantilever deflection, and an electrically-controlled feedback loop system for z positioning control.

AFM cantilevers with a tip curvature radius of several nanometers are typically made of silicon or silicon nitride. When the tip is brought close to a sample surface, the tip-sample interaction forces lead to deflection of the cantilever according to Hooke's law. There are many different types of forces that can be measured in AFM, depending on a specific situation: elastic forces, van der Waals forces, friction forces, capillary forces, electrostatic forces, magnetic forces, etc. Typically the cantilever deflection is measured by reflecting a laser off the back of the cantilever onto an array of photodiodes. A feedback loop maintains a constant tip-sample force by adjusting the z position. Traditionally, the sample is mounted on a piezoelectric tube that can move the sample in z direction for maintaining a constant force, and the x and y direction for scanning. Alternative configurations are also used to move the tip instead of the sample, or to have a combination of the tip and sample motion. The resulting map of z positioning represents the topography of the sample surface.

AFM can be operated in various modes depending on the application. The primary modes of AFM operation are static mode and dynamic mode. In the static mode, the tip is kept in the same vertical position with respect to the sample surface, and is scanned across the surface of the sample to measure the contours of the surface by maintaining a constant tip-sample separation distance. In the dynamic mode, the tip is kept a small distance above the sample surface (also called non-contact mode) and is externally exited to oscillate at or near its resonant frequency. The oscillation amplitude, phase and resonance frequency are modified by tip-sample interaction forces.

The AFM operational modes can also be classified as contact, non-contact, and tapping modes depending on the tip-sample interaction force regimes. The tip-sample interaction force can be classified as two separated regimes depending on the tip-surface separation distance: repulsive regime and attractive regime, as shown in

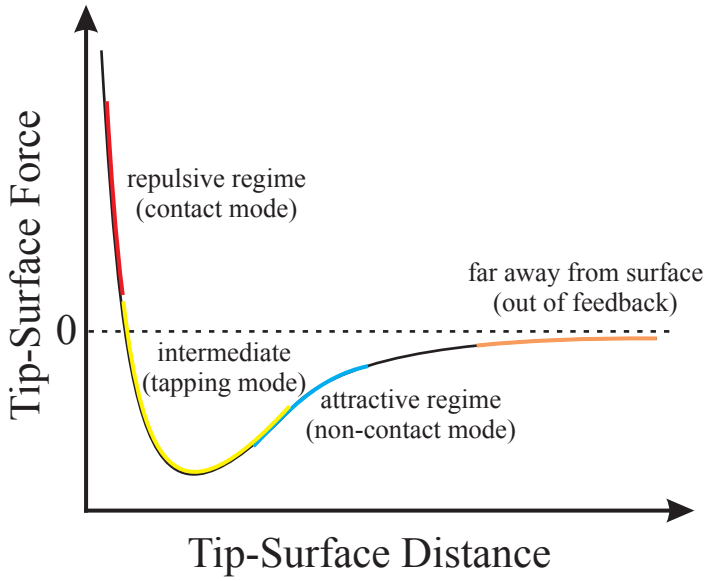

Figure 2.2: The repulsive and attractive force regimes as the AFM tip approaches the sample.

Fig. 2.2. At very small tip-sample distances (a few Å), there is a strong short-range repulsive force, which originates from the overlap of the electronic orbitals. Here, the tip is considered to be in contact with the sample surface. As the tip-sample distance increases (tens of nm), the long-range forces such as van der Waals interactions become dominant, and the tip is no longer considered to be in contact with the sample (non-contact regime). At even larger tip-sample distance (larger than hundreds of nm), the tip-sample interaction forces are generally too weak to be detected by the AFM tip.

The AFM contact mode is operated in the repulsive force regime, where the force between the tip and the surface is kept constant by maintaining a constant cantilever deflection signal during scanning. Contact mode is also an example of a static mode.

Non-contact mode is operated in the attractive regime, and is usually a dynamic mode where the tip is oscillated near its resonant frequency with a tip-sample distance of tens of nm, and the oscillation amplitude is typically a few ängstrøms to a few

nanometers. The resonance frequency of the cantilever is a function of the force gradient between the tip and sample surface:

$$\omega^2 = \omega_0^2(1 - \frac{1}{k}\frac{\partial F_{ts}}{\partial d}), \tag{2.2}$$

where ω, ω_0, k, F_{ts} and d are resonance frequency in the tip-sample force field, resonance frequency in free air, cantilever spring constant, tip-sample interaction force and tip-sample distance, respectively. For small amplitude, the frequency shift due to tip-sample interaction force is

$$\Delta\omega = \omega - \omega_0 = -\frac{\omega_0}{2k}\frac{\partial F_{ts}}{\partial d}. \tag{2.3}$$

Either the oscillation frequency (frequency modulation) or amplitude (amplitude modulation) can be monitored in order to maintain a constant tip-sample distance. In the *frequency modulation* mode, the tip is excited at the resonance frequency and oscillation amplitude is kept constant. A change of resonance frequency $\Delta\omega$ due to a change in the tip-sample distance is measured by a phase-locked loop (PLL) with very high sensitivity, and is then used as an input signal for the feedback loop to adjust the tip-sample separation distance. A constant $\Delta\omega$ maintains a constant tip-sample distance. In the *amplitude modulation* mode, the tip is oscillated at a fixed frequency slightly above resonance frequency. The shift in resonance frequency $\Delta\omega$ leads to a change of oscillation amplitude ΔA at maximum slope:

$$\Delta A_{\text{max slope}} = \frac{2QA_0}{3\sqrt{3}(k - \partial F_{ts}/\partial d)}\frac{\partial F_{ts}}{\partial d}, \tag{2.4}$$

where Q is the quality factor, and A_0 is the oscilation amplitude in free air. The amplitude change ΔA is then monitored and fed into feedback loop to adjust the tip-

sample distance. A constant oscillation amplitude maintains a constant tip-sample distance.

The feedback response time for frequency modulation mode is much faster (~$1/\omega_0$) than amplitude modulation mode (~Q/ω_0). In ultra-high vacuum condition, the cantilever quality factor Q can reach as high as 10^5. The feedback response for amplitude modulation would be too slow, so that frequency modulation mode is preferred. Single atoms can be easily imaged in vacuum using frequency modulation mode [5].

Tapping mode is operated in the intermediate force regime, where the cantilever can experience both attractive and repulsive force intermittently. In this mode, the tip is oscillating at a fixed frequency slightly below its resonance with a much higher oscillation amplitude (typically 100~200 nm) than non-contact mode. When the tip is brought close to the sample surface, the oscillation amplitude is significantly reduced due to the interaction of repulsive, attractive and damping forces in different tip-sample interaction regimes [6]. A set oscillation amplitude (typically 50%~70% of the free osillation amplitude) is maintained by the feedback loop to keep a constant tip-sample distance as the tip is scanned over the sample surface. Tapping mode is the most widely used AFM operational mode, since it is usually more accurate and more gentle than contact mode, and thus reduces the damage done to the surface.

SPM techniques used in this research include PFM, C-AFM, EFM, which are all based on the AFM technique. Here, we will briefly discuss operation principles of these techniques and the type of data they are capable to provide.

2.1.3 Piezoresponse Force Microscopy

Investigation of ferroelectric domain structures is of great importance due to the potential applications of ferroelectrics in next-generation devices and applications. Domain structures and properties in ferroelectric systems can strongly affect dielectric, pyroelectric, and electrocaloric effects in ferroelectrics. It is critical to be able to not only examine the ferroelectric domain microstructure, but also investigate external field-induced nucleation and dynamics of domains with high resolution. Piezoresponse force microscopy (PFM) is a contact mode AFM technique that allows imaging and manipulation of ferroelectric domains. It is based on the detection of local vibrations of the sample through the converse piezoelectric effect induced by a probing ac modulation bias applied through a conductive tip.

PFM was first used by Güthner and Dransfeld in 1992 to visualize the locally written domains in a ferroelectric polymer film [7]. The work by Gruverman with co-authors in 1995-96 [8, 9] is particularly important because it demonstrated imaging and manipulation of as-grown domains in inorganic thin film and bulk crystal ($Pb(Zr,Ti)O_3$, $BaTiO_3$, $LiNbO_3$) ferroelectrics. They coined the terms 'piezoresponse' and 'PFM' which has now become standard. Over the past years, PFM has become the mainstream tool for studying the static and dynamic properties of ferroelectric materials with the advantage of nanometer scale non-destructive imaging of ferroelectric domains and the capacity to locally manipulate ferroelectric polarization [10].

2.1.3.1 Principle of PFM

PFM is based on the detection of a local electromechanical response of the ferroelectric material through the converse piezoelectric effect: mechanical deformation is induced by the applied electric field. The mechanical strain due to deformation is described

as [11]:

$$s_j = d_{ij} E_i, \tag{2.5}$$

where s_j is the strain, d_{ij} the converse piezoelectric coefficient using matrix notation, and E_i is the external electric field. The piezoelectric coefficients are linked to the spontaneous polarization P in a ferroelectric material as [11]:

$$d_{ij} = 2\varepsilon_{im} Q_{jmk} P_k, \tag{2.6}$$

where ε_{im} is the dielectric constant tensor, and Q_{jmk} is the electrostriction coefficient tensor. For a ferroelectric material with tetragonal symmetry (point group: $4mm$), non-zero piezoelectric coefficients in the reduced matrix notation are:

$$d_{33} = 2\varepsilon_{33} Q_{33} P_3, \tag{2.7a}$$

$$d_{31} = 2\varepsilon_{33} Q_{13} P_3, \tag{2.7b}$$

$$d_{15} = 2\varepsilon_{11} Q_{44} P_3. \tag{2.7c}$$

where d_{33} is known as the longitudinal piezoelectric coefficient (along the polar axis), d_{31} is transverse piezoelectric coefficient (perpendicular to the applied field), and d_{15} is the shear coefficient.

Depending on the sign of polarization, the piezoelectric coefficients can be either positive or negative. This linear coupling between piezoelectric coefficients and spontaneous polarization can be used to detect ferroelectric domain polarity by determining the sign of mechanical strain, either expansion or contraction. The vertical deformation of the sample ΔL can be expressed as:

$$\Delta L = s_3 L = \pm d_{33} V, \tag{2.8}$$

where L is the sample thickness, V is the applied external voltage across the sample, and the $\pm$ sign reflects the opposite-oriented polarization direction.

Due to the small value of piezoelectric coefficient (typically tens of pm/V), it is very difficult to detect the static piezoresponse ΔL when the tip is biased by a fixed dc voltage. An alternative way is to use an ac modulation voltage instead of a constant dc bias. The alternating electric field causes the sample surface to vibrate at the modulation frequency due to piezoelectric effect, and this signal is detected and then amplified by the lock-in amplifier. This dynamic piezoresponse mode dramatically increases the sensitivity and reduces the imaging voltage required for domain imaging.

More specifically, in this approach, an ac modulation voltage is applied to the tip

$$V = V_{\mathrm{ac}} \cos(\omega t), \tag{2.9}$$

and the piezoresponse is detected at the first harmonic component of the tip deflection:

$$d = A_{1\omega} \cos(\omega t + \phi), \tag{2.10}$$

where d is the deflection signal, $A_{1\omega}$ is the first harmonic deflection vibration amplitude, and ϕ is the phase shift with respect to the applied ac voltage. For c^- ferroelectric domains the polarization vector is oriented downward, application of positive voltage results in expansion of the surface, so the piezoresponse is in phase with the applied ac voltage, i.e. $\phi = 0°$, while for opposite c^+ domains with upward oriented polarization, application of positive voltage results in contraction of the surface, so the piezoresponse is out of phase with phase shift $\phi = 180°$. These are schematically described in Fig. 2.3. For an ideal ferroelectric system, the piezoresponse amplitude for c^- and c^+ domains is equivalent, and zero at the domain boundary, while there is

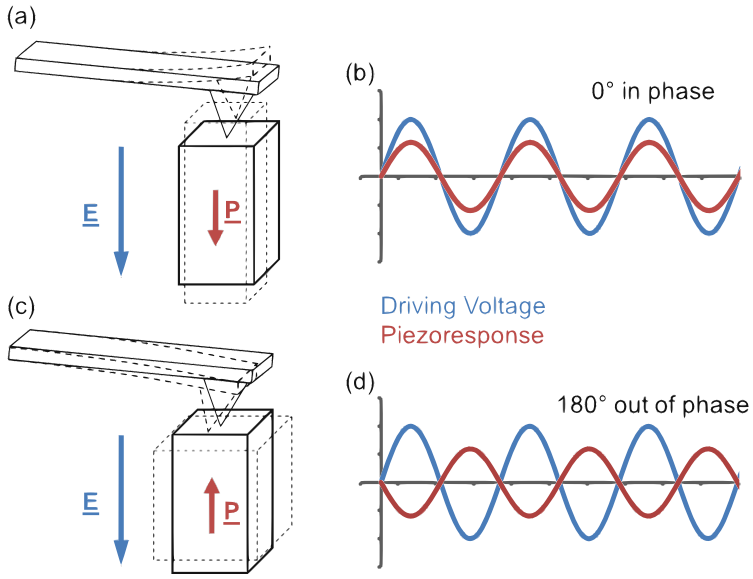

Figure 2.3: Schematics of piezoresponse: (a,b) In-phase piezoresponse on c^- domain, (c,d) out-of-phase response on the c^+ domain. Figure adapted from ref. [12].

180° of phase shift across the domain wall. By determining piezoresponse amplitude and phase at each point, a 2D map of ferroelectric polarization can be generated.

The cantilever deflection signal include not only *vertical* deflection signal but also *lateral* torsion deflection signal, leading to two basic PFM modes, vertical PFM (VPFM), and lateral PFM (LPFM). The VPFM detects out-of-plane polarization with vertical displacement Z as:

$$Z = d_{33} V_{\text{ac}} \cos(\omega t + \phi). \tag{2.11}$$

The LPFM detects in-plane polarization with lateral displacement X as:

$$X = d_{15} V_{\text{ac}} \cos(\omega t + \phi). \tag{2.12}$$

In both cases the phase shift ϕ determines the polarization orientation, either pointing into plane or out of plane for VPFM, or pointing left or right for LPFM. A combination

of x-direction LPFM and y-direction LPFM for imaging polarization in the x and y directions, and z-direction VPFM for polarization in the z direction result in a 3-D reconstruction of polarization orientation, which is usually mentioned as vector PFM [13]. Figure 2.4 shows an example of VPFM and LPFM imaging on $BiFeO_3$ thin

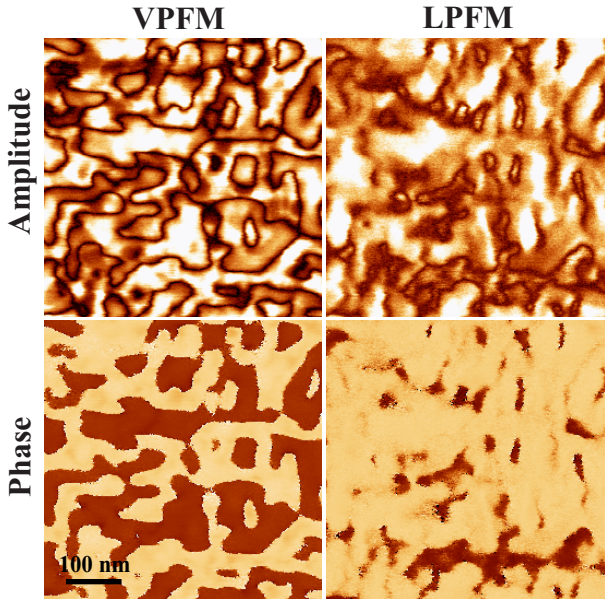

Figure 2.4: VPFM and LPFM on (001)-$BiFeO_3$(20nm)/(La,Sr)MnO_3/$SrTiO_3$ aquired simultaneously.

film aquired simultaneously. Vertical domains (z direction, in-plain and out-of-plain) and lateral domains (x direction, left and right) are distinguishable from PFM phase images, whereas amplitude signal is minimum (virtually zero) at domain boundaries.

In a real system, the measured signal contains additional contributions from local and distributed electrostatic forces. In general, the total response of the cantilever in contact with a ferroelectric surface can be written as follows [14]:

$$A = A_{\text{em}} + A_{\text{cap}} + A_{\text{nl}}, \tag{2.13}$$

where A_{em} is the electromechanical response, A_{cap} is the capacitive and Coulombic

tip–surface interaction, and A_{nl} is the non-local cantilever capacitive coupling. It is difficult to separate all the interactions, so that quantifying PFM signal in general is not trivial. However, the electrostatic interaction can be minimized by using top electrode, using short and stiff cantilevers, applying zero dc bias during imaging, etc [14].

2.1.3.2 Conventional PFM set-up

PFM is a contact mode AFM technique (Fig. 2.5). A conductive tip is used to apply an ac bias across the sample in order to induce as oscillating deformation of the sample through the converse piezoelectric effect. The resulting deflection of the cantilever is detected by the photodiode detector. As shown in Fig. 2.5, the

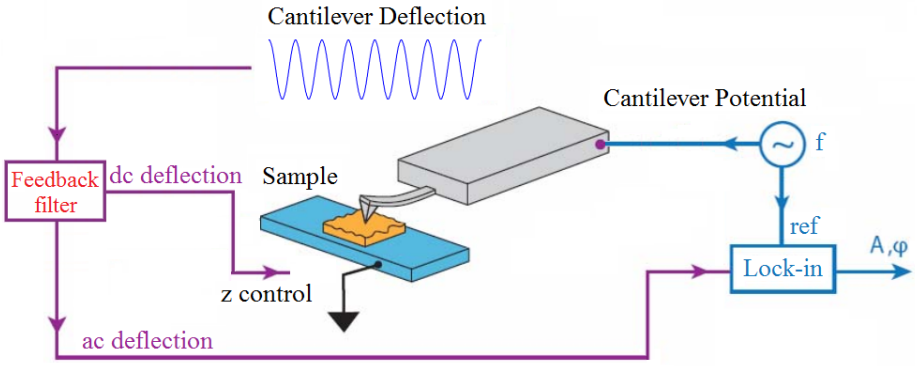

Figure 2.5: Schematics of PFM set-up. The deflection signal is filtered into dc deflection signal for z feedback control, and ac deflection signal for piezoresponse information.

cantilever deflection signal is filtered into dc (low frequency) and ac (high frequency) deflection signal through a feedback filter. The dc deflection signal is used as input for the feedback loop to track the surface topography, while the ac deflection signal contains piezoresponse signal. The frequency of the piezoelectric oscillation is much higher than the cut-off frequency of the feedback used for detecting static (or low frequency) cantilever deflection, so that both surface topography and ferroelectric

domains can be imaged simultaneously with high resolution. The ac deflection signal is then analyzed by the lock-in amplifier and decomposed into PFM amplitude and phase signals. The original ac modulation signal provides reference frequency and phase offset information for extracting PFM signal.

There are two approaches for imaging ferroelectric domains: local excitation on ferroelectric thin films and integral excitation on ferroelectric capacitors (Fig. 2.6).

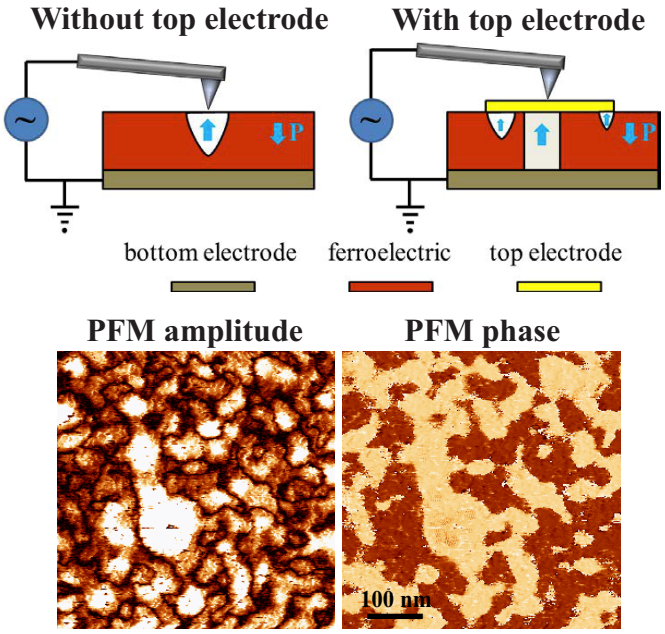

Figure 2.6: Top: schematic set up of two PFM imaging approach: on a bare ferroelectric surface without top electrode, and through the metal top electrode. Bottom: an example of domain structure visualized through 10 nm Pt top electrode on $Pb(Zr,Ti)O_3(10nm)/SrRuO_3/DyScO_3$.

In the first approach, the tip is directly in contact with a ferroelectric surface. Local piezoresponse is detected when applying a modulation voltage to the conductive tip. Due to the local detection of electromechanical response, high lateral resolution can be achieved. Also it allows for local control of nanoscale domains by applying switching voltage pulses. However, in this approach, the electric field applied through the tip is highly inhomogeneous, in which case converse flexoelectricity may be particularly

important (see Chap. 7), and may give rise to an apparent piezoelectric response, even in nonpiezoelectric materials. In addition, there are also contributions from electrostatic effect which makes it difficult to quantify the signal. In the second approach, modulation voltage is applied through the tip in contact with the top electrode of a ferroelectric capacitor. In this case, the whole volume underneath the top electrode is excited by the modulation voltage. The piezoresponse is still detected locally by the tip which picks up local polarization information. Ferroelectric domains can still be visualized by detecting the local piezoresponse signal at each point. In this approach, homogeneous electric field is generated between the top and bottom electrodes, and electrostatic contribution can be eliminated, which helps for quantitative characterization of local ferroelectric properties. However, the presence of the top electrode reduces the imaging resolution. Figure 2.4 gives an example of PFM domain imaging on bare $BiFeO_3$ surface, while Fig. 2.6 shows an example of PFM imaging of domain structures through a 10 nm Pt top electrode on $Pb(Zr,Ti)O_3$ film.

PFM has now become a standard tool for investigation of nanoscale properties of ferroelectric materials. It also allows characterization of electromechanical and structural properties of a wide range of piezoelectrically active materials, leading to a better understanding of material functionality down to the nanoscale level.

2.1.3.3 Resonance-enhanced PFM

In the conventional PFM set-up, the frequency of the modulation voltage is kept well below the cantilever's contact resonance frequency to avoid topographic cross-talk. The modulation voltage should be kept well below the coercive voltage of the ferroelectric film to avoid destruction of the original domain structure. The vertical electromechanical vibration of the surface is only tens of picometers, making

it difficult to detect especially for those with small piezoelectric coefficients or of a small thickness.

A significant enhancement of the piezoresponse sensitivity can be achieved by operating the PFM at the contact resonance frequency [15]. The piezoresponse signal at contact resonance is amplified by the quality factor Q of the tip-sample oscillation system when using the harmonic oscillator model [16]:

$$A = d_{33} V_{\mathrm{ac}} Q. \tag{2.14}$$

Typical Q values for PFM cantilevers range from tens to hundreds, which implies that one can amplify a PFM signal by up to two orders of magnitude simply by driving the modulation at the contact resonance frequency. On the other hand, operating at contact resonance introduces topographic cross-talks in the PFM signal that is not desired. A good optimization of such a situation is to operate the modulation voltage near the resonance instead of right at the resonance frequency.

The largest problem for operating at contact resonance is that the resonance frequency is very unstable. As the tip scans over the sample surface, the stiffness of the mechanical contact typically changes significantly, which results in a shift of the resonance frequency. Also, the tip can pick up some contaminants during scanning and thus changes the effective mass, which also changes the resonance frequency. The most commonly used resonance-tracking feedback loop, phase-locked loop (PLL), utilizes the phase sensitive signal of a lock-in amplifier to maintain the system at a specific phase value. This technique is generally limited to the case where the phase and amplitude of the driving force are constant, which is clearly not the case in PFM of ferroelectrics, where the phase and amplitude signal are related to the local material properties.

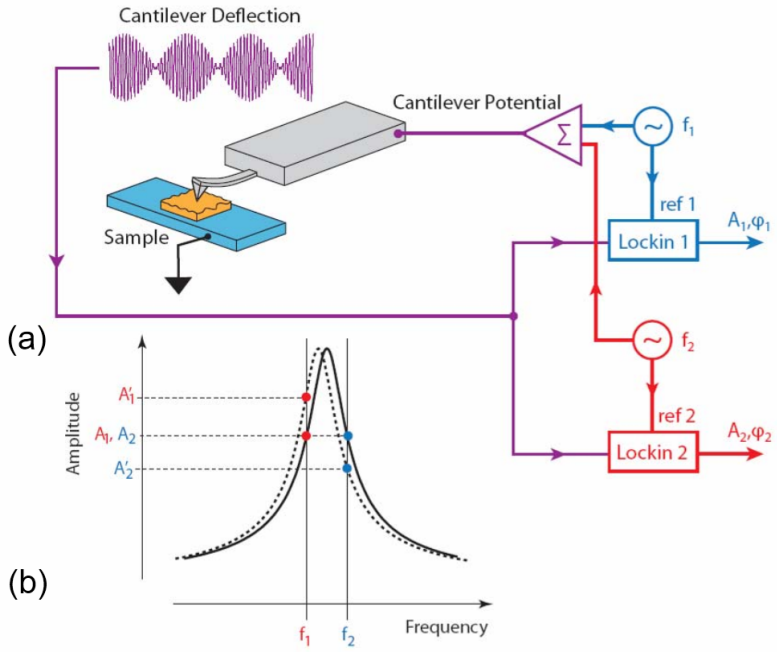

Figure 2.7: Schematics of the dual ac resonance tracking (DART) mode set up. Adapted from [17].

An approach to solve this problem is called dual ac resonance tracking (DART) method [17] (Fig. 2.7). In this approach, two oscillating voltages with different frequencies are applied to the conductive tip simultaneously, one below (f_1) and one above (f_2) the contact resonance frequency f_0. The resulting piezoresponse signal is measured at frequencies f_1 and f_2 using two lock-in amplifiers, and then decoupled into two amplitude signal, A_1 and A_2, and two phase signal, ϕ_1 and ϕ_2. The difference in amplitudes $\Delta A = A_1 - A_2$ is used as an error signal for feedback loop. Change of resonance frequency results in change of ΔA. The feedback keeps a constant ΔA and thus tracks the resonance frequency.

DART-PFM significantly increases signal to noise ratio and stabilizes piezoresponse signal in PFM imaging (Fig. 2.8), making it possible to study systems with weak piezoresponse, such as ultrathin ferroelectric films.

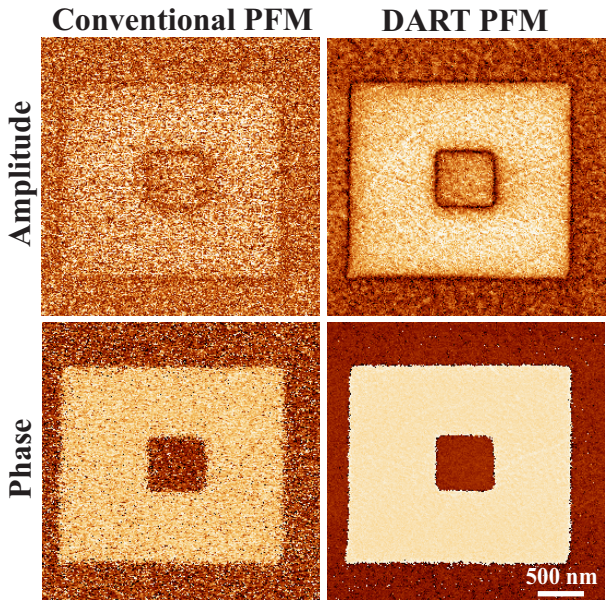

Figure 2.8: Comparison of conventional PFM and DART PFM on $BaTiO_3$(20nm) /(La,Sr)MnO_3/$SrTiO_3$.

2.1.3.4 Local PFM switching spectroscopy

PFM switching spectroscopy refers to measuements of local electromechanical hysteresis loops in ferroelectric materials. It is realized by sweeping of a dc bias applied to the PFM tip fixed at a certain point on the sample surface and simultaneous recording of the piezoresponse signal. The resulting hysteretic strain loop from piezoresponse signal due to polarization switching contains information on local ferroelectric behavior such as coercive voltage, imprint, etc.

Two different types of measurement procedures are used for PFM spectroscopy: step mode and pulse mode, as shown in Fig. 2.9. In the step mode, step-up dc voltage applied to induce polarization switching is superimposed on an ac modulation voltage to record a voltage dependence of the PFM signal (bias-on hysteresis) (Fig. 2.9(a)). Such a measurement always contains strong electrostatic interaction, and sometimes may dominate the response signal. However, use of a top electrode screens the elec-

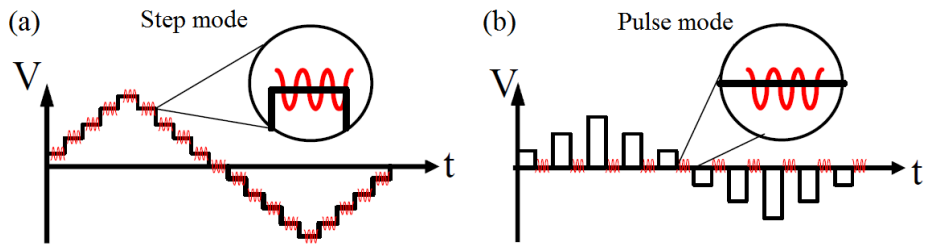

Figure 2.9: Two different modes in PFM spectroscopy: (a) step mode and (b) pulse mode.

trostatic charges and significantly reduces the electrostatic force. Hence this mode is more suitable for capacitors. In the pulsed mode, step-up dc pulses are applied to induce switching, while ac modulation voltage is applied between the pulses (bias-off hysteresis) (Fig. 2.9(b)). Electrostatic effects and capacitive coupling are greatly reduced in this mode, therefore it is more suitable for ferroelectric thin films. Figure

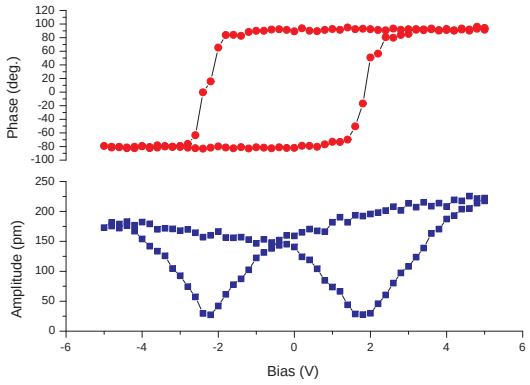

Figure 2.10: Example of a PFM hysteresis loop measured on 12 u.c. $BaTiO_3$ film (top: PFM phase; bottom: PFM amplitude).

2.10 shows an example of a bias-off PFM hysteresis loop measured on $BaTiO_3$ thin film. It represents polarization switching which corresponds to a minimum of the PFM amplitude and a 180° shift of the phase signal.

By measuring local PFM hysteresis loops at each point, it is possible to generate

a 2-D map with information of coercive voltages, imprint, nucleation voltages, etc., which is called switching spectroscopy PFM (SSPFM) [18]. Spatial inhomogeneities of ferroelectric polarization switching can be examined in this way.

2.1.4 Conductive Atomic Force Microscopy

The AFM can also be operated in a conductive mode, which is usually referred to as conductive AFM (C-AFM) that measures the electrical current through the sample due to a constant dc bias. C-AFM operates in AFM contact mode, where surface topography can be generated by the conventional contact AFM method. In addition, a current amplifier is integrated in the system with a sensitivity down to sub-pA range. Current flowing between the conductive tip and a bottom electrode through the sample is collected when applying a voltage across the film. Figure 2.11 shows a schematic set up of C-AFM, where a current amplifier is connected to the conductive AFM tip for sensing minuscule currents passing through the tip.

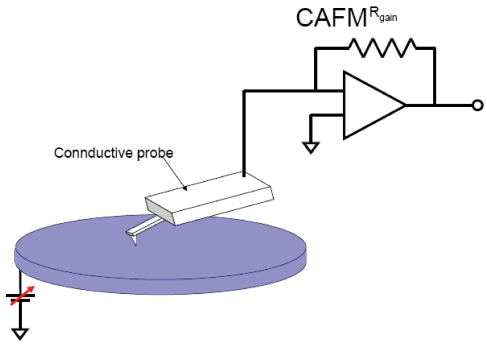

Figure 2.11: Schematics of the C-AFM set up. There is a current amplifier for sensing current flowing through the conductive AFM tip.

A current map can be generated by maintaining a constant dc bias across the sample while scanning the sample surface. Local current-voltage (I–V) spectroscopy

can also be done by sweeping a dc bias while collecting current signal at a fixed position.

C-AFM is a powerful technique for studying local electrical transport behavior, such as polarization-coupled resistive switching behavior in ferroelectric tunnel junctions, domain wall conductivity in ferroelectrics. It allows current measurements in the range of hundreds of fA to μA, with a spatial resolution down to the nm scale.

2.1.5 Electrostatic Force Microscopy

Electrostatic force microscopy (EFM) is a technique for imaging surface charges based on electrostatic interaction between the tip and sample surface. The electrostatic force is a long-range force which arises due to the interaction of separated charges on the tip and sample surface. EFM is operated in the non-contact AFM mode, and is usually realized by a two-pass scan mode: the first pass scan operates in conventional non-contact or tapping mode to obtain the surface topography profile, and the second pass lifts up the tip with a constant tip-sample distance, typically 50 to 100 nm, according to the topographic profile from the first pass scan. The second pass scan senses the long-range electrostatic force by maintaining a constant dc bias on the conductive tip. The AFM tip is driven at a fixed frequency near resonance for both passes. Due to the attractive or repulsive electrostatic force between the biased tip and sample surface charges, there is a shift of resonance frequency from Eq. 2.3 that is proportional to the force gradient: $\Delta\omega \propto -\partial F_{ts}/\partial d$. An attractive force results in a positive force gradient in the z direction, leading to a negative shift of the resonance frequency, while a repulsive force leads to a positive shift. By detecting the resonance frequency shift from the vibration amplitude or phase, it is possible to determine the sign of surface charge and relative charge density.

In ferroelectrics, EFM is used for sensing surface screening charges, which are important for stabilizing the polarization, especially in ultrathin films. Surface injection charges due to electrical poling are also investigated via EFM.

Additionally, the two pass scheme used in EFM is also applied to other AFM modes for detection of different types of long-range forces, such as magnetic force in magnetic force microscopy (MFM), which uses a magnetic tip to detect surface magnetization.

2.2 Force Calibration of AFM Cantilevers

An important application of the AFM is quantitative force measurements. The mechanical load F applied to the sample surface through the tip is expressed by Hooke's law:

$$F = kZ. \tag{2.15}$$

where k is the spring constant of the cantilever, and Z is vertical displacement of the tip. Precise calibration of the mechanical load is realized by calibrating the optical lever sensitivity (s) of the optical beam system, and the spring constant (k) of the cantilever. The optical lever sensitivity transfers the cantilever deflection measured by the photo detector in Volts to actual tip displacement in meters. It is realized by measuring the slope of a force-distance curve on a hard surface in the contact mode:

$$s = \frac{Z}{d}, \tag{2.16}$$

where d is the dc deflection signal from photo detector, and Z is measured from z-piezo displacement.

The spring constant of the cantilever is measured by the thermal noise method

[19]. This method uses the equipartition theorem to relate the measured thermal noise in the AFM cantilever deflection signal to the spring constant in the cantilever [19]:

$$\frac{1}{2}k\langle x^2\rangle = \frac{1}{2}k_BT, \tag{2.17}$$

where $\langle x^2\rangle$ is positional thermal noise, k_B Boltzmann's constant and T the absolute temperature. The spring constant to be determined is therefore:

$$k = \frac{k_BT}{\langle x^2\rangle}. \tag{2.18}$$

However, the cantilever cannot be treated as an ideal spring. A series of improvements lead to the correct calibration formula [20, 21, 22]:

$$k = 0.8174\frac{k_BT}{s^2P_{\mathrm{DC}}}[\frac{1-(\frac{3h}{2L})\tan\phi}{1-(\frac{2h}{L})\tan\phi}\cos\phi]^2, \tag{2.19}$$

where the numerical factor 0.8174 is a result of the geometry of the cantilever; s is the sensitivity calibration factor; P_{DC} is the positional noise power isolated in the fundamental resonant mode only and measured in Volts^2; h is the height of the tip; L is the cantilever length, and ϕ is the angle of the cantilever from the horizontal. ϕ is usually given for a specific AFM system, typically 10° to 15°. For a typical AFM tip with small h/L ratio, the term in the brackets in Eq. 2.19 simply reduces to $\cos\phi$:

$$k = 0.8174\frac{k_BT}{s^2P_{\mathrm{DC}}}\cos^2\phi. \tag{2.20}$$

The only unknown parameter P_{DC} is obtained from a Lorentzian fit to the first reso-

nance of the power spectral density (PSD) of the noise data:

$$P(\omega) = P_{\mathrm{DC}} \frac{\omega^2}{4(\omega - \omega_0)^2 + (\frac{\omega}{Q})^2}, \tag{2.21}$$

where $P(\omega)$ is the power spectral density of the noise data recorded by the photo detector; P_{DC} is the dc power response used in Eq. 2.19; ω and ω_0 are frequency and first resonance frequency respectivly; Q is the quality factor. Substituting P_{DC} into Eq. 2.19 gives the cantilever spring constant k.

Lateral friction forces can be measured from lateral deflection signal of the cantilever:

$$F_L = k_L s_L d_L, \tag{2.22}$$

where F_L, k_L, s_L and d_L are lateral force, lateral torsional spring constant of the cantilever, lateral optical sensitivity and lateral deflection signal, respectively. The lateral sping constant can be obtained from the relationship between vertical and lateral spring constants [23]:

$$k_L = k \frac{W^2}{T^2}, \tag{2.23}$$

where k is the normal spring constant; W and T are width and thickness of the cantilever. Also, the lateral sensitivity is obtained from the relation:

$$\frac{s}{s_L} = \frac{3}{2} \frac{h}{L}, \tag{2.24}$$

where h is the height of the tip, and L is the length of the cantilever. Lateral force in Eq. 2.22 therefore becomes

$$F_L = \frac{2}{3} \frac{W^2 L}{T^2 h} k s d_L. \tag{2.25}$$

2.3 Typical Experimental Conditions Used in This Research

A commercial AFM system, MFP-3D from Asylum Research, was used for characterization of ferroelectric materials in this research. For PFM imaging, Pt or PtIr coated silicon tips with a spring constant of about 3 N/m and a free resonance frequency of about 75 kHz were used (NSC18 from Mikromasch and PPP-EFM, PtSi-FM from Nanosensors) in DART-PFM mode. A contact resonance frequency of about 350 kHz was used for these tips. PFM ac modulation voltage is typically 0.3 V to 0.5 V in amplitude. For C-AFM measurements, durable diamond tips are preferred, such as CDT-NCHR from Nanosensors. The mechanical load for PFM imaging is typically between 10 nN and 100 nN, while for mechanical writing loads from several hundreds nN up to 2000 nN were applied.

References

[1] C. Gerber and H. P. Lang, Nat. Nanotechnol. **1**, 3 (2006).

[2] G. Binnig, H. Rohrer, Ch. Gerber, and E. Weibel, App. Phys. Lett. **40**, 178 (1982).

[3] G. Binnig, H. Rohrer, Ch. Gerber, and E. Weibel, Phys. Rev. Lett. **50**, 120 (1983).

[4] G. Binnig, C. F. Quate, and Ch. Gerber, Phys. Rev. Lett. **56**, 930 (1986).

[5] F.J. Giessibl, Science **267**, 68–71 (1995).

[6] L. Wang, Appl. Phys. Lett. **73**, 3781 (1998).

[7] P. Güthner and K. Dransfeld, Appl. Phys. Lett. **61**, 1137 (1992).

[8] A. Gruverman, O. Kolosov, J. Hatano, K. Takahashi, and H. Tokumoto, J. Vac. Sci. Technol. B **13**, 1095 (1995).

[9] A. Gruverman, O. Auciello, and H. Tokumoto, J. Vac. Sci. Technol. B **14**, 602 (1996).

[10] D. A. Bonnell, S. V. Kalinin, A. Kholkin, and A. Gruverman, MRS Bull. **34**, 648 (2009).

[11] Seungbum Hong, editor. *Nanoscale Phenomenon in Ferroelectric Thin Films*. Springer, Germany (2004).

[12] *http://en.wikipedia.org/wiki/Piezoresponse_force_microscopy*.

[13] S. V. Kalinin, B. J. Rodriguez, S. Jesse, J. Shin, A. P. Baddorf, P. Gupta, H. Jain, D. B. Williams, and A. Gruverman, Microsc Microanal. **12**, 206 (2006).

[14] S. V. Kalinin and D. A. Bonnell, Phys. Rev. B **65**, 125408 (2002).

[15] C. Harnagea, A. Pignolet, M. Alexe, and D. Hesse, IEEE Trans. Ultrason., Ferroelectr., Freq. Control **53**, 2309 (2006).

[16] R. García and R. Pérez, Surf. Sci. Reports **47**, 197 (2002).

[17] B. J. Rodriguez, C. Callahan, S. Kalinin, and R. Proksch, Nanotechnology **18**, 475504 (2007).

[18] S. Jesse, A. P. Baddorf, and S. V. Kalinin1, Appl. Phys. Lett. **88**, 062908 (2006).

[19] J. L. Hutter and J. Bechhoefer, Rev. Sci. Instrum. **64**, 1868–1873 (1993).

[20] H.-J. Butt and M. Jaschke, Nanotechnol. **6**, 1–7 (1995).

[21] D. A. Walters, J. P. Cleveland, N. H. Thomson, P. K. Hansma, M. A. Wendman, G. Gurley, , and V. Elings, Rev. Sci. Instrum. **67**, 3583–3590 (1996).

[22] L.-O. Heim, M. Kappl, and H.-J. Butt, Langmuir **20**, 2760–2764 (2004).

[23] H.-J. Butt, B. Cappella, and M. Kappl, Surf. Sci. Rep. **59**, 1 (2005).

Chapter 3

Tunneling Electroresistance Effect in Ultrathin Ferroelectrics

3.1 Introduction

3.1.1 Resistive switching

Resistive random-access memory (RRAM) is one of the most actively pursued technologies for the next generation of electronic devices. RRAM is based on the abrupt change in electrical resistance, referred to as the resistive switching phenomenon, induced by the applied electric field. This effect has been observed in many types of transition metal oxides, from binary oxides, such as NiO, CuO, TiO_2, and HfO, to complex oxide perovskites, such as $SrTiO_3$ and $SrZrO_3$, to even more complex multicomponent compounds, such as some manganites $LaCaMnO_3$ and $Pr_{1-x}La_xCaMnO_3$ and cuprates $YBa_2Cu_3O_7$, etc., among other materials [1, 2]. Although the resistive switching behavior is quite similar for different types of materials with hysteretic I–V characteristics, the physical mechanisms behind this effect are quite diverse [2], and

can include Schottky barriers [3], spatial inhomogeneity [4], trapping of charge carriers, oxygen vacancy migration, filamentary path formation [5], Mott metal-insulator transitions, etc.

3.1.2 Ferroelectric tunnel junctions

A new type of resistive switching mechanism based on polarization reversal in ferroelectric tunnel junctions (FTJs) has been recently discovered, making it a promising candidate for RRAMs. The advantages of using FTJ in RRAM devices include non-voltility of the resistive states, high scalability, high speed and low power consumption during read-out operation.

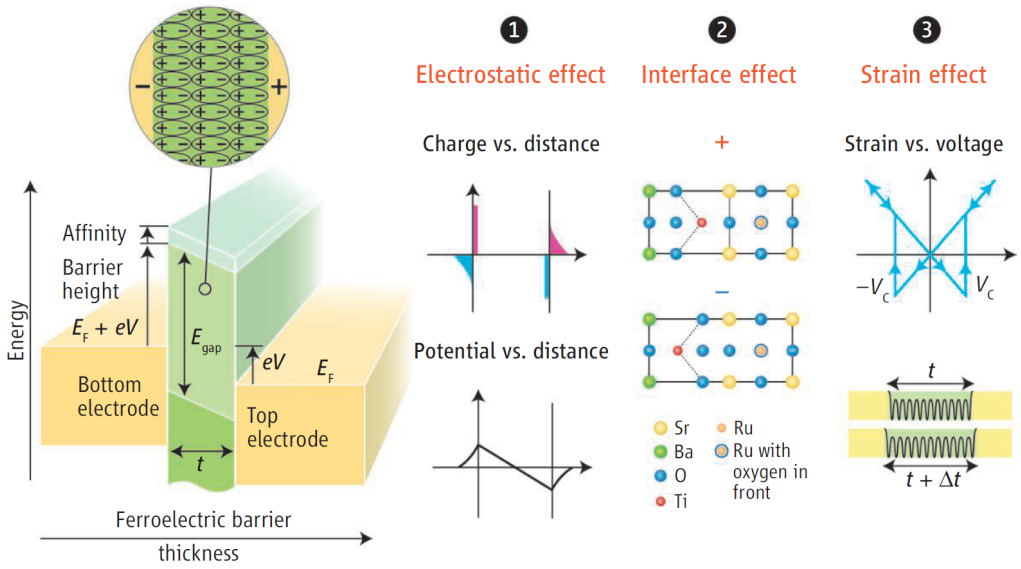

Figure 3.1: Schematic diagram of a ferroelectric tunnel junction, which consists of two electrodes separated by a nanometer-thick ferroelectric barrier layer. (E_{gap} is the energy gap. E_F is the Fermi energy, V is the applied voltage, V_c is the coercive voltage, t is the barrier thickness, and Δt is the thickness variation under an applied field. Figure addapted from ref. [6].

FTJs are tunnel junctions based on the quantum tunneling phenomenon. In a tunnel junction, two metal electrodes are separated by a very thin insulating barrier

or vacuum [7], so that electrons can still tunnel through the insulating barrier when there is a voltage drop across the junction. A ferroelectric material can be employed as the barrier layer with a metal-ferroelectric-metal structure. Such a device is known as a FTJ and is schematically depicted in Fig. 3.1. An important phenomenon of FTJs is a resistive switching behavior upon polarization reversal in the ferroelectric barrier, which is known as the tunneling electroresistance (TER) effect.

The possible mechanisms of the TER effect are illustrated in Fig. 3.1 [6]: (a) the electrostatic potential across the junction, (b) interface bonding strength, and/or (c) strain associated with the piezoelectric deformation. The electrostatic effect arises from incomplete screening of the polarization charges at the interface of FTJs [8], which results in an asymmetric potential energy profile across the barrier in FTJs with different electrodes that have different screening lengths. Polarization switching results in the reversal of the depolarizing field, which modifies the tunneling potential profile and also the tunneling probability. The interface bonding effect comes from the restrictions of ferroelectric displacements, since the atoms at the boundary of the ferroelectric are bonded to the electrodes. The piezoelectric effect can also change the barrier thickness and hence affect the tunneling conductance.

Originally, the idea of the FTJ was proposed by Esaki in 1971 [9]. A crucial requirement for FTJs is the existence of ferroelectricity in a nanometer-thick barrier film. However, at that time, it was believed that the critical thickness for ferroelectricity, below which polarization becomes unstable, was a few tens of nanometers, which was much larger than the thickness necessary for tunneling to take place. Recent theoretical and experimental reports on stable ferroelectricity at the thickness down to the unit cell scale opened up doors for experimental implementation of the FTJ structures [10, 11, 12, 13].

The electrically induced resistance switching in FTJs is fundamentally different

from the one observed in a number of transition metal oxides, such as titanates, manganites, and zirconates. A common feature of these mechanisms is that they are related to nano- or atomic scale inhomogeneities [14, 15]. In the FTJs, the resistance switching is realized via a pure electronic mechanism, which involves ferroelectric polarization reversal. By reversing the polarization of the ferroelectric barrier, it is possible to change an internal electronic potential profile and hence alter the transmission probability and produce the TER effect [8, 16, 17]. In this case, simultaneous monitoring of polarization and conductance is essential to distinguish ferroelectric-related resistive switching from non-ferroelectric effect.

Scanning probe microscopy (SPM) techniques allow the localization of an electric field within nanometer scale regions with simultaneous probing of polarization by piezoresponse force microscopy (PFM) and tunneling current by conducting atomic force microscopy (C-AFM). In this chapter, by using a set of scanning probe microscopy techniques, we demonstrate the reproducible tunneling electroresistance effect on nanometer-thick epitaxial $BaTiO_3$ single-crystalline thin films on $SrRuO_3$ bottom electrodes. Correlation between ferroelectric and electronic transport properties is established by direct nanoscale visualization and control of polarization and tunneling current. The obtained results show a change in resistance by about 2 orders of magnitude upon polarization reversal on a lateral scale of 20 nm at room temperature. These results are promising for employing ferroelectric tunnel junctions in nonvolatile memory and logic devices [18].

Results described in this chapter have been published in ref. [18].

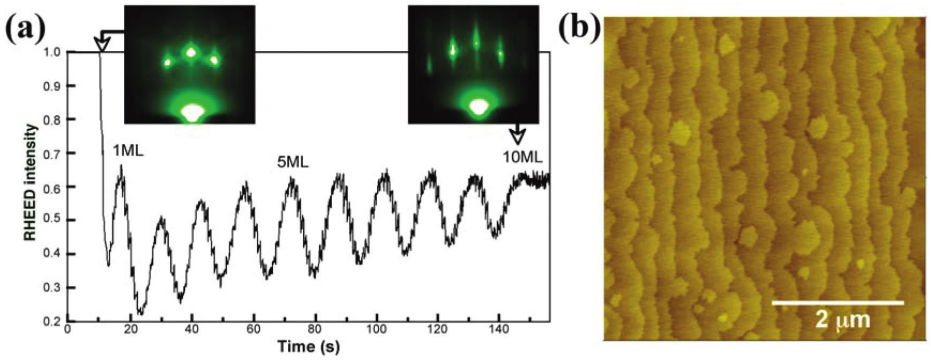

Figure 3.2: (a) RHEED intensity oscillation during the growth of $BaTiO_3$ ferroelectric layer on $SrRuO_3$ bottom electrode and RHEED patterns before and after $BaTiO_3$ deposition; (b) AFM image of $BaTiO_3$ film on $SrRuO_3/SrTiO_3$ substrate. Figure addapted from ref. [18].

3.2 Materials and Methods

Structurally and electrically perfect epitaxial ferroelectric heterostructures with a thickness of just several unit cells (u.c.) are a prerequisite for implementation of FTJs. To achieve the atomically abrupt and well-defined interfaces, epitaxial $BaTiO_3$ films have been fabricated by atomic layer controlled growth with in situ monitoring using high pressure reflection high energy electron diffraction (RHEED) [19, 20]. Here we have used $BaTiO_3$ films with a thickness of 6 and 12 u.c. (2.4 and 4.8 nm) grown on atomically smooth TiO_2-terminated (001)-$SrTiO_3$ substrates with single crystalline $SrRuO_3$ electrodes, for probing the nanoscale ferroelectric switching and tunneling transport behavior. Fig. 3.2(a) shows RHEED intensity oscillation and RHEED patterns indicating a layer-by-layer growth and epitaxial structure of the $BaTiO_3$ films. The AFM image of $BaTiO_3/SrRuO_3$ heterostructure in Fig. 3.2(b) clearly indicates atomically flat terraces with single unit-cell high (~4 Å) steps. Cross-sectional TEM images demonstrate that the $BaTiO_3$ and $SrRuO_3$ layers are fully commensurate with the $SrTiO_3$ substrates.

3.3 Polarization–conductance Correlation

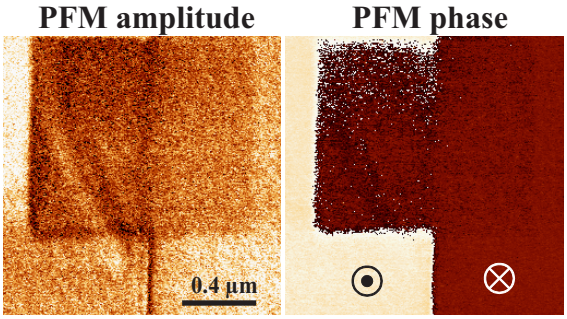

Figure 3.3: PFM amplitude and phase images showing domain structures of a 2 u.c. $BaTiO_3$ film after poling.

Polarization stability of the ultrathin $BaTiO_3$ films has been confirmed by PFM. Figure 3.3 shows PFM images on a 2 u.c. $BaTiO_3$ film after poling. The stable PFM signal indicates a stable and switchable ferroelectric polarization on ultrathin $BaTiO_3$ films down to 2 u.c.

We investigate the polarization-dependent TER effect by monitoring and controlling the electric polarization and correlating local ferroelectric switching with the local conductivity. Our approach is to employ a combination of PFM for nanoscale polarization detection and C-AFM for spatially resolved local conductance measurements. Figure 3.4(a) shows a sketch of the experiment geometry, which involves a conductive probing tip in contact with a bare $BaTiO_3$ surface connected to a power supply for local piezoresponse and current measurements. Local current–voltage characteristics were measured by positioning a conductive diamond tip at a selected point on the film surface and by sweeping a dc voltage. Current maps were obtained simultaneously with the topographic data by scanning the surface with the tip held under a constant dc bias well below the coercive voltage and measuring current at each pixel point of the scanned area.

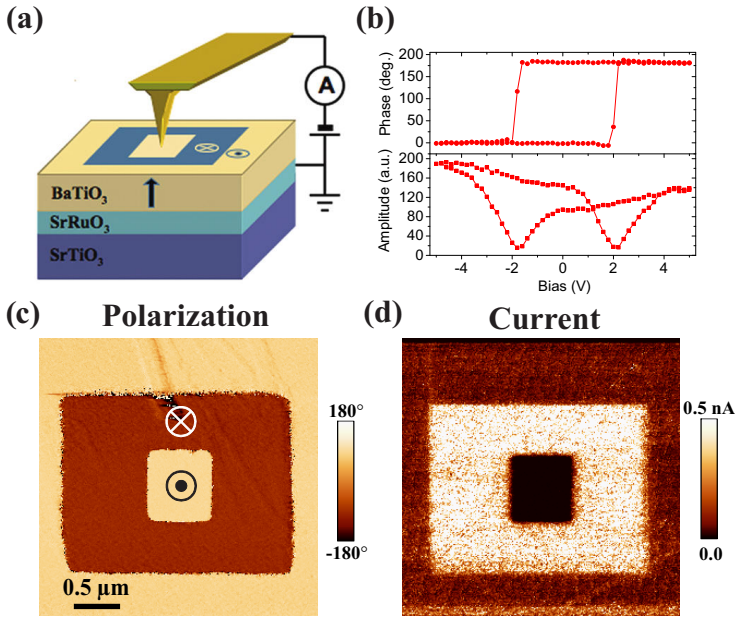

Figure 3.4: (a) Sketch illustrating the geometry of experiment for PFM/C-AFM studies of tunneling electroresistance effect in ultrathin $BaTiO_3$ films. (b) Local PFM hysteresis loops measured in the 12 u.c. $BaTiO_3$ film. (c) PFM image of a polarization pattern produced by scanning with the tip under ± 3.0 V. (d) Tunneling current map acquired in the same region as in (c). Bright contrast indicating higher current is observed in the regions with polarization oriented downward.

Figure 3.4(b) shows a local PFM spectroscopy of a 12 u.c. $BaTiO_3$ film that reveals a hysteretic behavior typical for polarization switching. Preliminary testing of polarization by means of PFM shows that the as-grown $BaTiO_3$ films are in a single-domain state with the upward polarization direction, which is consistent with an upward built-in electric field of about 10^6 V/cm from local spectroscopy measurement.

To demonstrate the TER effect, a bi-polar domain pattern is generated electrically by scanning the film surface with tip voltage $V_{\text{tip}} = \pm 3.0$ V. Figure 3.4(c) shows the resulting polarization pattern as measured by PFM, where polarization in the small squire is electrically switched upward and in the large squire is switched downward, while outside of the squires is as-grown upward polarized. Antiparallel domains written this way demonstrate almost no relaxation a few days after switching, which

suggests a highly stable and robust polarization.

The resistive switching behavior of the $BaTiO_3$ films is examined using the C-AFM technique. A current map is obtained by scanning the polarization-patterned area with a dc bias of 0.3 V well below the coercive voltage. Figure 3.4(d) shows the resulting current map within the poled area where variations in contrast correspond to different conductivity. The striking feature evident from the comparison of Fig. 3.4 (c) and (d) is a perfect correspondence of the spatial variations in local conductivity to the polarization domain pattern. The area with downward polarization shows significantly higher conductivity than the area with upward polarization with the resistance ratio between the two polarization states of about 7 and 80 for the 6 u.c. and 12 u.c. $BaTiO_3$ films, respectively. The small dc bias used for conductance measurements does not perturb the ferroelectric state, thus allowing multiple nondestructive polarization readouts. These experimental results prove the concept of FTJ and show the capability of information storage and readouts in ultrathin ferroelectrics.

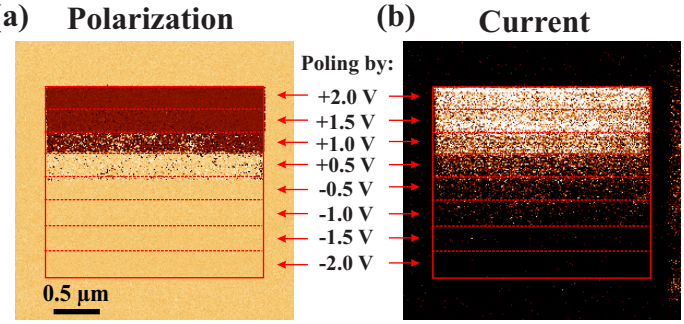

Figure 3.5: Spatially resolved correlation between the onset of polarization reversal (a) and a change in electrical conductance (b). A change in the polarization contrast in the red block from bright to dark illustrates polarization reversal under an incrementally changing tip bias. Dashed red lines indicate where the bias is changing. The change in PFM contrast correlates with the transition from low current (dark contrast) to high current (bright contrast).

To distinguish the ferroelectric-induced mechanism of resistive switching from other mechanisms, we have examined correlation between the onset of polarization

reversal and a change in electrical conductance in the same locations. The $BaTiO_3$ surface was scanned with the tip under an incrementally increasing dc bias with simultaneous PFM detection of polarization. The gradual change in the contrast under a tip bias close to the coercive voltage seen in Fig. 3.5(a) is an indication of polarization reversal. Subsequently, the current map was acquired in the same area by C-AFM. As seen from Fig. 3.5(b), the transition from high to low resistance states occurred exactly at the same bias where polarization undergoes reversal from the upward to downward direction. Resistance stays constant in the fully switched regions irrespective of what voltage is used for poling. This result is an unambiguous demonstration of the ferroelectric nature of the resistive switching.

3.4 Tunneling Electroresistance Effect

Spatially resolved imaging of polarization and tunneling current are complemented by local spectroscopic measurements which provide a quantitative insight into resistive switching [21]. I–V characteristics recorded for antiparallel domains show a nonlinear behavior typical for conductance in tunnel junctions and a drastic change in resistance (Fig. 3.6). In the case of the 12 u.c. $BaTiO_3$ film, the resistance changes by almost 2 orders of magnitude upon polarization reversal. These remarkable results clearly illustrate the giant TER effect in FTJs predicted earlier. High-resolution topographic imaging of the film surface did not show any signs of pinhole formation (which could be an indication of dielectric breakdown). This fact, as well as reproducibility of the I–V characteristics, strongly suggests that the electromigration effect can be ruled out.

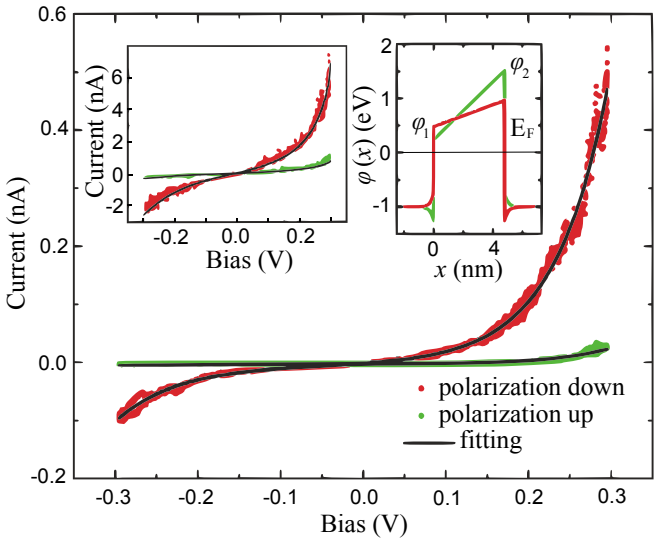

Figure 3.6: I–V curves for two opposite polarization directions in the 12 u.c. thick $BaTiO_3$ film measured by C-AFM. Solid lines, fitting of the experimental data by the WKB model. The inset shows schematically the potential energy profiles for two polarization orientations in the 12 u.c. $BaTiO_3$ film. I–V curves in the inset were measured for two opposite polarizations in the 6 u.c. $BaTiO_3$ film. Figure addapted from ref. [18].

3.5 Modeling of the TER Effect

It has been demonstrated theoretically [8, 17], that a change in electric polarization direction, and hence a change in the relative Ti displacements in the $BaTiO_3$ cell, can affect the density of states at the electrode-barrier interfaces, as well as the interface dipoles and complex band structure of the barrier, primarily due to changing interfacial atomic positions and electronic structure. In the case that the interfaces differ, the changes on polarization reversal are also likely to differ, leading to a dependence of tunneling current on polarization direction. To interpret our results, we assume direct tunneling through the barrier with interfacial effects and their change with polarization reversal by potential steps at the interfaces that depend on the polarization direction.

To model the observed TER effect, we employ a simple model, involving a tun-

neling current through a trapezoidal potential barrier [22] whose profile depends on polarization orientation. The barrier has width d and potential steps at the interfaces of ϕ_1 and ϕ_2, so that the potential energy across the barrier in the presence of bias voltage V varies as $\phi(x,V) = \phi_1 + eV/2 + x(\phi_2 - eV - \phi_1)/d$. Using the WKB approximation and assuming that the applied voltage is not too large, so that $eV/2 < \phi_{1,2}$, and the barrier width is not too small, so that $d[(2m/\hbar^2)\phi_{1,2}]^{1/2} \gg 1$, we obtain an analytic expression for the current density:

$$J \cong C\frac{\exp\{\alpha(V)[(\phi_2 - \frac{eV}{2})^{3/2} - (\phi_1 + \frac{eV}{2})^{3/2}]\}}{\alpha^2(V)[(\phi_2 - \frac{eV}{2})^{1/2} - (\phi_1 + \frac{eV}{2})^{1/2}]^2} \times \sinh\{\frac{3}{2}\alpha(V)[(\phi_2 - \frac{eV}{2})^{1/2} - (\phi_1 + \frac{eV}{2})^{1/2}]\frac{eV}{2}\}, \tag{3.1}$$

where $C = -(4em)/(9\pi^2\hbar^3)$ and $\alpha(V) \equiv [4d(2m)^{1/2}]/[3\hbar(\phi_1 + eV - \phi_2)]$.

Fig. 3.6 shows a fit of the experimental I–V characteristics for the 12 u.c. $BaTiO_3$ film, using Eq. 3.1 and the following parameters: $\phi_1 = 0.24$ eV and $\phi_2 = 1.52$ eV for polarization pointing up, $\phi_1 = 0.48$ eV and $\phi_2 = 0.96$ eV for polarization pointing down, $d = 4.8$ nm and $m = m_0$. In the fitting, we used a scaling factor which was assumed to be the same for two polarization orientations. The respective change in the potential energy profile is shown schematically in the inset of Fig. 3.6. According to these results, the reversal of polarization changes the potential energy difference $\phi_1 - \phi_2$ across the $BaTiO_3$ barrier from 1.28 to 0.48 eV. This change of 0.8 eV is due to the change in the electrostatic potential associated with ferroelectric polarization reversal and associated reorientation of the depolarizing field. We note that $\phi_2 - \phi_1$ is higher for polarization pointing up than for polarization pointing down indicating that "holes" dominate in the tunneling conductance. This behavior is expected if the decay constant of the evanescent state in the tunneling barrier is increasing with energy, which is the case for the Δ_1 band in $BaTiO_3$ [23].

In the Ohmic transport regime typical for a small bias voltage, Eq. 3.1 is reduced to

$$J \approx \frac{e^2}{2h}\frac{1}{2\pi d}\frac{\sqrt{2m}}{\hbar}(\phi_2^{1/2}+\phi_1^{1/2})\exp[-\frac{4\sqrt{2m}}{3\hbar}\frac{\phi_2^{3/2}-\phi_1^{3/2}}{\phi_2-\phi_1}d]V. \tag{3.2}$$

If the difference between potential steps $\Delta\phi \equiv \phi_2 - \phi_1$ is not too large compared to the average potential $\bar{\phi} \equiv (\phi_2+\phi_1)/2$, so that $\Delta\phi/2 < \bar{\phi}$, this formula can be approximated by

$$J \approx \frac{e^2}{h}\frac{1}{2\pi d}\frac{\sqrt{2m\bar{\phi}}}{\hbar}\exp[-2\frac{\sqrt{2m\bar{\phi}}}{\hbar}d]V, \tag{3.3}$$

which is consistent with Simmons's formula at low bias voltage [24]. According to Eq. 3.3, the transport properties are entirely determined by the average potential barrier height and we can discuss the TER effect in terms of the change of $\bar{\phi}$ with polarization reversal. We assume that the barrier height changes by $\delta\phi$ from $\bar{\phi}-\delta\phi/2$ (high conductance state, current density $J_>$) to $\bar{\phi}+\delta\phi/2$ (low conductance state, current density $J_<$) and define the TER ratio by TER$\equiv (J_> - J_<)/J_<$. Assuming that $\delta\phi$ is small and $J_> \gg J_<$, we arrive at

$$\text{TER} \equiv \frac{J_> - J_<}{J_<} \approx \exp[\frac{\sqrt{2m}}{\hbar}\frac{\delta\phi}{\sqrt{\bar{\phi}}}d]. \tag{3.4}$$

In the case of the 12 u.c. $BaTiO_3$ film, we find that $\bar{\phi} = 0.80$ eV and $\delta\phi = 0.16$ eV resulting in TER ≈ 80, which is consistent with our fit and experiment.

It is noteworthy that Eq. 3.4 predicts a dramatic increase in TER with increasing barrier thickness d. This increase is expected to be stronger than exponential due to the dependence of $\bar{\phi}$ and $\delta\phi$ on d (through the polarization-induced potential variation across the barrier), resulting in the increasing $\delta\phi/\bar{\phi}^{1/2}$ with film thickness. This tendency is indeed observed experimentally. If we assume that both $\bar{\phi}$ and $\delta\phi$ are constants, according to Eq. 3.4, an increase in film thickness by a factor of 2 is

expected to produce a TER that is a square of the value at the smaller thickness. In our case, an increase from $d = 2.4$ nm to $d = 4.8$ nm enhances TER from 7 to 80, that is, by a factor of 2 larger than what is expected from a simple exponential dependence.

3.6 Conclusion

In summary, we have demonstrated polarization-dependent resistive switching behavior of ultrathin films of $BaTiO_3$ at room temperature, manifesting the tunneling electroresistance effect predicted earlier. Upon polarization reversal, tunneling resistance changes by almost 2 orders of magnitude on a lateral scale of about 20 nm. Polarization retention is not affected by conductance measurements thus allowing multiple nondestructive polarization readouts and opening a possibility for application as noncharge based logical switches in nonvolatile memory devices.

References

[1] A. Sawa, Mater. Today **11**, 28 (2008).

[2] R. Waser and M. Aono, Nat. Mater. **6**, 833 (2007).

[3] A. Sawa, T. Fujii, M. Kawasaki, and Y. Tokura, Appl. Phys. Lett. **85**, 4073 (2004).

[4] C. Rossel, G. I. Meijer, D. Bremaud, and D. Widmer, J. Appl. Phys. **90**, 2892 (2001).

[5] F. A. Chudnovskii, L. L. Odynets, A. L. Pergament, and G. B. Stefanovich, J. Solid State Chem. **122**, 95 (1996).

[6] E. Y. Tsymbal and H. Kohlstedt, Science **313**, 181 (2006).

[7] J. Frenkel, Phys. Rev. **36**, 1604 (1930).

[8] M. Y. Zhuravlev, R. F. Sabirianov, S. S. Jaswal, and E. Y. Tsymbal, Phys. Rev. Lett. **94**, 246802 (2005).

[9] L. Esaki, R. B. Laibowitz, and P. J. Stiles, IBM Tech. Discl. Bull. **13**, 2161 (1971).

[10] C. Lichtensteiger, J.-M. Triscone, J. Junquera, and P. Ghosez, Phys. Rev. Lett. **94**, 047603 (2005).

[11] C. L. Jia, V. Nagarajan, J. Q. He, L. Houben, T. Zhao, R. Ramesh, K. Urban, and R. Waser, Nat. Mater. **6**, 64 (2007).

[12] D. D. Fong, G. B. Stephenson, S. K. Streiffer, J. A. Eastman, O. Auciello, P. H. Fuoss, and C. Thompson, Science **304**, 1650 (2004).

[13] D. A. Tenne, A. Bruchhausen, N. D. Lanzillotti-Kimura, A. Fainstein, R. S. Katiyar, A. Cantarero, A. Soukiassian, V. Vaithyanathan, J. H. Haeni, W. Tian, D. G. Schlom, K. J. Choi, D. M. Kim, C. B. Eom, H. P. Sun, X. Q. Pan, Y. L. Li, L. Q. Chen, Q. X. Jia, S. M. Nakhmanson, K. M. Rabe, and X. X. Xi, Science **313**, 1614 (2006).

[14] K. Szot, R. Dittmann, W. Speier, and R. Waser, Phys. Status Solidi **1**, R86 (2007).

[15] K. Szot, W. Speier, G. Bihlmayer, and R. Waser, Nat. Mater. **5**, 312 (2006).

[16] H. Kohlstedt, N. A. Pertsev, J. Rodr iguez, and R. Waser, Phys. Rev. B **72**, 125341 (2005).

[17] J. P. Velev, C.-G. Duan, K. D. Belashchenko, S. S. Jaswal, and E. Y. Tsymbal, Phys. Rev. Lett. **98**, 137201 (2007).

[18] A. Gruverman, D. Wu, H. Lu, Y. Wang, H. W. Jang, C. M. Folkman, M. Y. Zhuravlev, D. Felker, M. Rzchowski, C.-B. Eom, and E. Y. Tsymbal, Nano Lett. **9**, 3539 (2009).

[19] K. J. Choi, M. Biegalski, Y. L. Li, A. Sharan, J. Schubert, R. Uecker, P. Reiche, Y. B. Chen, X. Q. Pan, V. Gopalan, L.-Q. Chen, D. G. Schlom, and C. B. Eom, Science **306**, 1005 (2004).

[20] C. B. Eom, R. J. Cava, R. M. Fleming, J. M. Phillips, R. B. van Dover, J. H. Marshall, J. W. P. Hsu, J. J. Krajewski, and Jr. Peck, W. F., Science **258**, 1766 (1992).

[21] H. Kohlstedt, A. Petraru, K. Szot, A. Ruediger, P. Meuffels, H. Haselier, R. Waser, and V. Nagarajan, Appl. Phys. Lett. **92**, 062907 (2008).

[22] W. F. Brinkman, R. C. Dynes, and J. M. Rowell, J. Appl. Phys. **41**, 1915 (1970).

[23] J. P. Velev, C.-G. Duan, J. D. Burton, A. Smogunov, M. K. Niranjan, E. Tosatti, S. S. Jaswal, and E. Y. Tsymbal, Nano Lett. **9**, 427 (2009).

[24] J. G. Simmons, J. Appl. Phys. **34**, 1793 (1963).

Chapter 4

Interface Engineering for Polarization Retention Enhancement in Ferroelectric Junctions

Switchable ferroelectric polarization in ultrathin-film heterostructures offers a promising functional basis for novel nano-electronic devices. The main challenge for the implementation of such devices, however, is to overcome deleterious effects rendering ferroelectricity unstable, especially interface effects that become increasingly important as films are made thinner. In this chapter and the following two chapters, we have investigated three different approaches for enhancement of polarization stability in ultrathin ferroelectric heterostructures: the first approach is based on atomic level interface engineering to modify interfacial atomic terminations; the second approach involves a use of metal electrodes for more effective screening of polarization charges; and the third approach is based on electrode-ferroelectric interface modification by

introducing an additional polar molecular layer at the interface. In this chapter, we are going to investigate the first approach, that is, by engineering of interfacial atomic terminations.

4.1 Introduction

Maintaining and controlling a stable and switchable electric polarization in ferroelectric thin films down to the nanometer thickness range at room temperature is essential for exploiting the functionality of these materials for nano-electronics applications. Ferroelectric stability in thin films is largely determined by minimization of depolarizing field energy. The depolarizing field can be reduced by formation of screening charges at the film-electrode interfaces [1, 2, 3] or by forming a periodical stripe domain structure [4, 5, 6, 7, 8]. Although a free-electron charge in the metal electrodes is believed to provide the most efficient screening stabilizing the ferroelectric state down to nanometer dimensions [1], stable ferroelectricity has been also observed in nm-thick films without top electrodes [9, 10, 2, 3]. In this case, charge compensation at the free polar surfaces can be provided by ionic adsorbates, as has also been inferred from electrostatic force microscopy measurements [11] and first-principles calculations [3].

The presence of two electrodes is essential for the functional control and reproducibility of ferroelectric-based device characteristics. However, in some cases the screening provided by conductive electrodes appears to be less effective than screening by adsorbates on free surfaces exposed to air [10]. For example, deposition of the top $SrRuO_3$ electrodes on $BaTiO_3$ films results in severe relaxation to zero net polarization [8, 12]. This effect is a consequence of strong effective depolarizing fields due to incomplete screening or reduced interface capacitance effect. In addition, the presence of asymmetric interfaces may lead to a built-in electric field, whose direction

is independent of polarization orientation resulting in two non-equivalent polarization states [13]. In fact, such asymmetry may even destroy the stability of one of the polarization states, making the system only mono-stable in zero applied field and, therefore, non-ferroelectric. Addressing these detrimental effects is critical both for the fundamental understanding of the ferroelectric behavior at the nanoscale and related device performance.

One of the approaches to stabilize and even enhance ferroelectricity in nm-thick films has been offered by first-principles calculations suggesting that interface atomic structure and chemical bonding may significantly impact a ferroelectric state [14, 15]. In particular, interface engineering may be employed to eliminate the formation of a non-switchable interface dipole layer that is detrimental to ferroelectricity. In this chapter, we demonstrate an approach to stabilize that ferroelectric polarization in nm-thick ferroelectric films by interface engineering. We find that in the epitaxial $BaTiO_3$ films sandwiched between $SrRuO_3$ layers the RuO_2-BaO interface termination sequence, which commonly occurs during unit-cell-by-unit-cell growth, is detrimental to ferroelectric stability due to the presence of a pinned interface dipole. Our experimental measurements confirm that switchable ferroelectric polarization can be achieved by depositing a very thin layer of $SrTiO_3$ at the top interface to eliminate the unfavorable interface termination. These results indicate that interface engineering is a viable approach to stabilize ferroelectric polarization in ultrathin-film heterostructures.

Results described in this chapter have been published in ref. [16].

4.2 Polarization Behavior in $SrRuO_3/BaTiO_3/SrRuO_3$ Heterostructures

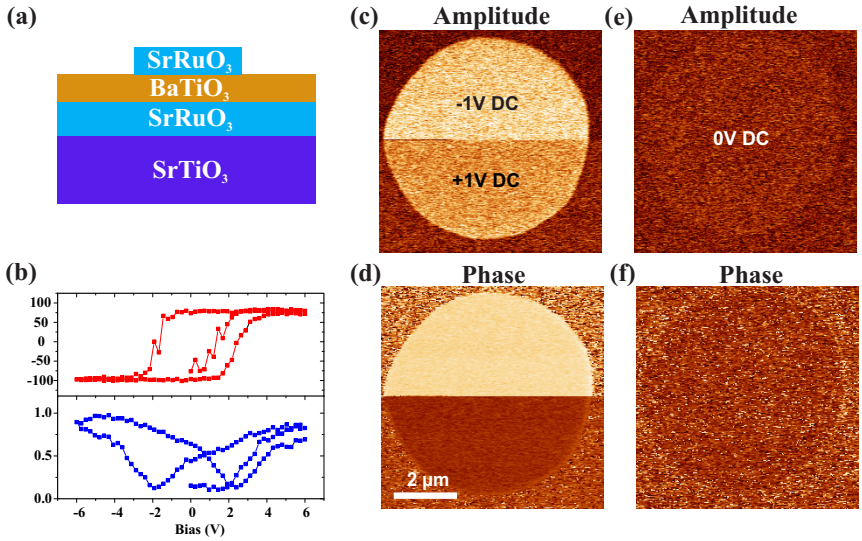

Figure 4.1: (a) A cross-section view of the $SrRuO_3/BaTiO_3/SrRuO_3$ heterostructure. (b) A PFM switching hysteresis loop obtained on the $BaTiO_3$ heterostructure showing typical ferroelectric switching behavior. (c, d) PFM amplitude (c) and phase (d) images on the electrode when maintaining ±1 V DC biases during imaging. (e, f) PFM amplitude (e) and phase (f) images without DC bias maintained during imaging.

Here we have used epitaxial single-cystalline $BaTiO_3$ films of 24 u.c. with epitaxial $SrRuO_3$ as top (3 nm) and bottom (30 nm) electrodes grown on (001)-$SrTiO_3$ substrates. The top electrodes have a circular shape with a diameter of 5 μm. A schematic cross section view of the resulting $SrRuO_3/BaTiO_3/SrRuO_3/SrTiO_3$ heterostructure is shown in Fig. 4.1(a).

PFM hysteresis loop obtained on the $BaTiO_3$ heterostructure (Fig. 4.1(b)) shows a typical ferroelectric switching behavior. However, PFM imaging shows that polarization is stable only when maintaining a constant DC bias (Fig. 4.1, (c)-(f)): there is strong PFM signal only when maintaining a ±1 V DC bias (Fig. 4.1, (c) and (d)), but no signal without DC bias maintained (Fig. 4.1, (e) and (f)), suggesting a fast

polarization relaxation in these heterostructures.

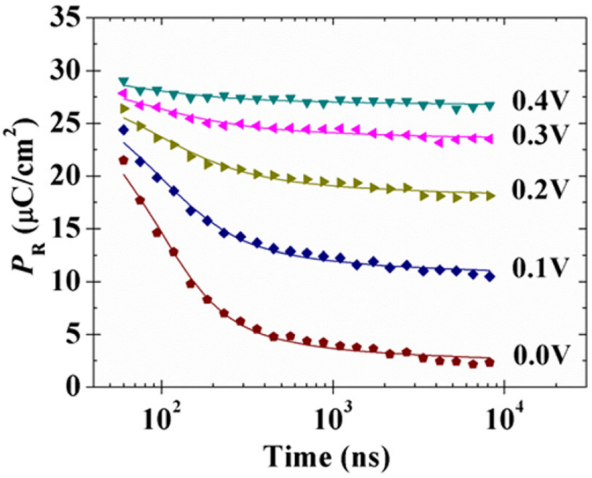

Figure 4.2: Polarization relaxation kinetics in the $SrRuO_3/BaTiO_3/SrRuO_3$ heterostructure, with or without maintaining a constant DC bias. Figure addapted from ref. [17].

The polarization relaxation kinetics in the $BaTiO_3$ heterostructures was obtained through measurement of the transient current by means of the positive up negative down (PUND) method [18, 19]. Due to the incomplete screening provided by the top $SrRuO_3$ electrode, polarization relaxation takes place within a very short time period (Fig. 4.2). As shown in Fig. 4.2, majority of the polarization decays away within micro-seconds when no DC bias is maintained. However, the depolarizing field can be compensated by maintaining an external DC bias through the electrodes, in which case a 0.4 V DC bias prevents from polarization relaxation and gives a stable polarization state. The depolarizing field, E_d, can be measured by changing the dc bias offset until relaxation is fully suppressed, which gives about 615±50 kV/cm (0.59±0.05 V) in the $BaTiO_3$ heterostructures.

4.3 Interface Engineering in $SrRuO_3/BaTiO_3/SrRuO_3$ Heterostructures

When $BaTiO_3$ is deposited in the [001] direction by pulsed laser deposition (PLD) it grows unit-cell-by-unit-cell. This results in a stoichiometric film with different atomic terminations on the two sides, i.e. one surface/interface will be BaO terminated while the other will be TiO_2 terminated. Therefore, since the usual AO-BO_2 stacking sequence is preserved at the interfaces in a heterostructure with $SrRuO_3$ electrodes, the bottom interface has the TiO_2-SrO termination sequence and the top interface has the RuO_2-BaO termination sequence. First-principle calculations in the $SrRuO_3/BaTiO_3/SrRuO_3$ heterostructure show that the RuO_2-BaO interface termination is detrimental to the polarization stability due to the presence of a pinned interface dipole. However, the detrimental effect of the RuO_2-BaO termination can be alleviated by replacing two $BaTiO_3$ unit cells at the top interface with $SrTiO_3$. This will make the interface termination sequence with the top electrode SrO-TiO_2 just as it is with the bottom interface. Calculations in such an engineered heterostructure reveal that both polarization states are stable [16, 20].

To verify the theoretical predictions we have grown several epitaxial $BaTiO_3$-based heterostructures with engineered interfaces (Fig. 4.3) and studied their switching behavior. Single-crystalline $BaTiO_3$ films (with a thickness of 24 unit cells) have been fabricated by pulsed laser deposition using atomically-controlled layer-by-layer growth on atomically smooth (001)-$SrTiO_3$ substrates with single-crystalline top and bottom $SrRuO_3$ electrodes [21, 22]. Control of epitaxial growth of the $BaTiO_3$ films has been ensured by in situ monitoring of RHEED intensity oscillations and RHEED patterns.

As has been proposed by the first-principle modeling, interface engineering has

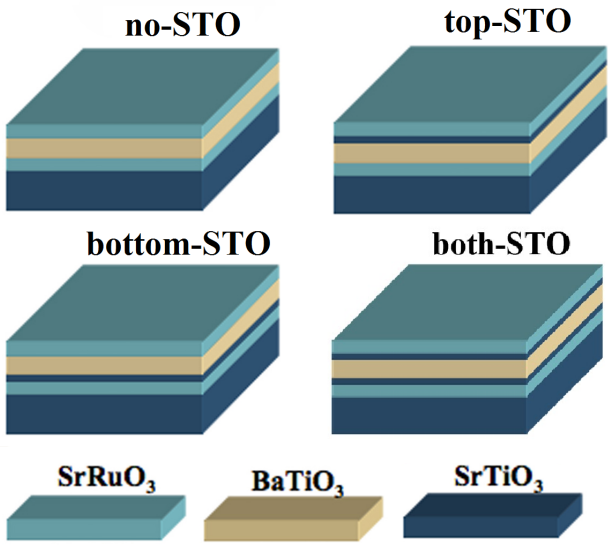

Figure 4.3: Schematic diagrams of the reference $SrRuO_3/BaTiO_3/SrRuO_3$ heterostructure (no-STO) and heterostructures with engineered top interface (top-STO), bottom interface (bottom-STO), and both interfaces (both-STO). Thickness of the $BaTiO_3$ and $SrTiO_3$ layers is 24 u.c. and 2 u.c., respectively.

been realized by introducing a $SrTiO_3$ layer with the thickness of 2 unit cells between the $BaTiO_3$ and $SrRuO_3$ layers (Fig. 4.3). The $SrRuO_3/BaTiO_3/SrRuO_3$, referred to as the reference, or no-STO heterostructure, and the corresponding heterostructures with engineered top, bottom and both interfaces are referred to as top-STO, bottom-STO and both-STO, respectively.

The high-resolution transmission electron microscopy (TEM) images revealed that the $BaTiO_3$ and $SrRuO_3$ layers being fully commensurate with the $SrTiO_3$ substrate and showed well-defined interfaces (Fig. 4.4, (a) and (b)). The intensity profile of the top interface in the $SrRuO_3/BaTiO_3/SrRuO_3$ (no-STO) heterostructure reveals a mixture of RuO_2-BaO and TiO_2-SrO terminations (Fig. 4.4(c)), while the bottom ferroelectric-electrode interface shows only TiO_2-SrO termination (Fig. 4.4(e)). Introduction of the $SrTiO_3$ layer at the top interface changes its termination to the TiO_2-BaO type (Fig. 4.4(d)), while the $SrTiO_3$ layer at the bottom interface leaves

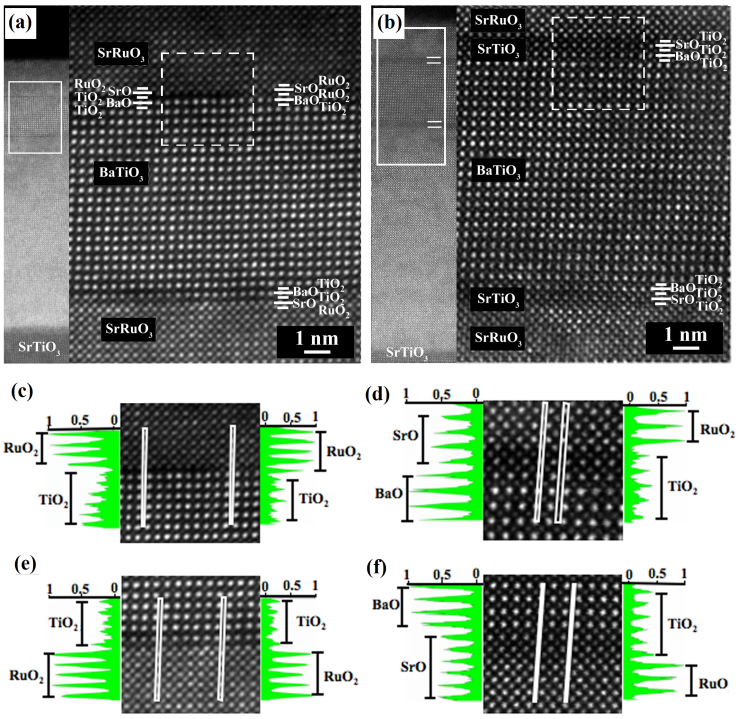

Figure 4.4: (a, b) STEM image of the no-STO (a) and both-STO (b) heterostructure. (c) The intensity profiles of the top interface of the no-STO heterostructure indicating a mixture of RuO_2-BaO and TiO_2-SrO terminations. (d) The intensity profiles showing the TiO_2-BaO termination at the top interface of the both-STO heterostructure. (e) The intensity profiles of the bottom interface of the no-STO heterostructure indicating termination of the TiO_2-SrO type. (f) The intensity profiles indicating the TiO_2-SrO termination at the bottom interface of the both-STO heterostructure. Figure addapted from ref. [16].

the TiO_2-SrO type termination intact (Fig. 4.4(f)).

Ferroelectric properties have been characterized using polarization hysteresis and scanning probe microscopy (SPM) measurements. The conventional hysteresis loops of all the heterostructures (Fig. 4.5(a) and (b)) show almost a paraelectric-type behavior with the remanent polarization well below 10 $\mu C/cm^2$ and a loop width of about 50 mV. To alleviate a strong nonlinear dielectric contribution effect and enable a more accurate measurement of such a low polarization value we applied a pulsed testing method [23]. In the no-STO heterostructure, the remanent polarization $2P_r$,

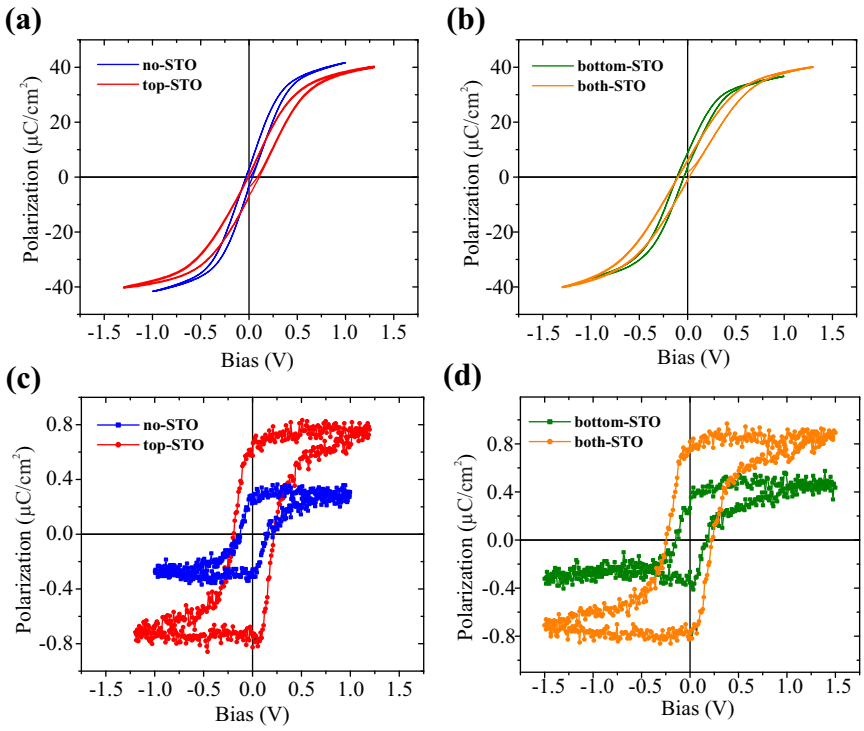

Figure 4.5: (a, b) Conventional and (c, d) remanent P–V hysteresis loops measured by pulsed testing in no-STO, top-STO, bottom-STO and both-STO heterostructures. The loops in (a) and (b) exhibit a width of 50 mV and low remanent polarization indicating an unstable polarization state. Note an almost 200% increase in the remanent polarization for the top-STO and both-STO samples in comparison with the no-STO and bottom-STO samples.

defined from the difference between the switched P^* and nonswitched $P^\wedge$ polarization signals, shown in Fig. 4.5(c), is about 0.5 μC/cm^2. (For comparison, the $2P_r$ value of 100 μC/cm^2 was reported for 200-nm-thick $BaTiO_3$ film on $GdScO_3$ substrate with $SrRuO_3$ top and bottom electrodes [21]). Changing the termination type at the top interface from RuO_2-BaO to TiO_2-BaO (top-STO) increases the remanent polarization by almost a factor of 3 to about 1.6 μC/cm^2, which is consistent with the changes predicted by the first-principle modeling. On the other hand, the remanent polarization value detected in the bottom-STO heterostructure (Fig. 4.5(d)) is very similar to that in the reference one (no-STO). This similarity can be expected as the in this

case the interface terminations are identical for both structures. Introduction of the $SrTiO_3$ layer at both top and bottom interfaces (both-STO) produces the same effect as modification of only the top interface (Fig. 4.5(d)). This finding confirms that the main mechanism behind the polarization retention enhancement is the change in termination structure at the top interface.

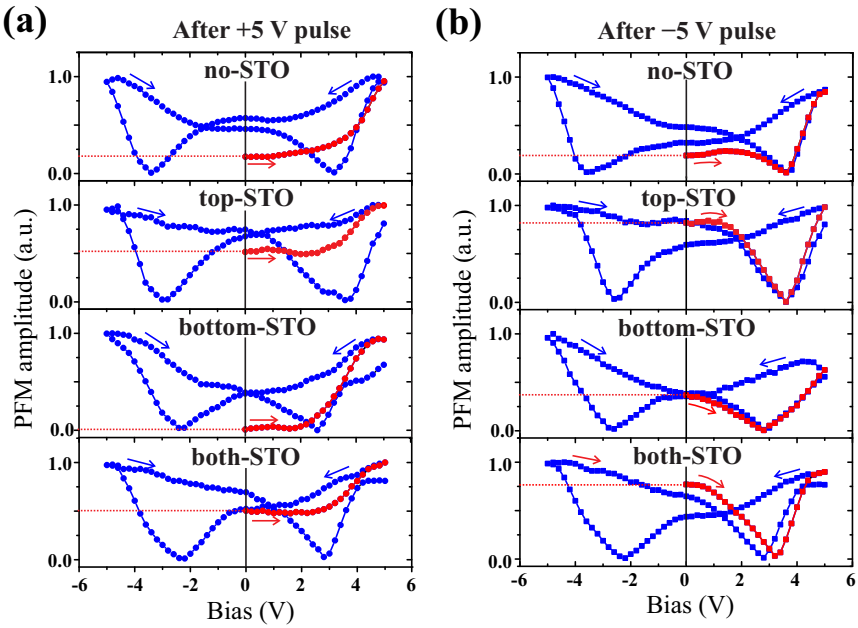

Figure 4.6: (a) PFM hysteresis loops for no-STO, top-STO, bottom-STO and both-STO heterostructures after application of +5 V poling pulses. (b) PFM hysteresis loops after application of −5 V poling pulses. The first quarters of the cycles are shown in red with arrows indicating the direction of voltage change. A difference in the initial (at zero bias) PFM amplitude illustrates a difference in remanent polarization values for different heterostructures.

While polarization hysteresis loop data are related to the net polarization, PFM provides information on the local (nanoscale) ferroelectric polarization. For the tetragonal (001)-oriented ferroelectrics as the $BaTiO_3$ films used in our study, the PFM amplitude signal is determined by the d_{33} piezoelectric coefficient which is proportional to the normal component of the local polarization: $d_{33} \sim ee_0P$ [24]. Ramping the poling dc voltage and monitoring the accompanying change in the PFM

amplitude signal allows testing the switching behavior at the spatial range determined by the tip-sample contact area (which is on the order of 10 nm in diameter). Local PFM switching measurements reveal a typical hysteretic polarization behavior for all the heterostructures (Fig. 4.6). In Fig. 4.6(a), before the measurements, the samples were poled by application of voltage pulses of +5 V, which is well above the threshold voltage. In PFM testing, the parameter directly related to the remanent polarization value is the initial piezoresponse amplitude signal at 0 V. It can be seen that for the no-STO and bottom-STO samples, the initial PFM amplitude and thus the local remanent polarization values are close to zero, which is consistent with zero net polarization revealed by P–V hysteresis measurements. On the other hand, the top-STO and both-STO samples exhibits a much higher initial PFM amplitude signal illustrating an enhanced remanent polarization in the sample with the engineered top interface. This effect was also observed when samples were poled by the opposite voltage(Fig. 4.6(b)).

To obtain a nanoscopic insight into the domain structure associated with the observed retention behavior, we employed a PFM imaging approach. Given that the $BaTiO_3$ films used in the present study are fully coherent with the $SrTiO_3$ substrates, which impose compressive stress, it is expected that the films would be in the polar state and only 180° domains would be present. It is also expected that to minimize the depolarizing energy, the system could break up into a system of 180° periodic antiparallel domains of equal volume fraction thus bringing the net polarization to zero. However, PFM imaging of the reference $SrRuO_3/BaTiO_3/SrRuO_3$ structure, which should be able to reveal domains as small as 10 nm in size [25], did not show any signature of the domain structure neither in the as-grown heterostructures nor after poling. This failure to observe domains by PFM can be explained if one recalls that the direct experimental measurements of ultrathin $BaTiO_3$ films by Raman

spectroscopy yielded a domain period value of 6.3 nm [26], which is below the PFM spatial resolution limit.

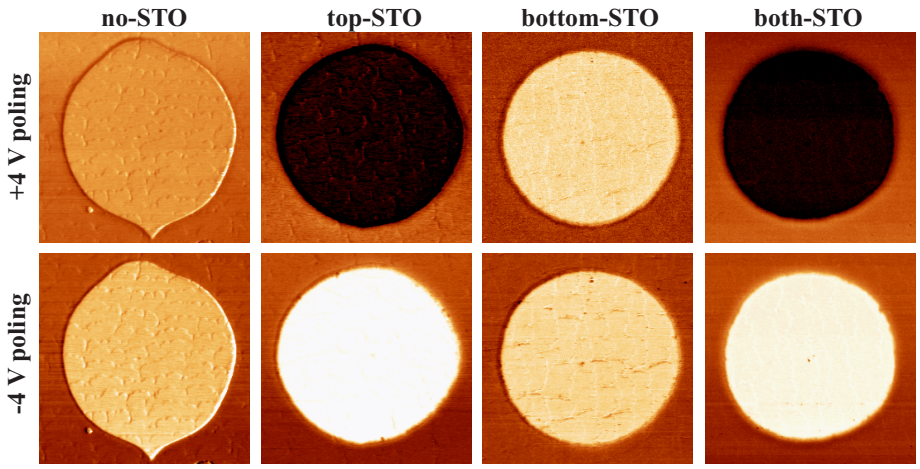

Figure 4.7: EFM images of the no-STO, top-STO, bottom-STO and both-STO heterostructures after poling by ±4 V pulses. Contrast inversion upon the change of the pulse polarity is attributed to the change of screening charge on the electrodes and indicates a presence of a switchable polarization with two stable states.

Nevertheless, the SPM approach still can offer additional support to the proposed mechanism of polarization retention enhancement. We have undertaken Electrostatic Force Microscopy (EFM) studies of the $BaTiO_3$ heterostructures subjected to poling by positive and negative voltage pulses. Note that EFM is sensitive to the presence of the surface charge and, as such, can address the issue of polarization stability by detecting the screening charge retained on the electrodes after poling. The EFM images of the reference sample and samples with engineered heterostructures after ±4 V poling are shown in Fig. 4.7. It can be seen that while poling of the reference no-STO sample by negative or positive pulses does not lead to any contrast change, the same poling procedure performed on the top-STO sample results in the appearance of strong reversible EFM contrast suggesting induction of the screening charge in the electrode. For the experimental conditions used in these measurements, dark EFM contrast corresponds to the positive charge signal (respectively, bright contrast

indicates negative charges). Based on this observation of the reversible EFM signal and its correlation with the sign of the poling voltage it can be confirmed that the resulting EFM contrast is indeed due to the screening charge on the electrodes and thus indicates a presence of stable polarization in the top-STO sample after poling. Additional tests show no sign of the EFM signal decay over the period of several hours has been detected suggesting high stability of the polarization states. Similarly, contrast inversion has been observed in the both-STO sample where both interfaces have been engineered. On the other hand, there is no change in the EFM signal after poling of the bottom-STO sample indicating zero net polarization. This effect is consistent with experimental results above showing that it is engineering of the top interface only that brings about polarization retention enhancement.

As a final note, it should be mentioned that the theoretically predicted effect of the interface engineering on polarization enhancement is only in qualitative agreement with the experiment. Interface engineering, while enhancing the remanent polarization by a factor of 3, did not lead to full recovery of polarization to its bulk value. This result illustrates a significant role of other effects and parameters in minimizing the depolarizing energy, such as polarization electronic screening and possible defect formation at the interfaces. In addition, stability enhancement by interface engineering in the first-principle calculations is based on eliminating an ideal *uniform* RuO_2-BaO termination at the top interface, whereas our experimental STEM data shows that the top interface of our $SrRuO_3/BaTiO_3/SrRuO_3$ sample exhibits a mixture of different interface terminations.

4.4 Conclusion

It has been suggested that significant retention enhancement can be achieved by depositing a very thin layer of $SrTiO_3$ at the interface to eliminate the unfavorable RuO_2-BaO interface termination, predicted by the first-principle calculations. Validity of the proposed approach to polarization stabilization has been confirmed by experimental measurements of polarization retention behavior in a set of model heterostructures with atomically engineered interfaces. The obtained results indicate that interface engineering is a viable approach to enhancement polarization retention in ultrathin ferroelectric heterostructures.

References

[1] J. Junquera and Ph. Ghosez, Nature **422**, 506 (2003).

[2] C. Lichtensteiger, J.-M. Triscone, J. Junquera, and Ph. Ghosez, Phys. Rev. Lett. **94**, 047603 (2005).

[3] D. D. Fong, A. M. Kolpak, J. A. Eastman, S. K. Streiffer, P. H. Fuoss, G. B. Stephenson, C. Thompson, D. M. Kim, K. J. Choi, C. B. Eom, I. Grinberg, and A. M. Rappe, Phys. Rev. Lett. **96**, 127601 (2006).

[4] S. K. Streiffer, J. A. Eastman, D. D. Fong, C. Thompson, A. Munkholm, M. V. RamanaMurty, O. Auciello, G. R. Bai, and G. B. Stephenson, Phys. Rev. Lett. **89**, 067601 (2002).

[5] D. D. Fong, G. B. Stephenson, S. K. Streiffer, J. A. Eastman, O. Auciello, P. H. Fuoss, and C. Thompson, Science **304**, 1650 (2004).

[6] B.-K. Lai, I. Ponomareva, I. I. Naumov, I. Kornev, H. Fu, L. Bellaiche, and G. J. Salamo, Phys. Rev. Lett. **96**, 137602 (2006).

[7] P. Aguado-Puente and J. Junquera, Phys. Rev. Lett. **100**, 177601 (2008).

[8] V. Nagarajan, J. Junquera, J. Q. He, C. L. Jia, R. Waser, K. Lee, Y. K. Kim, S. Baik, T. Zhao, R. Ramesh, P. Ghosez, and K. M. Rabe, J. Appl. Phys. **100**, 051609 (2006).

[9] V. Garcia, S. Fusil, K. Bouzehouane, S. Enouz-Vedrenne, N. D. Mathur, A. Barthelemy, and M. Bibes, Nature **460**, 81 (2009).

[10] A. Gruverman, D. Wu, H. Lu, Y. Wang, H. W. Jang, C. M. Folkman, M. Y. Zhuravlev, D. Felker, M. Rzchowski, C.-B. Eom, and E. Y. Tsymbal, Nano Lett. **9**, 3539 (2009).

[11] S. V. Kalinin and D. A. Bonnell, Phys. Rev. B **63**, 125411 (2001).

[12] D. J. Kim, J. Y. Jo, Y. S. Kim, Y. J. Chang, J. S. Lee, Jong-Gul Yoon, T. K. Song, and T. W. Noh, Phys. Rev. Lett. **95**, 237602 (2005).

[13] A. K. Tagantsev and G. Gerra, J. Appl. Phys. **100**, 051607 (2006).

[14] C. G. Duan, R. F. Sabirianov, W. N. Mei, S. S. Jaswal, and E. Y. Tsymbal, Nano Lett. **6**, 483 (2006).

[15] M. Stengel, D. Vanderbilt, and N. A. Spaldin, Nat. Mater. **8**, 392 (2009).

[16] H. Lu, X. Liu, J. D. Burton, C.-W. Bark, Y. Wang, Y. Zhang, D. J. Kim, A. Stamm, P. Lukashev, D. A. Felker, C. M. Folkman, P. Gao, M. S. Rzchowski, X. Q. Pan, C.-B. Eom, E. Y. Tsymbal, and A. Gruverman, Adv. Mater. **24**, 1209 (2012).

[17] A. Stamm, D. J. Kim, H. Lu, C. W. Bark, C. B. Eom, and A. Gruverman, Appl. Phys. Lett. **102**, 092901 (2013).

[18] C. Dehoff, B. J. Rodriguez, A. I. Kingon, R. J. Nemanich, A. Gruverman, and J. S. Cross, Rev. Sci. Instrum. **76**, 023708 (2005).

[19] A. K. Tagantsev, I. Stolichnov, N. Setter, J. S. Cross, and M. Tsukada, Phys. Rev. B **66**, 214109 (2002).

[20] X. Liu, Y. Wang, P. V. Lukashev, J. D. Burton, and E. Y. Tsymbal, Phys. Rev. B **85**, 125407 (2012).

[21] K. J. Choi, M. Biegalski, Y. L. Li, A. Sharan, J. Schubert, R. Uecker, P. Reiche, Y. B. Chen, X. Q. Pan, V. Gopalan, L.-Q. Chen, D. G. Schlom, and C. B. Eom, Science **306**, 1005 (2004).

[22] C. B. Eom, R. J. Cava, R. M. Fleming, J. M. Phillips, R. B. van Dover, J. H. Marshall, J. W. P. Hsu, J. J. Krajewski, and Jr. Peck, W. F., Science **258**, 1766 (1992).

[23] D. H. Chang, Y. S. Yoon, and S. J. Kang, J. Korean Phys. Soc. **38**, 277 (2001).

[24] A. F. Devonshire, Philos. Mag. **42**, 1065 (1951).

[25] S. V. Kalinin, B. J. Rodriguez, S.-H. Kim, S.-K. Hong, A. Gruverman, and E. A. Eliseev, Appl. Phys. Lett. **92**, 152906 (2008).

[26] D. A. Tenne, P. Turner, J. D. Schmidt, M. Biegalski, Y. L. Li, L. Q. Chen, A. Soukiassian, S. Trolier-McKinstry, D. G. Schlom, X. X. Xi, D. D. Fong, P. H. Fuoss, J. A. Eastman, G. B. Stephenson, C. Thompson, and S. K. Streiffer, Phys. Rev Lett. **103**, 177601 (2009).

Chapter 5

Metal Electrodes for Polarization Retention Enhancement in Ferroelectric Tunnel Junctions

5.1 Introduction

Polarization stability of ultrathin ferroelectric barriers with top electrodes becomes a serious issue due to large depolarizing field. It has been shown that polarization screening by metal oxide electrodes is less effective than by elemental metals [1], leading to progressive loss of polarization retention and thus a relaxation of the TER effect. In this chapter, we employed metal electrodes to achieve stable polarization and resistance states in the FTJs. it was found that the tunneling resistance of the FTJ could be continuously tuned by varying the writing voltage amplitude and duration thereby achieving the OFF/ON resistance ratio of up to 10^5 % at room temperature. The FTJ devices with tunable resistance states, referred to as ferroelectric tunnel memristors (FTMs), can be considered as a new paradigm for non-volatile memories and

adaptive electronic circuit elements. Employing of memristors can radically enhance the computational power and energy efficiency of electronic systems.

Results described in this chapter have been published in ref. [2].

5.2 Polarization Reversal and Resistive Switching in Ferroelectric Tunnel Junctions with Metal Electrodes

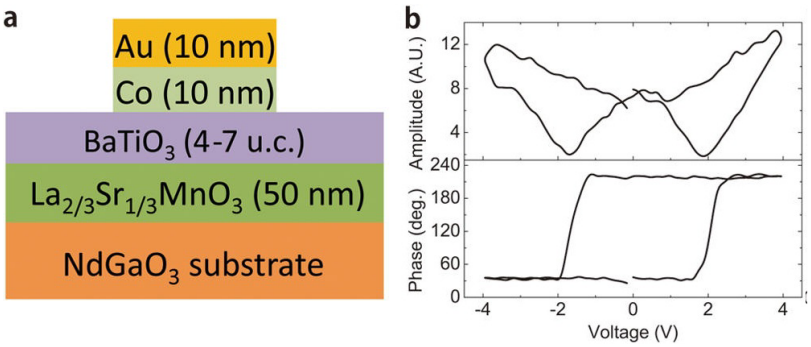

Figure 5.1: (a) A schematic cross-section of the junction. (b) PFM hysteresis loops measured through the junction with the 4-u.c.-thick $BaTiO_3$ barrier. Figure addapted from ref. [2].

Resistive switching measurements have been carried out on the $BaTiO_3$-based tunnel junctions with Co as top electrode and $La_{2/3}Sr_{1/3}MnO_3$ as bottom electrode, as schematically shown in Fig. 5.1. Epitaxial single-crystalline $BaTiO_3$ films of 4 to 7 u.c. have been grown with layer-by-layer control on (110)-$NdGaO_3$ substrate sandwiched with $La_{2/3}Sr_{1/3}MnO_3$ as bottom electrode. The top Co electrodes (10 nm) of 5 μm in diameter have been fabricated ex-situ by lift-off and sputtering followed by photolithographic patterning through image reversal lithography. Co is then covered by Au (10 nm) to prevent from oxidation. PFM switching spectroscopy obtained

through the junction shows typical ferroelectric switching behavior, demonstrating ferroelectricity in these junctions (Fig. 5.1(d)).

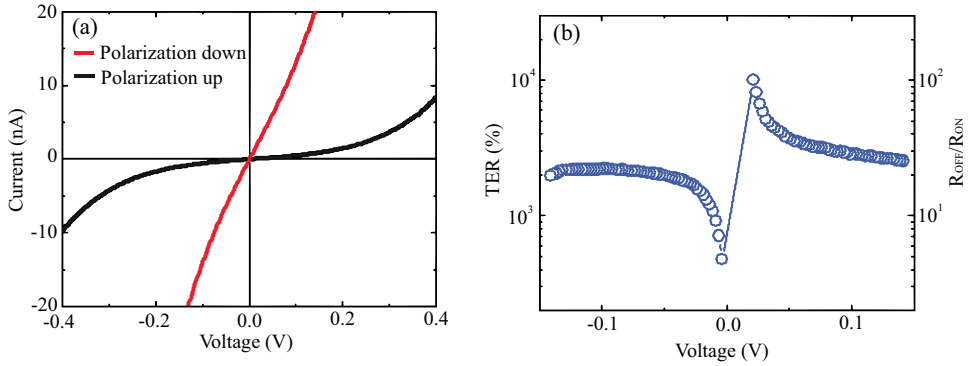

Figure 5.2: The tunneling electroresistance effect in the $Co/BaTiO_3/(La,Sr)MnO_3$ tunnel junctions. (a) I–V curves for polarization up (OFF) and polarization down (ON) states in the 6 u.c. $BaTiO_3$ junction. (b) The TER or resistance ratio for the ON and OFF states shows a high value over 10^3 %.

The $Co/BaTiO_3/(La,Sr)MnO_3$ junctions show a clear resistive switching behavior upon reversal of $BaTiO_3$ polarization by application of voltage pulses. I–V characteristics measured on the junction for polarization up (black) and polarization down (red) states in the 6 u.c. $BaTiO_3$ junctions (Fig. 5.2(a)) show different tunneling resistances: The downward polarization state shows much higher conductivity (ON state) than the upward polarization state (OFF state), giving a tunneling electroresistance effect higher than 10^3 % (Fig. 5.2(b)).

The junctions with the Co electrodes fabricated at a high oxygen base pressure (HBP) of 10^{-4} Torr exhibit fast decay and instability of resistive switching (Fig. 5.3, (a) and (c)). The I–V curves measured with a certain delay (0.1s to 100 s) after application of the poling bias show strong dependence of the delay time, especially for the ON state, which relaxes to the OFF state after 100 s. The TER relaxes as a power law: $R_{OFF}/R_{ON} \sim t^{-\alpha}$, where α is a fitting parameter. This relaxation of the resistance states indicates that polarization is not stable after application of voltage

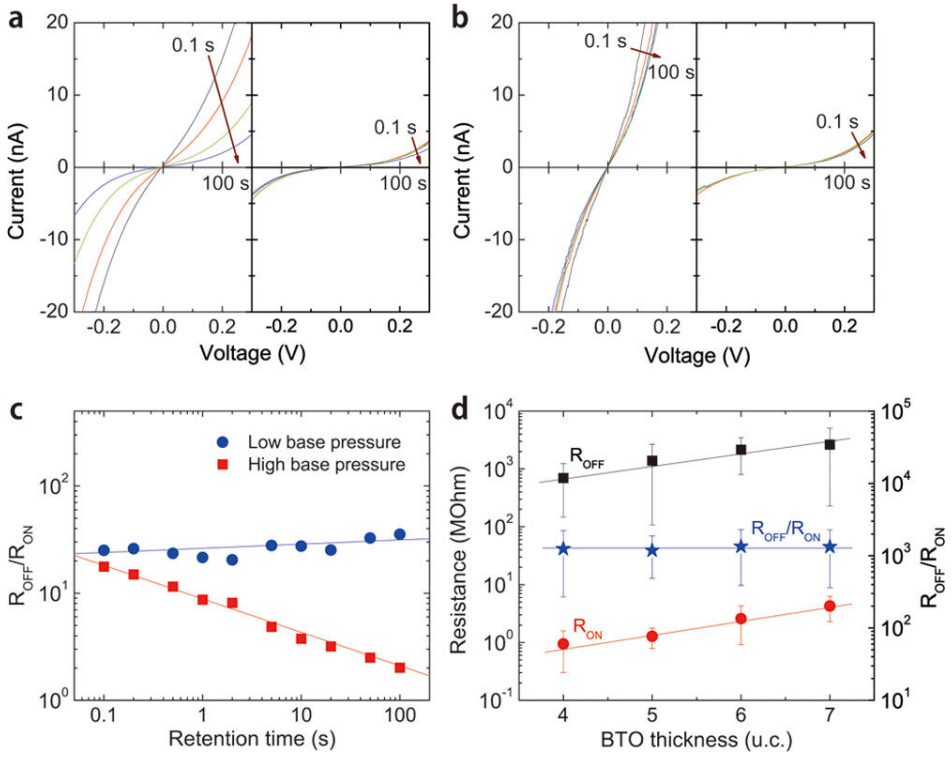

Figure 5.3: (a, b) Temporal evolution of the I–V curves measured in the 6-u.c.-thick $BaTiO_3$ junctions with the top Co electrode fabricated under (a) high base pressure and (b) low base pressure. Writing pulse voltage was fixed at ±6 V. (c) R_{OFF}/R_{ON} resistance ratio, calculated from (a) and (b). The solid lines represent power-law fitting of the time-dependent behavior. (d) Differential resistance for OFF and ON states and their ratio, R_{OFF}/R_{ON}, as a function of the $BaTiO_3$ barrier thickness in the LBP-processed junctions. Writing pulse was at ±8 V, 1 ms. Figure addapted from ref. [2].

pulses.

The measured TER effect shows much stronger retention for those with Co electrodes processed at a low base pressure (LBP) of 10^{-6} Torr, the junctions exhibit a much more stable resistive switching effect with neither ON nor OFF states showing any noticeable sign of relaxation (Fig. 5.3(b)). Fig. 5.3(c) shows a comparison of resistance retention behavior for Co deposition with high and low oxygen pressure.

The fact that the TER effect is very sensitive to the Co processing condition indicates the importance of metal-ferroelectric interface in stabilizing the ferroelectric

polarization in the ultrathin ferroelectric layer. Here, in our case, high O_2 pressure may lead to oxidation of Co, resulting an additional cobalt oxide layer at the interface and thus reduces the screening effect.

In the LBP-processed junctions, Fig. 5.3(d) indicates that the resistance for ON and OFF states increases exponentially with $BaTiO_3$ thickness, however, the resistance ratio R_{OFF}/R_{ON} remains nearly constant for $BaTiO_3$ thickness ranging from 4 to 7 u.c. This observation is in striking contrast to the behavior previously reported for FTJs where R_{OFF}/R_{ON} increased exponentially with ferroelectric barrier thickness [3], consistent with theoretical predictions for the TER effect [4]. Note that the change in resistance due to switching between OFF and ON states is much larger than the respective change in resistance with the $BaTiO_3$ thickness. This fact suggests that the properties of the interface, rather than bulk properties of the ferroelectric barrier, are responsible for the observed resistive switching behavior.

5.3 Tunable Resistance—Memristive Behavior in Ferroelectric Tunnel Junctions

Furthermore, the R_{OFF}/R_{ON} resistance ratio can be tuned continuously by several orders of magnitude by varying the writing voltage amplitude and duration. Figure 5.4(a) shows a set of the I–V curves measured on the 4 u.c. $BaTiO_3$ junctions after poling by voltage pulses of various amplitudes, where the tunneling conductance changes as a function of the writing pulse voltages. The continuously tunable resistance states are depicted in Fig. 5.4(b). Starting at 0 V where the junction is in the ON state (low resistance state), application of positive voltage pulses above the coercive voltage of 2 V gradually increases the resistance and sets the junction to

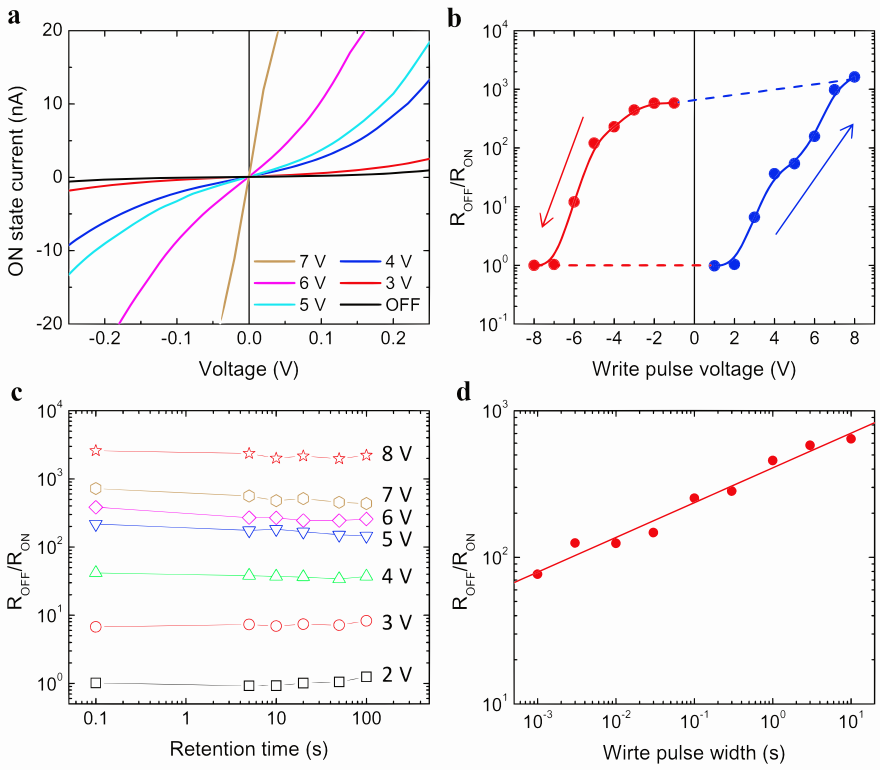

Figure 5.4: (a) I–V curves measured in the 4-u.c.-thick $BaTiO_3$ junctions after application of the writing pulses with amplitudes varying in the range from 3 to 7 V (pulse width fixed at 1 ms). (b) R_{OFF}/R_{ON} as a function of the writing pulse amplitude from (a). The lines are the guides for eyes. (c) The retention behavior of R_{OFF}/R_{ON} as a function of delay time between the write pulse and the I–V measurement from 0.1 s to 100 s. (d) The R_{OFF}/R_{ON} ratio as a function of writing pulse duration (pulse amplitude fixed at 6 V). The solid line is a fit to the power-law. Figure addapted from ref. [2].

the OFF state (high resistance state). The R_{OFF}/R_{ON} resistance ratio continuously increases and reaches 10^5 % at the writing bias of 8 V. Reversing of the voltage pulses results to a continuously decrease of the resistance and finally sets to the ON states again, forming a resistance hysteresis of the junction. In each state the resistance is stable at least for as long as 100 s (Fig. 5.4(c)). In the meanwhile, the resistance ratio is tunable and varies with the writing pulse duration (Fig. 5.4(d)). A longer positive (or negative) pulse sets the junction in a higher (or lower) resistance state.

The tunable and nonvolatile nature of electrical resistance of the FTJ allows us to treat it as a memristor. The resistance state of the memristor is determined by the history of the applied voltage so that can be modulated electrically in an analogous manner [5, 6]. This property distinguishes resistive switching in the ferroelectric tunnel memristor (FTM) from the TER effect in FTJs, which is realized in the form of two nonvolatile resistance states with fixed resistance values [7].

5.4 Interfacial Layer Model of Tunable Resistance

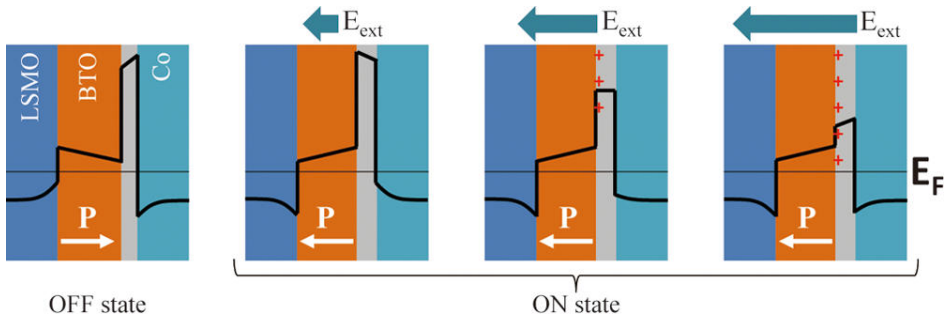

Figure 5.5: Schematic illustration of the energy barrier diagrams for the OFF and ON states as a function on the external electric field E_{ext}. The gray layer between the Co and BTO layers is the passive dielectric layer of CoO_x. Figure addapted from ref. [2].

The voltage dependence of $R_{\text{OFF}}/R_{\text{ON}}$, which at the same time is independent of the thickness of the $BaTiO_3$ barrier, implies a mechanism different from the mechanism of the TER effect in FTJs. Given that the resistive switching is very sensitive to the processing conditions of the top electrode, we suggest that charge migration and accumulation at the Co/$BaTiO_3$ interface facilitated by its defect structure play an important role in the observed effect [8, 9]. Note that Co tends to oxidize, which may lead to the formation of the passive dielectric layer with an increased density of oxygen vacancies at the top $BaTiO_3$ interface in the LBP-processed FTJs. It is

suggested that the barrier height associated with this layer is higher in comparison with the barrier of $BaTiO_3$ and provides significant contribution to the resistance behavior. Under a positive bias applied to the top electrode, oxygen vacancies accumulate at the $CoO_x/BaTiO_3$ interface, effectively reducing the barrier height and decreasing the resistance of the ON state (Fig. 5.5). Decrease in resistance with the writing pulse amplitude and duration is consistent with this mechanism. Enhanced retention of the resistive switching in the LBP-processed FTJs can be explained by more effective domain pinning by interface defects. A negative bias induces a dissipation of accumulated charges at the interface and/or a reduction of Co oxide at the interface, switching the heterostructure into the high-resistance state.

5.5 Role of Ferroelectric Polarization in Memristive Behavior

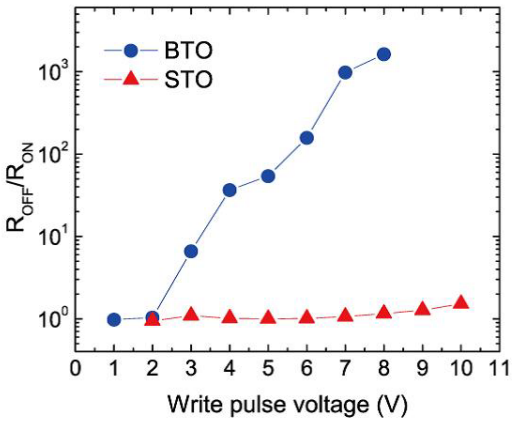

Figure 5.6: The $R_{\mathrm{OFF}}/R_{\mathrm{ON}}$ ratio measured in the 4-u.c.-$BaTiO_3$ and 4-u.c.-$SrTiO_3$ junctions as a function of the 1 ms writing pulse amplitude. Figure addapted from ref. [2].

While the tunable resistive switching is determined mainly by the interface, the

ferroelectric layer still plays an important role in the resistive behavior of FTM as an electrically switchable barrier for the tunneling current. This is evident from the fact that substituting the $BaTiO_3$ layer with the $SrTiO_3$ layer of the same thickness results in almost complete annihilation of the resistive switching effect (Fig. 5.6). Also, an onset of the resistive switching at 2 V (Fig. 5.4(b)) coincides with the coercive field of the $BaTiO_3$ film (Fig. 5.1(d)), which suggests that polarization in $BaTiO_3$ affects the charge accumulation at the interface and determines the hysteretic nature of the resistive switching effect. Specifically, the negative bound polarization charges at $Co/BaTiO_3$ interface facilitate accumulation of oxygen vacancies resulting in the reduced energy barrier of the interface and lowering the resistance of the ON state as shown in Fig. 5.5.

5.6 Conclusion

In summary, we have stablized the polarization states and achieved strong retention of the resistance states by employing Co as top electrodes in ultrathin $BaTiO_3$ tunnel junctions. In addition, we have demonstrated a ferroelectric tunnel memristor, which exhibits tunable, nonvolatile, hysteretic resistance switching behavior with the OFF/ON resistance ratio reaching 10^5 %. Tunable resistive switching is attributed to the field-induced charge redistribution at the ferroelectric–electrode interface resulting in the modulation of the interface barrier height. A large value of the observed effect, its long-time retention, and the robustness of the resistance state against the read-out process make the ferroelectric tunnel memristor a promising device concept for next-generation of nonvolatile memories and logic neuromorphic circuits.

References

[1] V. Nagarajan, J. Junquera, J. Q. He, C. L. Jia, R. Waser, K. Lee, Y. K. Kim, S. Baik, T. Zhao, R. Ramesh, P. Ghosez, and K. M. Rabe, J. Appl. Phys. **100**, 051609 (2006).

[2] D. J. Kim, H. Lu, S. Ryu, C.-W. Bark, C.-B. Eom, E. Y. Tsymbal, and A. Gruverman, Nano Lett. **12**, 5697 (2012).

[3] V. Garcia, S. Fusil, K. Bouzehouane, S. Enouz-Vedrenne, N. D. Mather, A. Barthélémy, and M. Bibes, Nature **460**, 81 (2009).

[4] M. Y. Zhuravlev, R. F. Sabirianov, S. S. Jaswal, and E. Y. Tsymbal, Phys. Rev. Lett. **94**, 246802 (2005).

[5] D. B. Strukov, G. S. Snider, D. R. Stewart, and R. S. Williams, Nature **453**, 80 (2008).

[6] S. D. Ha and S. Ramanathan, J. Appl. Phys. **110**, 071101 (2011).

[7] E. Y. Tsymbal, A. Gruverman, V. Garcia, M. Bibes, and A. Barthélémy, MRS Bull. **37**, 138 (2012).

[8] R. Waser, R. Dittmann, G. Staikov, and K. Szot, Adv. Mater. **21**, 2632 (2009).

[9] J. J. Yang, M. D. Pickett, X. Li, D. A. A. Ohlberg, D. R. Stewart, and R. S. Williams, Nat. Nanotechnol. **3**, 429 (2008).

Chapter 6

Use of Interfacial Polar Layer for Polarization Retention Enhancement in Ferroelectric Tunnel Junctions

6.1 Introduction

It has been shown in Chapter 3 that polarization is switchable and stable in ultrathin $BaTiO_3$ films without top electrode, which indicates that screening is effective by polar adsorbates on free surfaces exposed to air, while there is always a problem of effective screening of the depolarizing field when top electrode is present. It is reasonable to think that by adding an additional polar molecular layer at the electrode-ferroelectric interface in a real FTJ structure with top and bottom electrodes, it may help to enhance the screening effect and thus enhance the polarization retention.

On the other hand, resistive switching behavior of FTJs to a large extent is gov-

erned by the electric potential across the ferroelectric layer [1]. Parameters of the potential barrier are highly sensitive to the electrical boundary conditions, which opens a possibility to control tunneling resistance by engineering the interfaces of the FTJs. It has been also found that the film-electrode interface properties play critical role in the tunneling electroresistance (TER) effect resulting in tunable resistivity and affecting polarization retention [2, 3]. Ionic displacement and orbital hybridization at the interfaces, non-stoichiometry and charge defects affect the boundary conditions, which determine the potential barrier profile. Most recently it has been demonstrated that significant enhancement of the electroresistance effect can be achieved by using a semiconducting material as one of the FTJs electrodes [4]. TER enhancement is a result of switching between accumulation and depletion of the majority carriers at the semiconductor interface due to a ferroelectric field effect. Another method makes use of the ferroelectrically induced metal-insulator transition in the interfacial oxide layer, which leads to significant changes in the potential barrier thereby pushing the TER ratio even higher [5]. These observations show that the interface engineering could be a very efficient approach to amplify the resistive switching effect of FTJs.

In this chapter, we demonstrate a significant enhancement of polarization retention in FTJ realized by introducing a polar molecular layer at the electrode-ferroelectric interface. We also show, that this approach results in almost two orders of magnitude enhancement of the TER effect (3×10^5 %). The obtained results provide a general approach for interface-facilitated enhancement of TER, which can be adapted for use in the FTJ devices.

6.2 Materials and Methods

To utilize this approach for enhancement of polarization retention and TER control, we explore the polarization switching and resistive switching of the $BaTiO_3$-based tunnel junctions with graphene and $La_{0.67}Sr_{0.33}MnO_3$ as top and bottom electrodes, respectively, in the graphene/$BaTiO_3$/(La,Sr)MnO_3/$SrTiO_3$ tunnel junctions. Epitaxial single-crystalline $BaTiO_3$ films with the thickness of 6 unit cells (u.c.) have been fabricated by pulsed layer deposition on atomically smooth (001) $SrTiO_3$ substrates [6].

Graphene films were grown by the chemical vapor deposition (CVD), and graphene patches with a size of 10×30 μm^2 based on a CVD graphene was prepared by electron beam lithography (EBL). Control of the graphene-ferroelectric interface properties has been enabled by introducing an additional molecular layer formed during the transfer of graphene to the ferroelectric surface in different solvents. Specifically, we have studied the polarization stability and resistive switching in FTJs, which incorporate H_2O and NH_3 layers at the graphene/$BaTiO_3$ interfaces. From here on, we denote samples with graphene electrodes transferred in ammonia as Gr/NH_3/BTO and samples with graphene transferred in water as Gr/H_2O/BTO.

6.3 Enhancement of Polarization Retention by a Polar Interfacial Layer

First, we tested the reliability of electrical control of polarization in the FTJ utilizing graphene as a top electrode by performing PFM imaging of the polarization states on the 10×30 μm^2 graphene patches (Fig. 6.1(a)) before and after voltage pulse application. Figure 6.1(b) shows the topographic image of the edge of the graphene

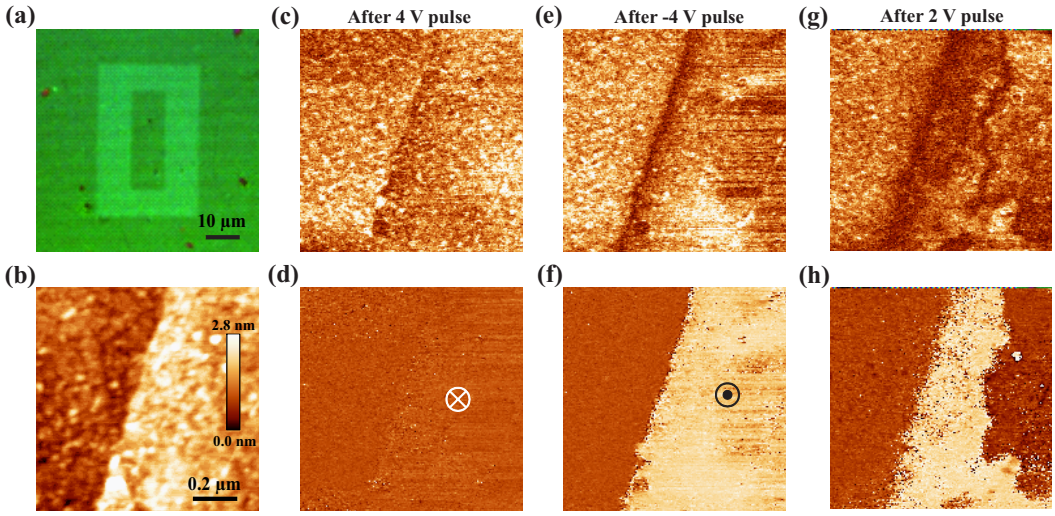

Figure 6.1: PFM testing of the $Gr/NH_3/BTO$ junction. (a) An optical image of the 10×30 μm^2 graphene patch. (b) Topographic image of the edge of the graphene patch (on the right) along with the segment of the bare $BaTiO_3$ surface (on the left). (c-h) PFM amplitude (c,e,g) and phase (d,f,h) images of the $Gr/NH_3/BTO$ junction after application of 4V (c,d), -4 V (e,f) and 2 V (g,h) pulses, showing changes of the domain structures under graphene.

patch (on the right) along with the segment of the bare $BaTiO_3$ surface (on the left) of the $Gr/NH_3/BTO$ junction. PFM testing of the FTJs shows that as-grown $BaTiO_3$ films are in a single-domain state with polarization oriented downward (toward the bottom interface). Polarization states resulting from application of the voltage pulses by the PFM tips in contact with the graphene patch are shown in Fig. 6.1, (c)-(h). It can be clearly seen that polarization can be switched either completely or in small fractions depending on the pulse amplitude (or duration) indicating an efficient polarization control with external voltage. Note that polarization state of the exposed $BaTiO_3$ film remains unchanged.

Polarization switching in the FTJs has been also confirmed by PFM hysteresis loop measurements. Figure 6.2 compares PFM switching hysteresis loops obtained on bare $BaTiO_3$ surface (a) and through graphene (b). In both cases, the hysteresis loops shows typical ferroelectric polarization switching. It can be seen that the FTJ devices

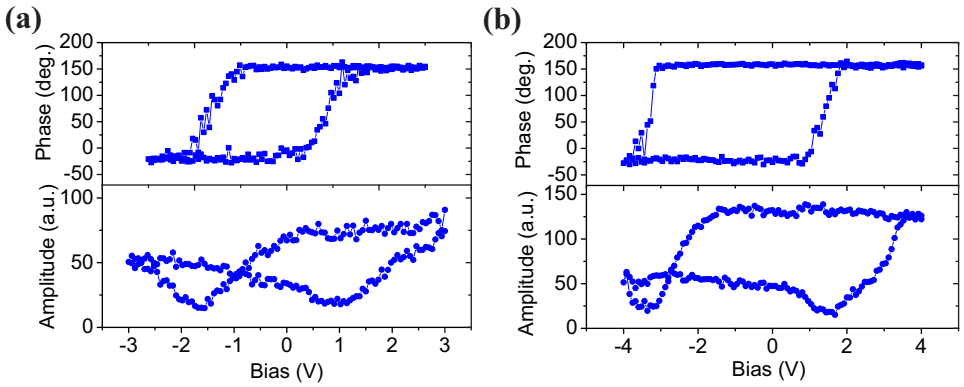

Figure 6.2: PFM switching hysteresis loops measured (a) on bare $BaTiO_3$ and (b) through graphene on graphene/NH_3/$BaTiO_3$. Both cases show typical ferroelectric polarization switching hysteresis.

are characterized by more asymmetric loops in comparison with the bare $BaTiO_3$ film. While this can be a consequence of an asymmetric band structure due to the dielectric layer inserted at the FTJs top interface, we maintain that the main reason for this effect is higher conductivity of the FTJs with downward polarization, which results in strong leakage and high energy loss when switching from the downward to the upward polarization state.

As for polarization retention, it has been found that introduction of the NH_3 layer results in much more stable polarization (with retention time of at least several days for both polarization states), while only one polarization state (downward) is stable in the Gr/H_2O/BTO junctions. Figure 6.3 illustrates a difference in polarization retention between Gr/H_2O/BTO (a) and Gr/NH_3/BTO (b) junctions. In the case of a H_2O interfacial layer, the PFM signal quickly decays to zero within seconds after pulse application, indicating an unstable polarization state, while there is stable remnant PFM amplitude signal corresponding to the downward polarization state. In fact, it is not possible to unambiguously conclude whether polarization reversal can be realized in the Gr/H_2O/BTO junctions at all. In the case of a NH_3 interfacial

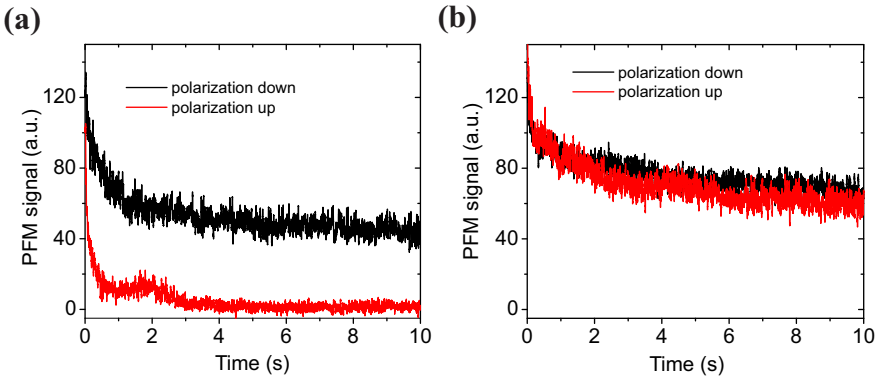

Figure 6.3: Comparison of polarization retention behavior in the $Gr/NH_3/BTO$ and $Gr/H_2O/BTO$ junctions. Time dependenc of the PFM amplitude in (a) $Gr/H_2O/BTO$ and (b) $Gr/NH_3/BTO$ junctions for opposite polarization states. Only downward polarization is stable in the $Gr/H_2O/BTO$ junctions while upward polarization decays within seconds after application of the switching voltage pulse. In the $Gr/NH_3/BTO$ junctions both polarization states are stable after voltage pulses on graphene for graphene/NH_3/BTO.

layer, both of polarization up and down states shows strong retention, indicating an enhancement of polarization stability by introducing an interfacial NH_3 layer.

6.4 Effect of the Polar Layer on Tunneling Electroresistance

Next, we have characterized the resistive switching behavior by measuring the current-voltage (I–V) characteristics of the FTJs as a function of their polarization state using the conductive AFM (C-AFM) approach. Given its superior retention properties, we have focused on the $Gr/NH_3/BTO$ junctions. Figure 6.4(a) shows the I–V curves measured after complete switching of the $BaTiO_3$ polarization either up or down by applying the ±4 V voltage pulses. It can be seen that there is a giant resistance change upon polarization reversal: the OFF/ON ratio R_{OFF}/R_{ON} reaches a level of more than 3500 for zero-bias limit and can be as large as 6000 for the bias range

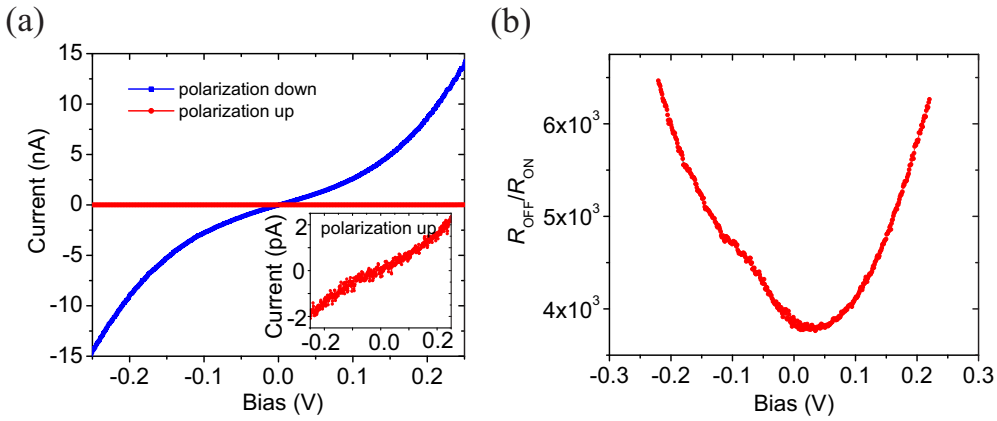

Figure 6.4: (a) The I–V curves measured on the Gr/NH_3/BTO junction for polarization up (red) and polarization down (blue) states. The inset shows the rescaled I–V for polarization up state. (b) $R_{\mathrm{OFF}}/R_{\mathrm{ON}}$ resistance ratio as a function of the reading bias. The resistance ratio is about 3500 for zero-bias limit, and reaches about 6000 for the bias of ±0.2 V.

of ±0.2 V (Fig. 6.4(b)). This effect is much stronger than that reported earlier in ultrathin $BaTiO_3$ films of the same thickness (6 u.c.) with the TER magnitude of only 7 [7]. The observed effect is highly consistent: the I–V curves measured at different locations on the surface of the graphene patch are reproducible and show no degradation with time within the period of polarization stability. In addition, C-AFM measurements performed on several different samples show little junction-to-junction variations. Additional PFM imaging after I–V measurements shows that polarization is not affected by the I–V measurements, as I–V curves are measured well below coercive voltages. The obtained results suggest that the electrode/ferroelectric interface properties play a crucial role in the polarization-coupled resistive switching behavior in FTJ devices. Introduction of the NH_3 layer at the graphene/$BaTiO_3$ interface not only stabilizes the polarization of $BaTiO_3$ but also significantly enhances the TER effect.

6.5 Modeling of the Effect of the Polar Layer on Tunneling Electroresistance

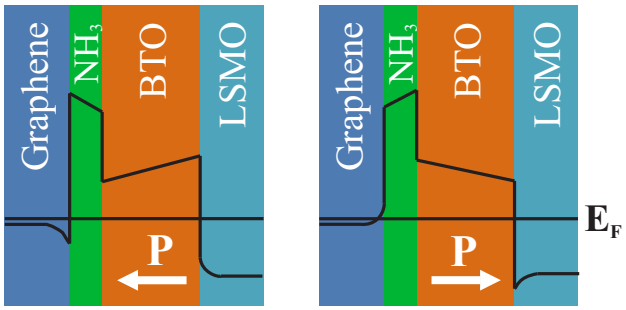

Figure 6.5: Schematic illustration of the energy barrier diagrams for the two polarization states in the graphene/NH_3/$BaTiO_3$/(La,Sr)MnO_3 tunnel junctions.

In the graphene/NH_3/$BaTiO_3$/(La,Sr)MnO_3 tunnel junctions, the NH_3 layer plays a role as an additional barrier. Figure 6.5 shows a schematic illustration of the energy barrier diagrams for polarization up (pointing to graphene) and polarization down (pointing to substrate) states, respectively. The polar molecular NH_3 layer acts as screening dipoles for screening the polarization charges in the $BaTiO_3$ layer, so that the dipoles of NH_3 are oriented opposite to the $BaTiO_3$ polarization. Upon polarization reversal, the dipoles of NH_3 also switch, as shown in Fig. 6.5, which effectively screen the polarization charges and thus stabilizes the polarization.

The effect of NH_3 layer on the TER effect is then calculated from the potential profile shown in Fig. 6.5 as a function of NH_3 barrier thickness and barrier height (Fig. 6.6). The tunneling conductance for ON and OFF states decreases when increasing the thickness of NH_3 layer (Fig. 6.6(a)). However, the resulting TER value (Fig. 6.6(b)) increases rapidly when increasing the NH_3 barrier thickness, resulting an enhancement of the TER effect over an order of magnitude when NH_3 thickness increases from 4 Å to 10 Å. On the other hand, the barrier height of NH_3 layer

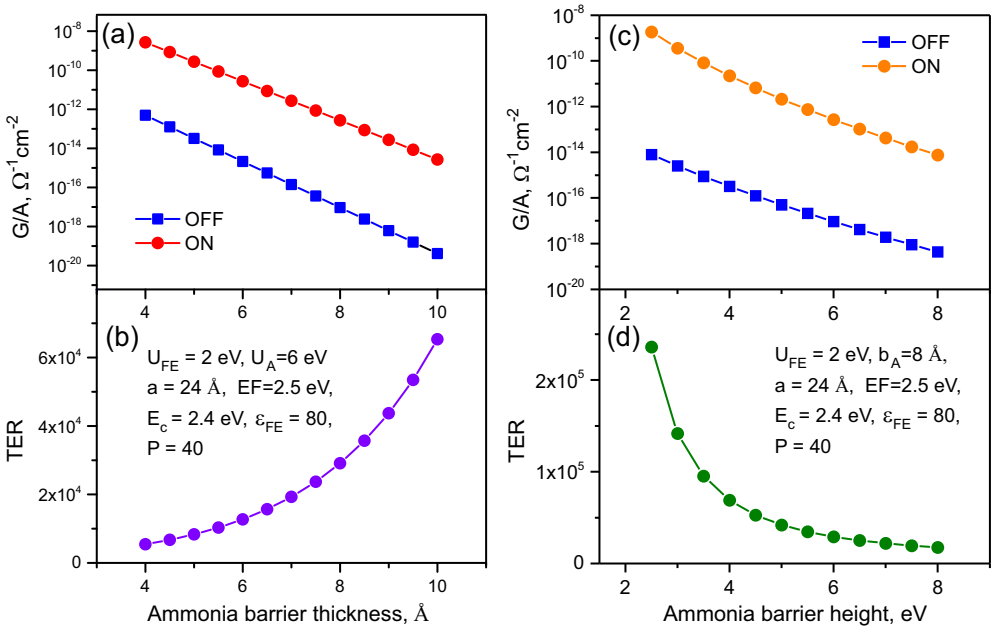

Figure 6.6: Modeling of the tunneling conductance and TER effect as a function of NH_3 barrier thickness and barrier height in graphene/NH_3/$BaTiO_3$/(La,Sr)MnO_3 tunnel junctions. (a) Tunneling conductance for ON and OFF states, and (b) TER effect as a function of NH_3 barrier thickness. (c) Tunneling conductance for ON and OFF states and (d) TER effect as a function of NH_3 barrier height.

also affects the tunneling conductance and the TER value. Figure 6.6(c) shows the tunneling conductance as a function of the NH_3 barrier height, which also shows a decreasing of conductance when increasing barrier height. However, an enhancement of the TER effect can be achieved by reducing of the barrier height.

6.6 Conclusion

In conclusion, we obtained stable and switchable polarization in graphene/$BaTiO_3$/(La,Sr)MnO_3 tunnel junctions by introducing a polar NH_3 layer at the graphene/$BaTiO_3$ interface for providing more efficient screening charges. In the meanwhile, this additional NH_3 layer significantly enhances the tunneling electroresistance effect of the tunnel junction, making it promising for device applications.

References

[1] E. Y. Tsymbal and H. Kohlstedt, Science **313**, 181 (2006).

[2] D. Pantel, H. Lu, S. Goetze, P. Werner, D. J. Kim, A. Gruverman, D. Hesse, and M. Alexe, Appl. Phys. Lett. **100**, 232902 (2012).

[3] D. J. Kim, H. Lu, S. Ryu, C.-W. Bark, C.-B. Eom, E. Y. Tsymbal, and A. Gruverman, Nano Lett. **12**, 5697 (2012).

[4] Z. Wen, C. Li, D. Wu, A. Li, and N. Ming, Nat. Mater. **12**, 617 (2013).

[5] Y. W. Yin, J. D. Burton, Y-M. Kim, A. Y. Borisevich, S. J. Pennycook, S. M. Yang, T. W. Noh, A. Gruverman, X. G. Li, E. Y. Tsymbal, and Q. Li, Nat. Mater. **12**, 397 (2013).

[6] K. J. Choi, M. Biegalski, Y. L. Li, A. Sharan, J. Schubert, R. Uecker, P. Reiche, Y. B. Chen, X. Q. Pan, V. Gopalan, L.-Q. Chen, D. G. Schlom, and C. B. Eom, Science **306**, 1005 (2004).

[7] A. Gruverman, D. Wu, H. Lu, Y. Wang, H. W. Jang, C. M. Folkman, M. Y. Zhuravlev, D. Felker, M. Rzchowski, C.-B. Eom, and E. Y. Tsymbal, Nano Lett. **9**, 3539 (2009).

Chapter 7

Mechanical Switching of Ferroelectric Polarization

7.1 Introduction to Flexoelectric Effect

One of the most distinctive features of ferroelectrics is a strong coupling between the polarization and mechanical strain that gives rise to a range of electromechanical phenomena in these materials including piezoelectric, electrostrictive and flexoelectric effects. Piezoelectricity is one of the most prominent and intensively studied effects, which is the linear electromechanical interaction between the electric field and mechanical stress in non-centrosymmetric crystals. An alternative effect which has received comparatively less attention is flexoelectricity—the coupling between electrical polarization and *strain gradient*: a strain gradient in a crystal generates an electrical polarization (direct flexoelectric effect), or a polarization gradient induces stress or strain in the crystal (converse flexoelectric effect). However, it is becoming no longer negligible, for several reasons [1]. First, flexoelectricity, in contrast to piezoelectricity, is a universal property allowed by symmetry in any structure, as

strain gradient breaks the inversion symmetry. Centrosymmetric materials cannot be piezoelectric, but can be flexoelectric, making flexoelectricity more general than piezoelectricity. Second, flexoelectricity grows as device size decreases. Strain gradient is inversely proportional to the relaxation length: A strain difference over a smaller distance gives a larger strain gradient, which gives rise to a huge flexoelectric effect at the nanoscale. Finally, flexoelectricity has polarity, while homogeneous stress/strain does not, so it can tune not just the magnitude but also the sign of the polar vector. The polar nature of the flexoelectric effect means that strain gradients can effectively play the role of an equivalent electric field and can be used in field effect devices, or to interplay with ferroelectric polarization in ferroelectrics.

Flexoelectricity was first theoretically predicted by Kogan in 1964 [2] and experimentally demonstrated by Bursian and Zaikovskii in 1968 [3], who measured the changes in curvature of a ferroelectric film due to polarization (converse flexoelectric effect). The same year, Scott [4] invoked a strain gradient as a parity-breaking mechanism in spectroscopic measurements. Further theoretical consideration of flexoelectricity has been provided by Tagantsev [5], and seminal experimental measurements of direct flexoelectricity for perovskite ferroelectrics are due to Cross and Ma [6, 7].

In the general case, a polarization can result from both piezoelectric and flexoelectric effects due to a mechanical stress. The total electrical polarization P can be described as [7]:

$$P_i = d_{ijk}\sigma_{jk} + \mu_{ijkl}\frac{\partial \varepsilon_{ij}}{\partial x_l}, \tag{7.1}$$

where d_{ijk}, σ_{jk}, μ_{ijkl}, ε_{ij} and x_l are the piezoelectric coefficient, applied stress, flexoelectric coefficient, strain and spatial coordinate, respectively. There are two terms in Eq. (7.1) that contribute to the polarization: a linear coupling to stress which is the piezoelectric effect, and a gradient coupling to stress/strain which is the flexoelectric

effect.

The flexoelectric coefficient μ_{ijkl} is a four rank tensor, and has the same symmetry as the electrostriction coefficient. For a cubic crystal the non-zero components are μ_{1111}, μ_{1122}, and μ_{1212}, or in a matrix notation, μ_{11}, μ_{12}, and μ_{44}, which are called longitudinal, transverse, and shear coefficient, respectively. For decades after its proposal in the early 1960s, there were only few studies of flexoelectricity, even though it is a general property in solids. The reason was the comparatively small magnitude of the flexoelectric coefficient. Theoretical predictions pointed out that the flexoelectric coefficient scales as $\mu \sim \chi(\frac{e}{a})$, where χ, e and a are the dielectric susceptibility, electron charge and the lattice constant, respectively [2, 5]. The flexoelectric coefficient is typically in the order of $e/a \sim 10^{-10}$ C/m for ordinary dielectric materials. Also, high strain gradient is difficult to achieve in solids, giving that flexoelectricity is generally weaker than piezoelectricity.

The static response of the flexoelectric effect can be phenomenologically described by Landau-Ginzburg-Devonshire (LGD) theory. The macroscopic description of the static bulk flexoelectric response can be obtained by generalizing the thermodynamic potential used for the description of the piezoelectric response by introducing a linear coupling between the polarization and strain gradient and vice versa into the system. The thermodynamic free energy density Φ_G for such a description reads [1]:

$$\Phi_G = \frac{1}{2\chi}P^2 + \frac{c}{2}\varepsilon^2 - \frac{\mu}{2\chi}(P\frac{\partial\varepsilon}{\partial x} - \varepsilon\frac{\partial P}{\partial x}) - PE - \varepsilon\sigma, \tag{7.2}$$

where c, σ, ε, and μ are the elastic constant, stress, strain, and the flexoelectric coefficient, respectively. For simplicity here we have dropped the tensor suffix. Also, the piezoelectric term $d\varepsilon P$ and the electrostrictive coupling term $q\varepsilon P^2$ have been dropped from the free energy density equation, where d and q are piezoelectric and

electrostrictive constants. Variational minimization of Φ_G against P and ε using Euler equations $\partial\Phi_G/\partial A - \frac{d}{dx}(\partial\Phi_G/\partial(\partial A/\partial x)) = 0$, ($A = P$ or ε) leads to [1]:

$$P = \chi E + \mu\frac{\partial\varepsilon}{\partial x}, \tag{7.3}$$

$$\sigma = c\varepsilon + \frac{\mu}{\chi}\frac{\partial P}{\partial x}. \tag{7.4}$$

In Eq. 7.3, the first right-hand-side term describes the dielectric response with the clamped dielectric susceptibility χ, and the second right-hand-side term describes the flexoelectric response with the flexoelectric coefficient μ. In Eq. 7.4, the first right-hand-side term describes Hook's law, with the elastic constant at fixed polarization c, and the second right-hand-side term describes the converse flexoelectric response. The polarization P in Eq. 7.4 can be simply replaced by χE by taking into account that the flexoelectric effect is relatively weak, which describes the strain generated by a non-uniform polarization or electric field.

As is clear from Eq. 7.3, the vector $\frac{\mu}{\chi}\frac{\partial\varepsilon}{\partial x}$ has the same effect on polarization as the external electric field E, which suggests that strain gradient is equivalent to an external electric field, and is sometimes termed as the flexoelectric field.

In this chapter, we demonstrate that the stress gradient generated by the AFM tip can be used to mechanically switch the polarization in the nanoscale volume of a ferroelectric film. Pure mechanical force can therefore be used as a dynamic tool for polarization control, enabling information processing in a new concept of multiferroic high-density data storage devices where the memory bits are written mechanically and read electrically [8, 9].

Results described in Section 7.2.1 have been published in ref. [8].

7.2 Flexoelectric Effect in Ferroelectrics: Mechanical Switching of Polarization

7.2.1 Mechanical switching of polarization in $BaTiO_3$ films

Previous studies of the tip-induced stress effect showed suppression of the piezoelectric response under a sufficiently high loading force [10, 11] with almost complete recovery after stress release. Polarization vector rotation caused by simultaneous application of an external electrical bias and tip-induced stress has been observed in polycrystalline thin films [11, 12], although in these studies the random orientation of the polarization in the crystals allowed for partial ferroelastic rotation rather than pure 180° inversion of polarization. On the other hand, recent report by Lee et al. [13] showed that the flexoelectric effect caused by strain gradients can create a strong imprint in uniaxial, perfectly oriented ferroelectric thin films, and flexoelectricity due to substrate bending was also invoked in the imprint of polarization in polycrystalline ferroelectric films [14]. This suggests that strain gradients, rather than homogeneous strain, can be exploited for switching polarization and "writing" the domain bits into ferroelectric memories. This process is allowed by symmetry because a strain gradient, unlike a homogeneous strain, is an odd parity tensor without inversion symmetry—strain gradients have directionality and polarity [2, 4]. Although flexoelectricity is generally weaker than piezoelectricity, gradients grow in inverse proportion to the relaxation length, so very large flexoelectric effects can be achieved at the nanoscale [15, 16, 17].

We have explored whether flexoelectricity can actively switch ferroelectric polarization by mechanically pushing AFM tips onto the surface of epitaxial single-crystalline $BaTiO_3$ films, thereby inducing large and localized stresses. The films were fabricated by atomic layer controlled growth on atomically smooth (001)-$SrTiO_3$

substrates with $La_{0.67}Sr_{0.33}MnO_3$ conductive buffers that served as bottom electrodes [18, 19]. Compressive stress induced by the substrate ensured that polarization was aligned in the direction perpendicular to the surface, and only 180° inversion of polarization would be allowed. $BaTiO_3$ films with a thickness of 12 unit cells, or ~4.8 nm, have been chosen so as to ensure epitaxial clamping and prevent mismatch strain relaxation.

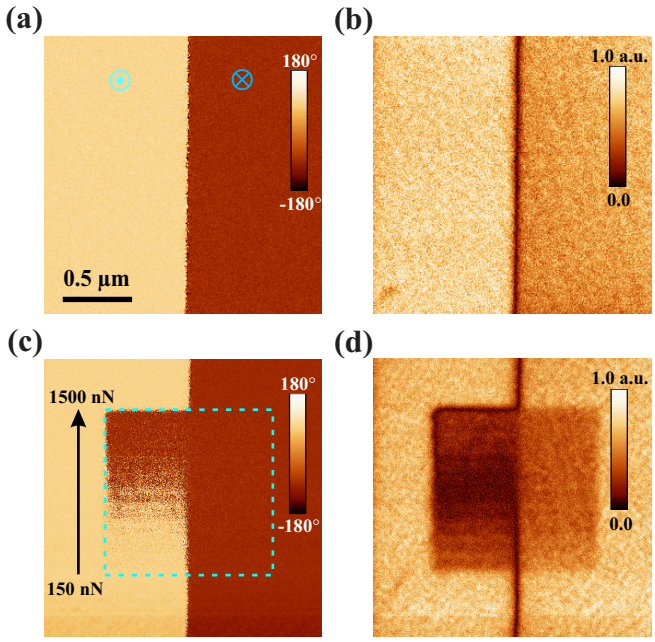

Figure 7.1: Mechanically induced reversal of ferroelectric polarization. (a, b) PFM phase (a) and amplitude (b) images of the bidomain pattern electrically written in the $BaTiO_3$ film. (c, d) PFM phase (c) and amplitude (d) images of the same area after the 1×1-μm^2 area in the center (denoted by a dashed-line frame) has been scanned with the tip under an incrementally increasing loading force. The loading force was increasing in the bottom-up direction [denoted by a black arrow in (c)] from 150 to 1500 nN.

Initial testing of the films by means of PFM show that as-grown $BaTiO_3$ films are in a single-domain state with out-of-plane polarization, indicating effective screening of the depolarizing field by surface adsorbates [20]. Bipolar domain patterns can be generated conventionally with an electrically biased PFM tip: the film surface

is scanned with a tip under ±4-V bias exceeding the coercive voltage. The 2×2-μm^2 PFM images of this electrically written domain structure are shown in Fig. 7.1, (a) and (b), with left half polarized up and right half polarized down. A typical value of the contact force during conventional PFM imaging is ~30 nN. A stable and uniform PFM amplitude signal across the domain boundary illustrates effective electric switchability of the film and strong polarization retention.

The mechanical switching has been investigated by scanning a 1×1-μm^2 area of the bipolar domain pattern with the electrically grounded tip under an incrementally increasing loading force from 150 to 1500 nN, with a corresponding change in the applied stress from 0.5 to 5 GPa (approximating the tip-surface contact area as a disk of 10 nm in radius). Note that, although the maximum local stress is very large, it is still well below the threshold (~20 GPa) for irreversible plastic deformation damage of the $BaTiO_3$ surface [21]. After that, a larger area of 2×2 μm^2 is imaged by conventional PFM with a low load of 30 nN (Fig. 7.1, (c) and (d)).

The tip-induced stress reverses the PFM phase contrast in the left half of the image where initially polarized up in Fig. 7.1(c), from bright to dark, indicating inversion of the polarization from up to down, while no change in the right half of the image where initially polarized down. Figure 7.1(d) shows a non-monotonous change in the corresponding PFM amplitude image of the flexoelectrically switched domain in the left side: Initially, the amplitude decreases as load increases and then, at an applied force of ~750 nN, it increases again. Due to the fact that only compressive stress may be applied in the context of this experiment, the resulting flexoelectric field generated by the AFM tip pressing is pointing to downward direction, which only switches polarization from up to down.

This type of behavior is analogous to the polarization-reversal process in conventional (voltage-induced) PFM, in which the electromechanical amplitude signal passes

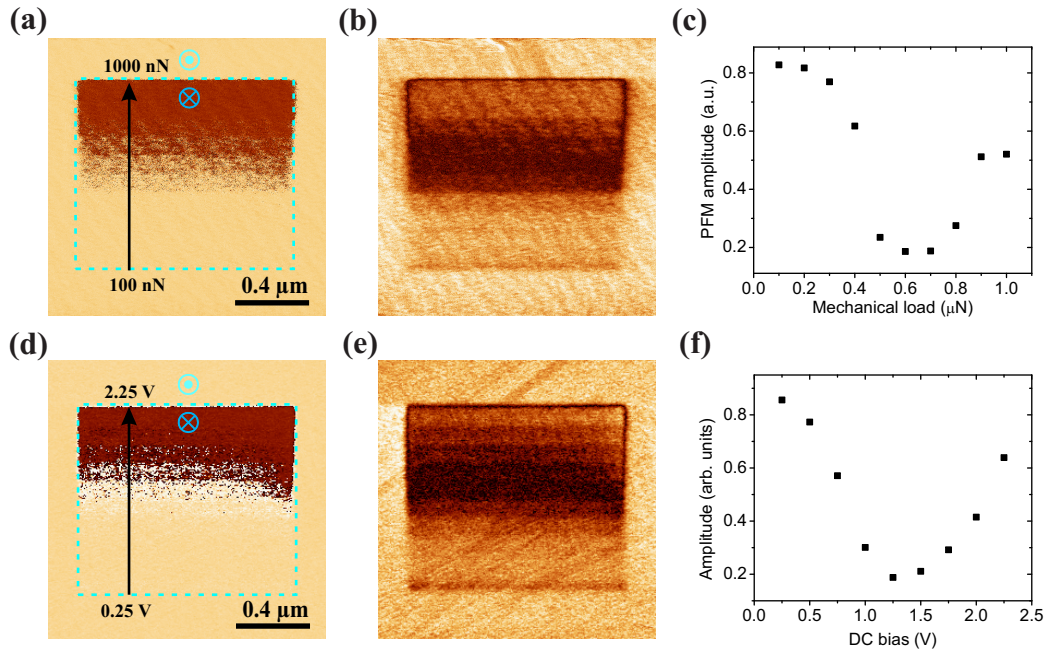

Figure 7.2: Comparison of mechanically-induced and electrically-induced reversal of ferroelectric polarization in the $BaTiO_3$ film. (a, b) PFM phase (a) and amplitude (b) images of the film acquired after the central area has been scanned with the tip under an incrementally increasing in mechanical load from 100 nN to 1000 nN. (c) PFM amplitude as a function of mechanical load obtained by cross-section analysis of the mechanically scanned area in (b). (d, e) PFM phase (d) and amplitude (e) images acquired after the central area has been scanned with the tip under an incrementally increasing in dc bias from 0.25 V to 2.25 V. (f) PFM amplitude as a function of a dc bias obtained by cross-section analysis of the poled area in (e).

through a minimum during switching. Figure 7.2 gives a comparison of mechanically-induced and electrically-induced reversal of ferroelectric polarization in the $BaTiO_3$ film, where an area in the center has been scanned with a tip either under an incrementally increasing mechanical load or under an incrementally increasing electrical dc bias on upward polarized background before PFM imaging. The polarization patterns generated by mechanical load (Fig. 7.2, (a) and (b)) and by electrical field (Fig. 7.2, (d) and (e)) are identical. For both cases, initially the PFM amplitude signals decrease and then, after reaching a minimum value, they start to increase (Fig. 7.2, (c) and (f)). This is caused by the formation of 180° domains (antiparallel polarization)

so that the net polarization and associated piezoelectric signal go through zero when the volume fractions of domains with opposite polarization become equal. Beyond that, the PFM amplitude grows again while the PFM phase is changed by 180°, indicating that the polarization has been inverted. The results show that there is no fundamental difference in the switching response induced by conventional electric biasing and that induced by mechanical loading, indicating that flexoelectricity is an effective substitute for voltage in ferroelectric switching.

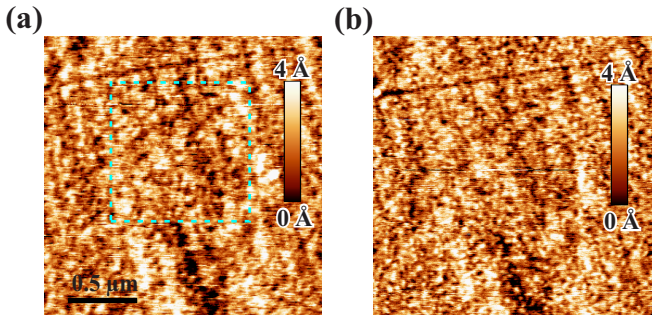

Figure 7.3: (a and b) Topographic images acquired before (a) and after (b) mechanical writing of 1500 nN in the center 1×1 μm^2 squire showing that the film surface was not affected by the writing process.

There are several useful features of mechanical switching: (i) It generates stable domain patterns exhibiting no relaxation for days after switching, (ii) no damage to the sample surface caused by a high loading force was observed, (iii) mechanically written domain patterns are electrically erasable, and (iv) the mechanically written domains are nanoscopic. These features are illustrated in Fig. 7.3 and Fig. 7.4.

The topographic images acquired before (Fig. 7.3(a)) and after (Fig. 7.3(b)) mechanical writing of 1500 nN in the center 1×1 μm^2 squire showing that the film surface does not exhibit any traces of surface deformation by the writing process. Mechanically written parallel linear domains, shown in Fig. 7.4(a), have been subsequently transformed into the pattern in Fig. 7.4(b) by electrically erasing central domain seg-

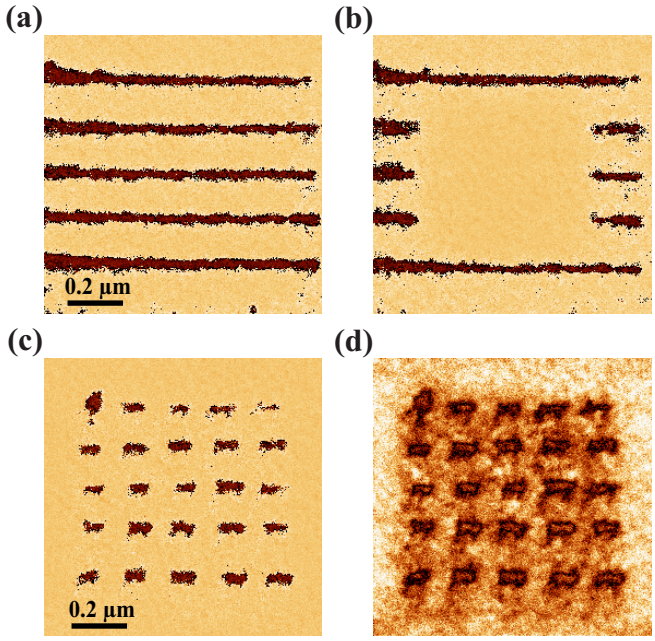

Figure 7.4: Fabrication of nanoscale domain patterns by mechanical means. (a) Domain lines mechanically written in the $BaTiO_3$ film by scanning the film with a tip under a loading force of 1500 nN. (b) The same domain structure modified by electrical erasure of the mechanically written domains. Erasure has been performed by scanning the central segment with the tip under a dc −3-V bias. (c, d) PFM phase (c) and amplitude (d) images of an array of flexoelectrically written dot domains illustrating the possibility of using mechanical writing for high density data-storage application.

ments with a tip under a dc −3-V bias. Finally, Fig. 7.4, (c) and (d) shows an array of dot domains only 30 nm in size, written by abruptly alternating the tip load between 30 and 1500 nN during scanning.

Mechanical polarization switching is also feasible by mechanical scanning using an insulating tip, as no voltage is required for polarization switching. The tip generated internal flexoelectric field causes a potential drop through the ferroelectric film and this internal field switches the polarization when it is higher than coercive field in the film. Figure 7.5 shows an example of domain pattern generated by mechanical writing using a non-conductive Si tip and visualized in a conventional PFM mode

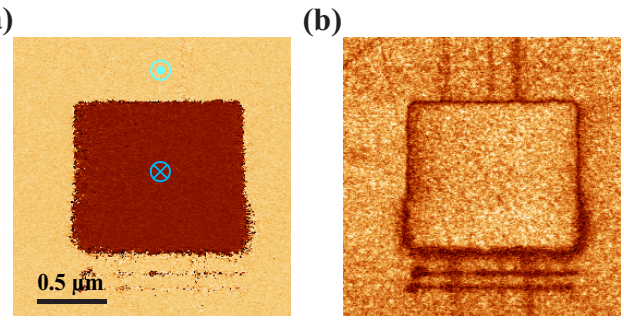

Figure 7.5: PFM phase (a) and amplitude (b) images of the domain pattern generated by mechanical writing in the center squire using a non-conductive Si tip under a 1400 nN load and visualized in a conventional PFM mode using a PtIr-coated Si tip. Initial background polarized upward.

using a conductive tip.

These results open up a way to write ferroelectric memory bits using mechanical force instead of electrical bias in data-storage devices. By converting mechanical stress into readable information, such devices would operate as a nanoscopic analog of typewriters that could be scaled up using a millipede-like scheme [22]. The tip-sample contact area is typically less than 10-nm in radius, so switching can be highly localized, allowing fabrication of high-density domain patterns. Because no voltage is applied during mechanical switching, leakage and/or dielectric breakdown problems are minimized. Because electrodes are not required, the problems caused by their finite screening length [23] are also removed.

Conversely, if top electrodes were used, mechanical writing would enable the targeted poling of localized areas under the electrodes—which is impossible using voltage, as the electric field is homogeneous in a parallel-plate capacitor. This suggests the possibility of controlled fabrication of domain walls underneath top electrodes, useful for electronic device applications employing physical properties of domain walls [24] that could be read in a nondestructive manner by PFM imaging [25] or by measuring the electroresistive effect [26]. These results will be discussed in Section 7.3 by using

graphene as top electrode.

7.2.2 Universality of flexoelectric control of polarization

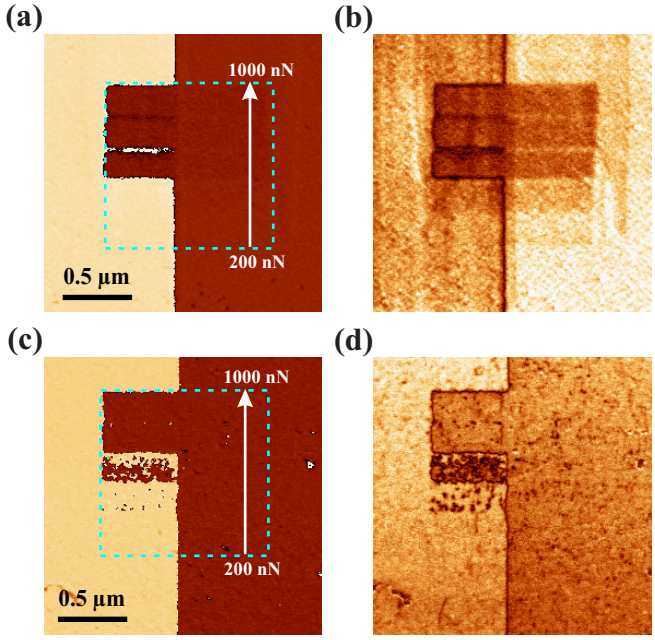

Figure 7.6: (a, b) PFM phase (a) and amplitude (b) images of the domain pattern generated by mechanical writing in the center squire area on a bi-poled domain area on $Pb(ZrTi)O_3$(4nm)/$(LaSr)CoO_3$/$SrTiO_3$. (c, d) PFM phase (c) and amplitude (d) images of the domain pattern generated by mechanical writing on $BiFeO_3$(12.5nm)/$SrRuO_3$/$SrTiO_3$. In both cases mechanical load increased from 200 nN to 1000 nN from bottom to top.

Mechanical switching of ferroelectric polarization via flexoelectric coupling is a general phenomenon that exists in all ferroelectrics due to the universality of the flexoelectric effect. Figure 7.6 shows examples of domain pattern generated by mechanical writing using the same approach as in the previous section, on a 4-nm-thick $Pb(Zr,Ti)O_3$ film (Fig. 7.6, (a) and (b)) and on a 12.5-nm-thick $BiFeO_3$ film (Fig. 7.6, (c) and (d)). In both cases, mechanical writing switches polarization from upward to downward when mechanical load is higher than a certain threshold load. In our AFM

tip experimental set-up, we have an *effective* flexoelectric coefficient that contains contributions from all the tensor components. In all the perovskites that have been tested, mechanical writing always switches polarization from upward to downward, suggesting a downward flexoelectric field when pressing the AFM tip, which gives a positive effective flexoelectric coefficient. This is actually consistent with experimental measurements of the flexoelectric effect: In all the perovskites ever measured experimentally, the *effective* transverse flexoelectric coefficient always turns out to be positive [27, 28].

Next sections consider the effect of various parameters on the threshold load, which allows quantification of the flexoelectric effect.

7.2.3 Quantification of flexoelectric switching: Effect of tip radius

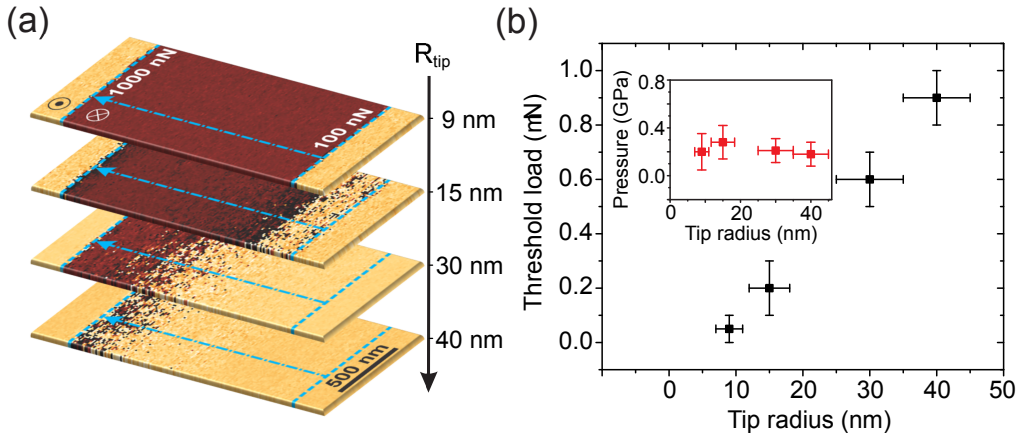

Figure 7.7: (a) A series of PFM phase images on 12 u.c. $BaTiO_3$ film after mechanical writing in the center dashed area using different type of tips with radius around 9 nm, 15 nm, 30 nm and 40 nm respectively. Mechanical load increased from 100 nN to 1000 nN in the arrow direction. (b) Threshold switching load as a function of tip radius obtained from (a). The threshold load increases as tip radius increases. The inset calculates the threshold pressure assuming a tip-sample contact radius same as tip radius. Threshold pressure maintains a constant as tip radius varies.

The threshold load—a minimal mechanical load which is required to flexoelectrically switch the polarization—depends on material constants of the ferroelectric films, such as elastic constants, flexoelectric coefficients, coercive fields, etc., and also external parameters, such as tip radius, electrical bias, temperature, etc. The AFM tip radius is especially important as the typical AFM tip radius is only tens of nanometers, so that a small change of tip radius would largely affect the stress gradient and the flexoelectric effect magnitude. Here, we used different types of fresh AFM tips with variable tip radii to determine the threshold load for the 12 u.c. $BaTiO_3$ film. Figure 7.7(a) shows a series of PFM images after mechanical writing with different radius AFM tips. The mechanical stress induces polarization switching (bright to dark) at different threshold loads with different tip radius: less than 100 nN for tip radius of 9 nm and about 1000 nN for tip radius of 40 nm. The resulting threshold load as a function of tip radius is shown in Fig. 7.7(b): There is a strong dependence of the threshold load on the tip radius: a smaller radius tip requires much lower mechanical load for flexoelectric switching. However, the inset plot shows that the threshold pressure keeps almost the same for all tip radii, since stress is proportional to pressure. This is an important issue as there is always wears of the tip apex after some heavy scanning, so that it increases the tip radius and consequently reduces the flexoelectric effect.

7.2.4 Quantification of flexoelectric switching: Effect of film thickness

The flexoelectric field generated by the AFM tip is non-uniform, i.e. it is large only within the first several nanometers from the tip-sample contact and rapidly decreases with distance. Thus, there should be a strong thickness dependence of the flexoelectric

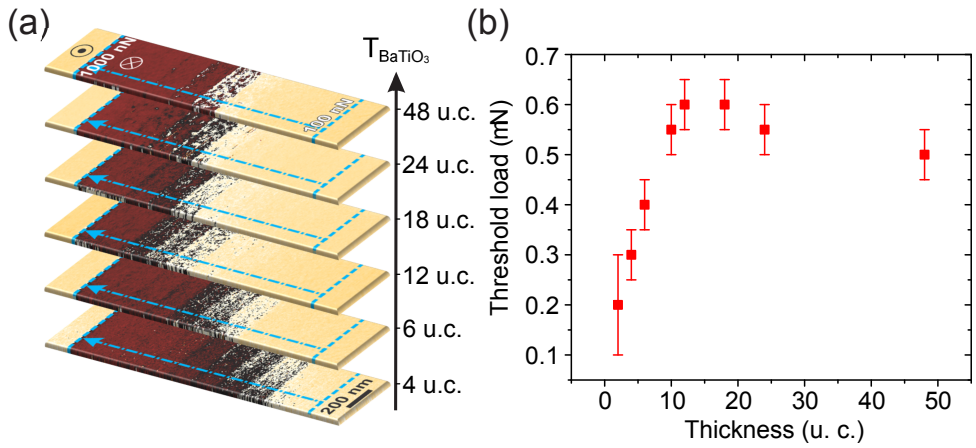

Figure 7.8: (a) A series of PFM phase images after mechanical writing in the dashed area for $BaTiO_3$ film thicknesses from 4 u.c. to 48 u.c respectively. Mechanical load increased from 100 nN to 1000 nN (in the direction marked by the blue arrow). (b) Threshold mechanical load as a function of $BaTiO_3$ thickness. Threshold load increases with film thickness up to 12 u.c., and then becomes relatively flat.

polarization switching behavior. Here, we examined the threshold load in the $BaTiO_3$ films with the thicknesses ranging from 4 u.c. to 48 u.c. Figure 7.8(a) shows a series of PFM images after mechanically-induced switching (marked by the dashed lines) in the $BaTiO_3$ film with different thickness. Figure 7.8(b) shows that the threshold load increases with thickness up until 12 u.c., and then stays relatively flat. Analysis of this data certainly requires information on the coercive field for all film thicknesses.

7.2.5 Flexoelectric field in static and dynamic regimes

It is possible to consider two different cases for the flexoelectric effect induced by the AFM tip: a static case, when the tip under a high load is fixed at a certain point, and a dynamic case, when the tip is in sliding motion (scans the surface). Tip sliding motion introduces additional friction force along the tip moving direction, which not only introduces assymetric strain distribution, but also significantly contributes to the shear strain gradients. Here, we present a study on calibration of mechanical load

generated flexoelectric field in the 12 u.c. $BaTiO_3$ film, both in static regime by local PFM hysteresis measurements under static mechanical load, or in dynamic regime by examining the switching behavior after mechanical writing.

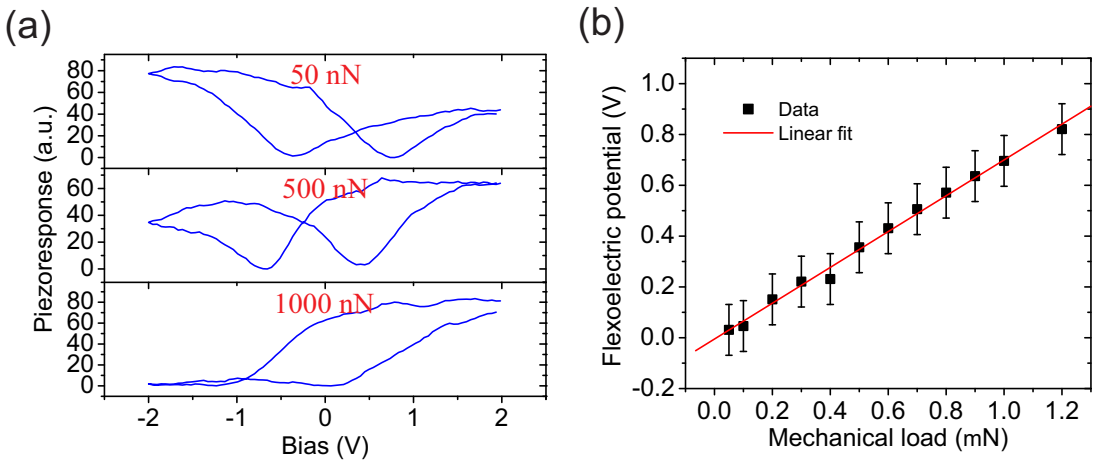

Figure 7.9: (a) a series of local PFM hysteresis loops obtained on $BaTiO_3$ under tip load of 50 nN, 500 nN and 1000 nN from top to bottom. Local switching coercive voltage is defined at the minimum of the PFM hysteresis loop. (b) Flexoelectric potential as a function of tip load in the static regime obtained from (a).

PFM local switching spectroscopy is a static measurement at a fixed point, which shows a hysteretic piezoresponse as a function of the applying dc switching bias due to the reversible ferroelectric polarization. Figure 7.9(a) shows a series of bias-off local PFM hysteresis loops obtained on the $BaTiO_3$ film under different mechanical loads, 50 nN, 500 nN, and 1000 nN from top to bottom. There is a clear negative shift of the coercive voltages when increasing the mechanical load, due to the flexoelectric field generated by the tip pressing. The average of coercive voltages contains information of the flexoelectric potential (details about flexoelectric potential will be discussed in Section 7.4):

$$(V_c^+ + V_c^-)/2 = V_{imp} - V_{flexo}, \tag{7.5}$$

where V_c^+, V_c^-, V_{imp} and V_{flexo} are the positive and negative coercive voltages, the ini-

tial imprinted voltage, and the flexoelectric potential, respectively. Strictly speaking, the piezoelectric effect may also contribute to the shift of coercive voltages. However, piezoelectricity acts equally on both polarization directions so that the average of coercive voltages cancels this effect and gives a good estimation of the flexoelectric potential. The flexoelectric potential, obtained from the PFM hysteresis loops, is shown in Fig. 7.9 as a function of the mechanical load. It gives a quite linear relationship between the flexoelectric potential and the mechanical load, with a slop of $V_{\text{flexo}}/F_{\text{load}} \sim 0.7$ V/μN, where F_{load} is the normal load applied to the tip. This means that for 1 μN of normal force applied to the tip, it generates about 0.7 V (1.4 MV/cm) across the $BaTiO_3$ film due to the flexoelectric effect, which is a huge electric field comparable to the coercive field of the film.

In the dynamic regime, the mechanical polarization switching is realized by scanning the AFM tip under high mechanical loads. During the mechanical writing process, an external dc voltage is applied. The critical polarization switching condition reads:

$$V_{\text{flexo}} + V_{\text{ext}} = V_{\text{c}}. \tag{7.6}$$

where V_{ext} is external voltage applied to the AFM tip. By measuring the threshold load F_{th} as a function of the external voltage V_{ext}, we can establish a relationship between the applied load F and the generated flexoelectric voltage V_{flexo}.

Figure 7.10(a) shows a set of PFM images after mechanical writing. Before PFM imaging, an upward polarization was initialized electrically, and then mechanical writing was performed in the center dashed area with an incremental load from 100 nN to 1000 nN in the arrow direction. During mechanical writing, a constant dc bias V_{ext} from −0.4 V to 1.2 V was maintained on the conductive tip. By determining the threshold load F_{th} for critical switching, we can estimate the flexoelectric potential

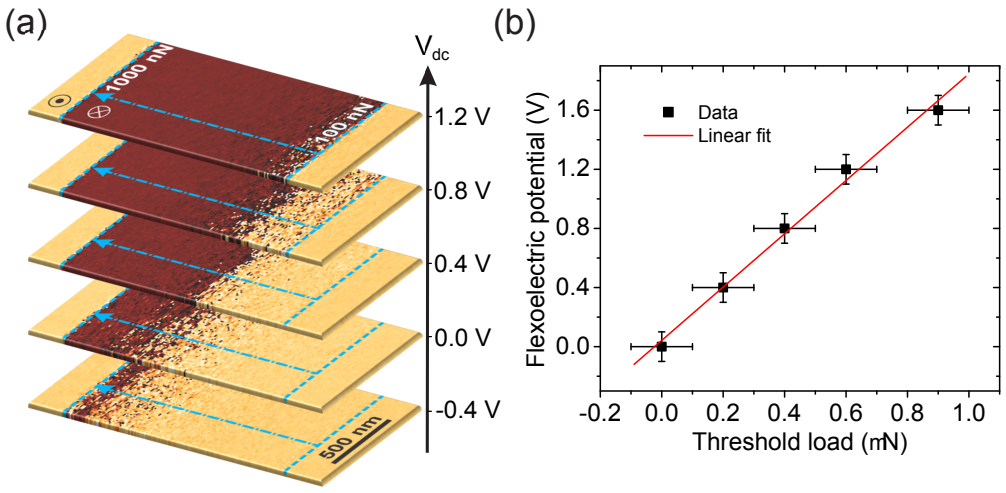

Figure 7.10: (a) A series of PFM images after mechanical writing in the center dashed area on $BaTiO_3$ with a constant tip voltage V_{dc} from -0.4 V to 1.2 V respectively. Mechanical load increased from 100 nN to 1000 nN in the arrow direction. Positive dc bias assists polarization switching, and reduces the threshold load. (b) Flexoelectric potential as a function of tip load in the dynamic regime obtained from (a).

from Eq. 7.6. Figure 7.10(b) shows the relationship between the flexoelectric potential and the mechanical load, which gives a slop of $V_{\text{flexo}}/F_{\text{load}} \sim 1.8$ V/μN. Comparing with the static case with the slop of only 0.7 V/μN, dynamic sliding motion of the tip significantly enhances the flexoelectric effect.

7.2.6 Scaling of the flexoelectric switching

Flexoelectric polarization switching is spatially more localized than electrical polarization switching, since the mechanical stress is concentrated at the tip-sample contact point, while the electric field spreads at the distances of hundreds of nanometers from the contact point. Figure 7.11 shows a direct comparison of electrically written and mechanically written lines on the 12 u.c. $BaTiO_3$ film. The electric bias of 2.7 V and mechanical load of 1500 nN used in the writing is calibrated to be equivalent in switching from Fig. 7.10. It is clear that the mechanically written lines are more

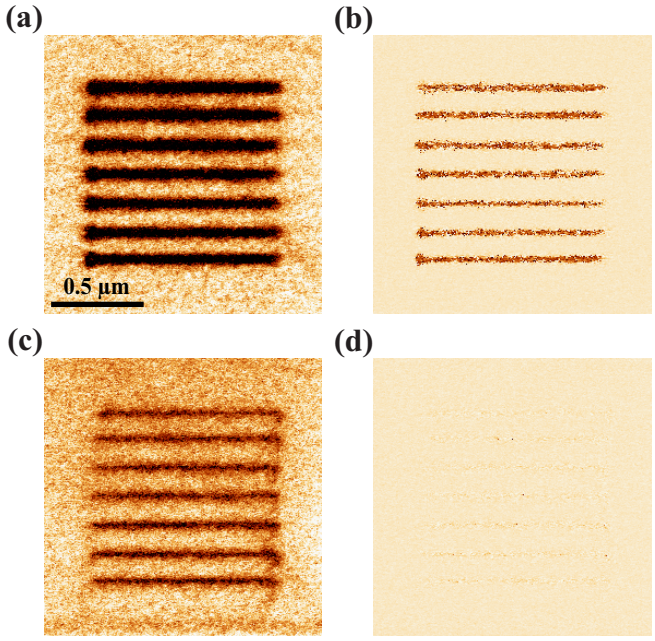

Figure 7.11: PFM images of electrically written lines at 2.7 V of (a) PFM amplitude and (b) PFM phase, and mechanically written lines at 1500 nN of (c) PFM amplitude and (d) PFM phase.

localized with domain sizes beyond resolution limit of typical PFM imaging (about 10 nm).

We tried to determine the rate of mechanically-induced switching by varying the time of load application to a single point. This was realized by scanning the sample surface with different speeds while applying a fixed loading force. Figures 7.12(a, b) show the resulting domain lines written mechanically at different tip scanning rates. At the fastest scanning rate of 20 µm/s, the tip dwelling time for each pixel (~4 nm in size) is about 0.2 ms. Given that switching still takes place at this scanning rate, it means that switching time due to flexoelectric effect at 1000 nN should be faster than 0.2 ms, which is an upper limit for for our experimental setup (the scanner in our AFM has the largest scan rate of 20 µm/s).

The size of mechanically written domain is very sensitive not only to the duration

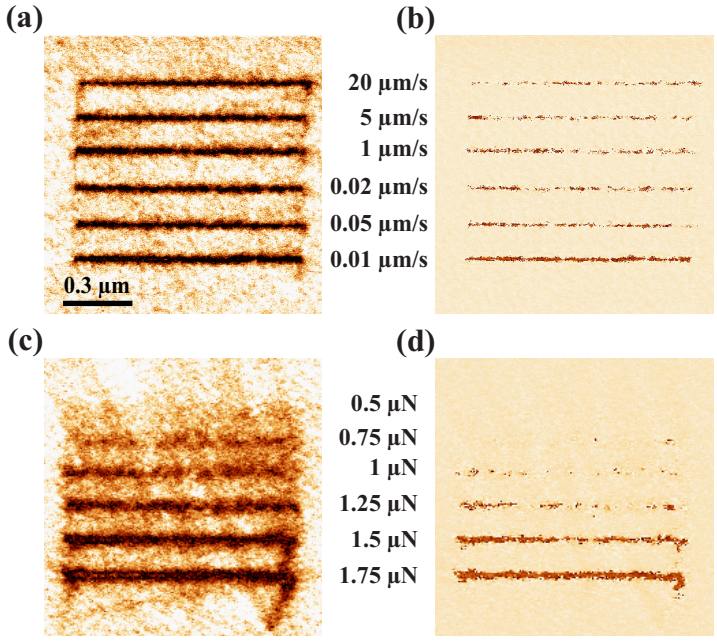

Figure 7.12: PFM images showing mechanically written lines on 48 unit cell $BaTiO_3$ film. (a, b) PFM amplitude (a) and phase (b) images of lines written at 1000 nN with writing rate from 20 µm/s down to 0.01 µm/s from top to bottom, respectively. (c, d) PFM amplitude (c) and phase (d) images of lines written at 1 µm/s with mechanical load from 0.5 µN to 1.75 µN from top to bottom, respectively.

of loading force application, but also to the applied force magnitude. Figure 7.12(c, d) show domain lines written with different mechanical load at the same scanning rate. Increase in the applied load results in wider domain lines which is due to the wider film region under high mechanical stress where it exceeded the threshold load.

7.3 Deterministic Domain Writing in Ultrathin Ferroelectric Capacitors

7.3.1 Introduction

In ferroelectric capacitors, application of a voltage potential to the electrodes results in polarization reversal in the whole volume of the ferroelectric film between the electrodes. Local control of polarization switching is thus impossible. Here, we show that using localized mechanical stress generated by the AFM tip it is possible to realize a deterministic switching of polarization underneath the top electrode due to the flexoelectric effect. This opens a possibility of precise control of polarization in ferroelectric capacitors and fine tuning of polarization-coupled effects, such as TER.

To realize local polarization switching in ferroelectric capacitors, several issues have to be addressed. First, the strain gradient generated by the AFM tip is large only within the first several nanometers, thus the top electrode should be thin enough (ideally, below 5 nm, to preserve the electrode material conductivity). Second, only in the relatively thin ferroelectric films (typically, <100 nm) a sufficiently high strain gradient (sufficient for polarization switching) can be realized. Third, the electrode should be durable and not damage under high mechanical stress. From these considerations, epitaxial oxide electrodes seem to be ideal for tip-induced flexoelectric switching. However, recent experimental studies showed that polarization screening by metal oxide electrodes is less effective than predicted, resulting in progressive loss of the net polarization in ultrathin ferroelectric capacitors [29, 23]. Typical metal electrodes should be at least 10 nm thick to ensure good conductivity. Also metal electrodes are not hard enough for high mechanical stresses. For this reason, in our studies, we decided to use graphene as a top electrode on $BaTiO_3$ films capacitors to

investigate local mechanically-induced polarization switching.

Graphene consists of a single planar sheet of carbon atoms, which allows the force gradient to be generated in the ferroelectric film underneath. Another advantage is that graphene is one of the toughest materials ever tested [30]. Also, graphene has a high carrier mobility and good electrical conductivity, making it an excellent material for electrodes. In this section we show that targeted switching of polarization in any selected localized area can be realized by mechanical writing with an AFM tip in the ferroelectric capacitors with graphene as a top electrode.

7.3.2 Electrical switching of polarization in graphene/$BaTiO_3$/(La,Sr)MnO_3 heterostructures

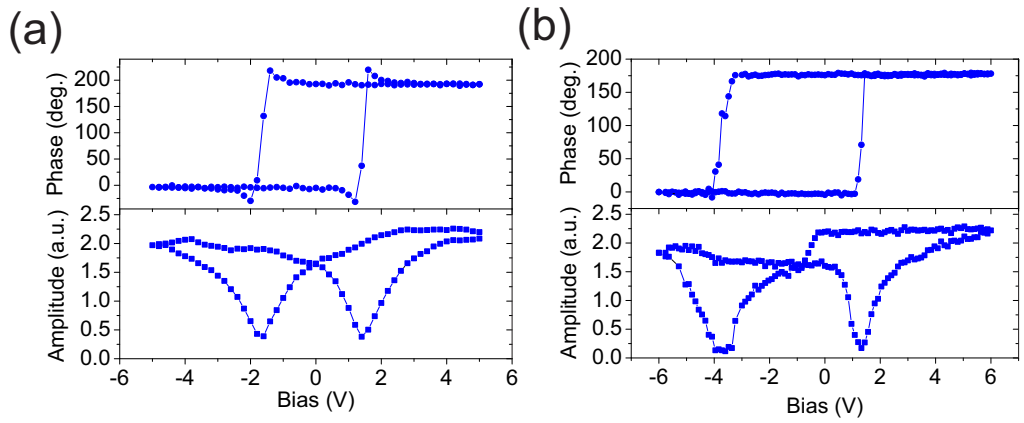

Figure 7.13: PFM switching hysteresis loops measured (a) on bare $BaTiO_3$ surface and (b) through graphene. Both cases show typical ferroelectric polarization switching hysteresis.

Here we used exfoliated graphene prepared by conventional scotch tape method in ambient condition [30]. To ensure polarization stability we have chosen epitaxial 48 u.c. $BaTiO_3$ films as the ferroelectric layer. Polarization switching in the graphene/$BaTiO_3$/(La,Sr)MnO_3/$SrTiO_3$ heterostructure is confirmed by PFM imag-

ing and switching spectroscopy. Figure 7.13 shows two PFM switching hysteresis loops obtained (a) on bare $BaTiO_3$ surface, and (b) through graphene. In both cases, the PFM switching loops exhibit a typical for ferroelectrics hysteresis behavior, confirming a reliable polarization switchability. The only difference is the increase in the negative coercive voltage. This may result from large leakage current due to low resistivity associated with one of the polarization states, which therefore requires a larger applied voltage for switching.

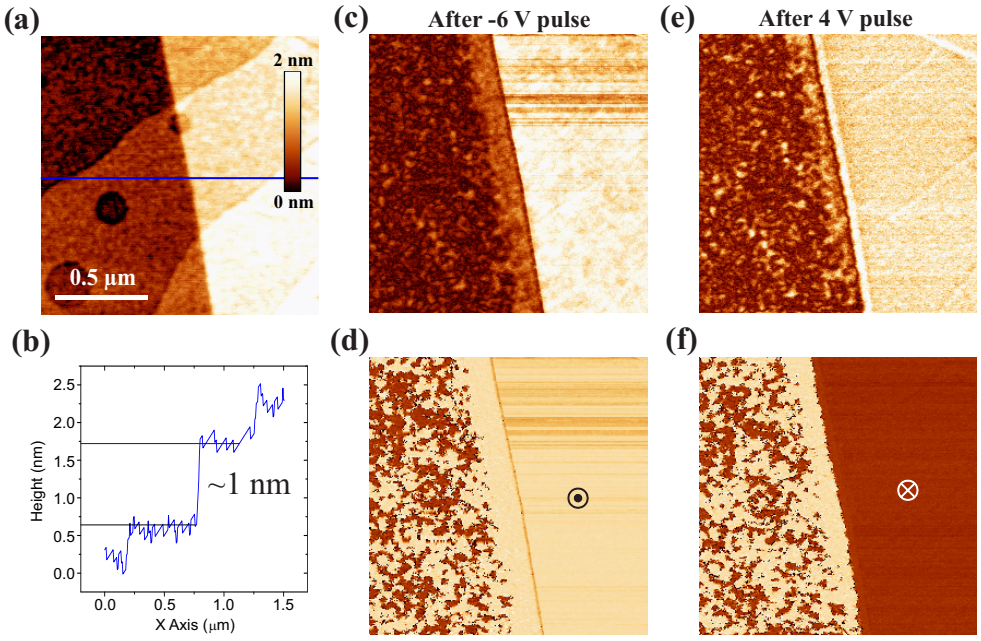

Figure 7.14: (a) Surface topography on the edge of the graphene flake. Left half of the images is exposed $BaTiO_3$ surface and right half covered by graphene. (b) A cross section from (a) along the blue line showing that the thickness of the graphene flake is around 1 nm. (c, d) PFM amplitude (c) and phase (d) images after application of a -6 V pulse on the graphene flake. (d, e) PFM amplitude (d) and phase (e) images after application of a $+4$ V pulse on the graphene flake.

PFM imaging also shows a stable polarization after application of voltage pulses to the graphene electrode. Figure 7.14(a) shows surface topography that includes the graphene flake (on the right) and exposed $BaTiO_3$ surface (on the left). From Fig. 7.14(b), it was determined that the thickness of the graphene flake was about

1 nm. PFM images after application of voltage pulses to the graphene electrode shown in Figs. 7.14(c)-(f) illustrate an efficient polarization control in the $BaTiO_3$ film underneath.

Electrical switching of polarization underneath the graphene flake is uniform. By application of a voltage pulse to graphene, homogeneous domain nucleation is observed across the whole graphene flake covered area. Figure 7.15 shows a series of

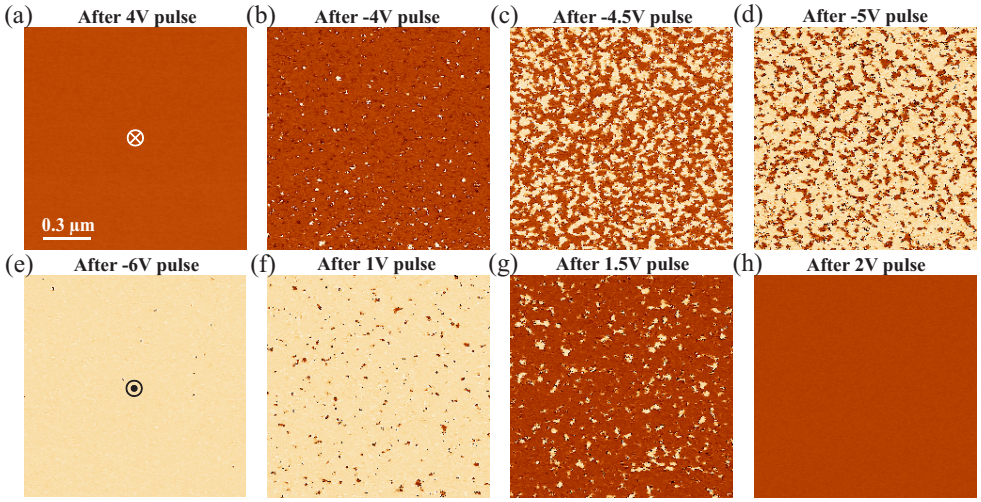

Figure 7.15: PFM images of the electrical switching of polarization underneath the graphene flake after application of voltage pulses.

PFM images taken through the graphene flake after application of voltage pulses with different amplitude and the same duration of 1 s. Fully switched polarization states as well as random domain nucleation sites can be seen. In all cases, the polarization patterns are stable within the investigated time of a few hours.

7.3.3 Deterministic domain writing through graphene

Mechanical switching of ferroelectric polarization through graphene has been done by scanning an AFM tip under a high mechanical load on graphene/$BaTiO_3$/(La,Sr)MnO_3 heterostructure. This approach allows switching of polarization only from up to down

directions, since only compressive stress can be applied by an AFM tip. Before mechanical writing, a −6 V voltage pulse is applied to graphene to set the initial polarization state to be upward. Mechanical writing has been performed by scanning a grounded AFM tip in a 0.5×0.5 μm^2 area under a mechanical load of 1600 nN. After

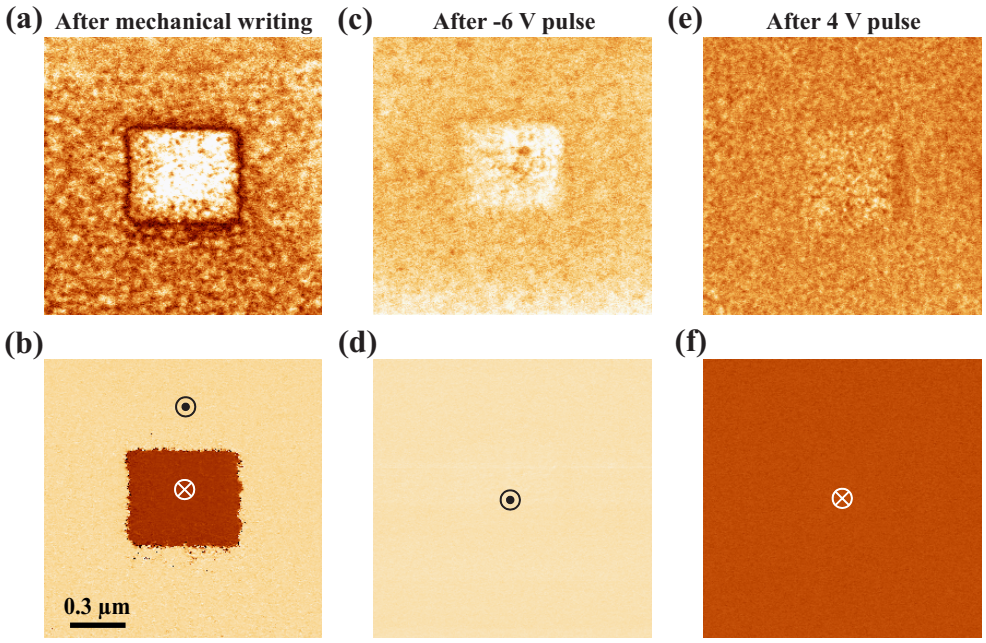

Figure 7.16: (a,b) PFM amplitude (a) and phase (b) after 1600 nN of mechanical writing in the center square. (c, d) PFM amplitude (c) and phase (d) images after application of a −6 V pulse. (e, f) PFM amplitude (e) and phase (f) images after application of a 4 V pulse.

that, the polarization domain pattern is imaged by PFM under a much lower mechanical load of about 100 nN. The resulting PFM images are shown in Figs. 7.16(a) and (b). The polarization in the center area has been switched to downward by the mechanical strain gradient generated by the AFM tip. Note that this type of polarization switching is not feasible with a conventional voltage switching method, since a voltage pulse would simply generate switching in the whole film underneath the graphene electrode. The mechanically switched polarization is electrically erasable by application of the opposite polarity voltage (Fig. 7.16, (c) and (d)).

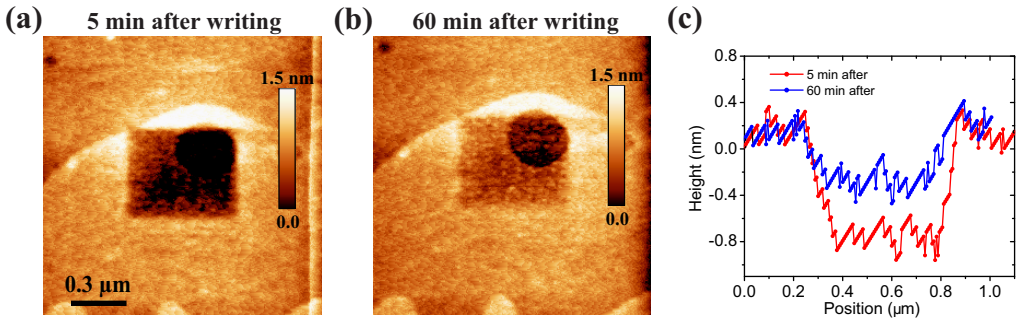

Figure 7.17: (a) Topography 5 min after mechanical writing. (b) Topography 60 min after mechanical writing. (c) Comparison of topography cross sections.

There is some topographic deformation in the mechanically scanned area, shown in Fig. 7.17(a). Previous investigation shows that there is no surface change to the ferroelectric surface after high mechanical scans [8]. We attribute this topography change to the removal of the fluidic (likely water) interfacial layer existing between graphene and barium titanate. An observation that supports this assumption is that this deformation gradually decreases and finally disappears with time (Fig. 7.17(b)).

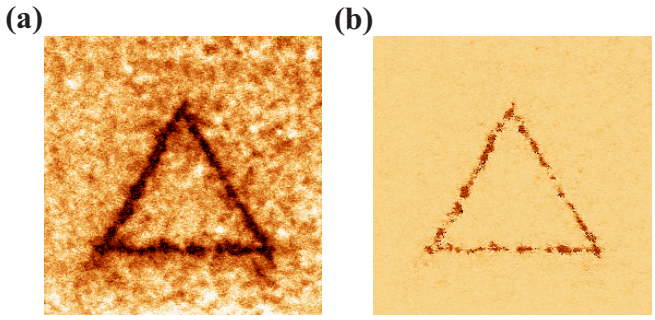

Figure 7.18: PFM amplitude (a) and phase (b) images of a triangle lines written mechanically.

Mechanical polarization switching through graphene is still highly localized. Figure 7.18 shows domain lines in the shape of a triangle mechanically written under 1600 nN load applied through graphene. The smallest domain generated can be as small as 20 nm. This feature enables for local controlled reversal of polarization in a

ferroelectric capacitor.

7.4 Finite Element Modeling of Strain Gradient Distribution

Finite element method is a numerical technique for finding approximate solutions to boundary value problems. The flexoelectric field is given by Eq. 7.1:

$$E_h = \frac{\mu_{ijkl}}{\epsilon_{ih}} \frac{\partial e_{jk}}{\partial x_l}, \tag{7.7}$$

where ϵ_{ih} is the dielectric constant and e_{jk} the strain. The vertical component of the flexoelectric field contains three components, namely, transverse, longitudinal and shear components in each parenthesis:

$$E_3 = (\frac{\mu_{3311}}{\epsilon_{33}} \frac{\partial e_{11}}{\partial x_3} + \frac{\mu_{3322}}{\epsilon_{33}} \frac{\partial e_{22}}{\partial x_3}) + (\frac{\mu_{3333}}{\epsilon_{33}} \frac{\partial e_{33}}{\partial x_3}) + (\frac{\mu_{1313}}{\epsilon_{33}} \frac{\partial e_{13}}{\partial x_1} + \frac{\mu_{2323}}{\epsilon_{33}} \frac{\partial e_{23}}{\partial x_2}). \tag{7.8}$$

The dielectric constant is $\epsilon_{33} = \epsilon_0 \epsilon_r$, where ϵ_0 is the permittivity of vacuum and $\epsilon_r = 30$ for compressively strained $BaTiO_3$ on $SrTiO_3$ [31]. The physics of switching under static regime and dynamic regime is different: in the static regime when there is no sliding, the shear strain gradients, which are big, cancel each other out exactly, and we are left only with transverse and longitudinal components, while in the dynamic regime when the tip is sliding, the shear strain gradients are asymmetric with respect to the tip moving direction, which cannot cancel out and in fact plays an important role. Here we first consider the static situation for simplification. Thus,

the flexoelectric field under the tip is:

$$E_3 = (\frac{\mu_{3311}}{\epsilon_{33}}\frac{\partial e_{11}}{\partial x_3} + \frac{\mu_{3322}}{\epsilon_{33}}\frac{\partial e_{22}}{\partial x_3}) + (\frac{\mu_{3333}}{\epsilon_{33}}\frac{\partial e_{33}}{\partial x_3}). \tag{7.9}$$

Once the flexoelectric field E_3 is known, its effect is calculated by adding the term $-E_3P$ to the standard Landau-Devonshire free energy [32] of an epitaxial film under uniaxial compression.

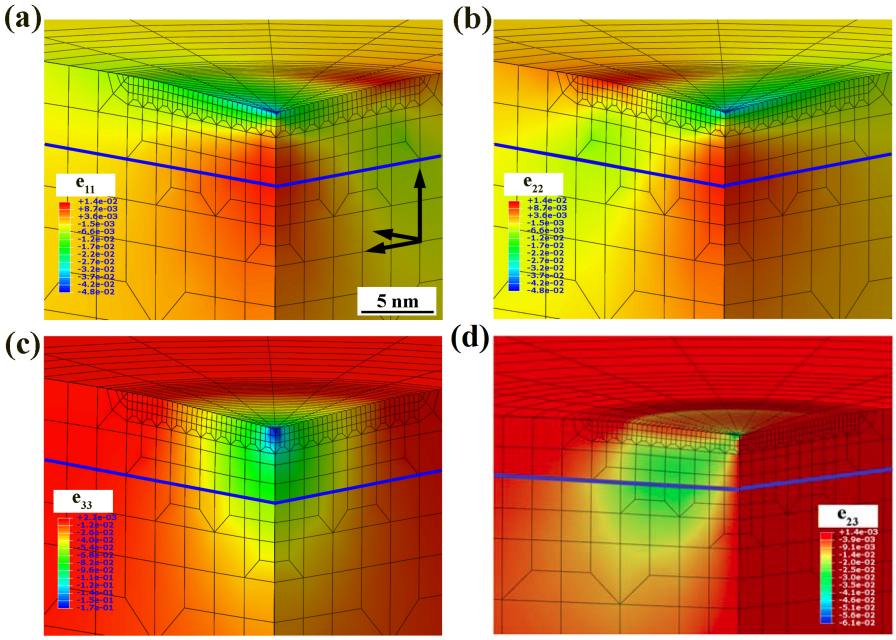

Figure 7.19: Finite element calculations of the strains distribution along the (a) x (e_{11}), (b) y (e_{22}), and (c) z (e_{33}) directions under static pressure from the AFM tip. (d) Finite element calculation map of the shear strain ($e_{13} = e_{23}$). All the strain components show gradients, with the shear strain gradient being the smallest one.

We performed finite-element calculations to model the strains e_{11}, e_{22} and e_{33} induced by the AFM tip when pressed against the $BaTiO_3$ film surface (the structure is sketched in Fig. structure). The calculations are for a tip force of 1000 nN over a tip-sample contact area of 10-nm radius, and the calculated strain distributions for all the strain components are mapped (Fig. 7.19). Using the calculated strain gradients,

the flexoelectric field is obtained by multiplying the strain gradient times the flexoelectric tensor and dividing by the dielectric constant [4, 7]. To be conservative in our calculations, we use the theoretical values for the flexoelectric tensor coefficients [33], which are a thousand times smaller than the experimental ones [27, 34].

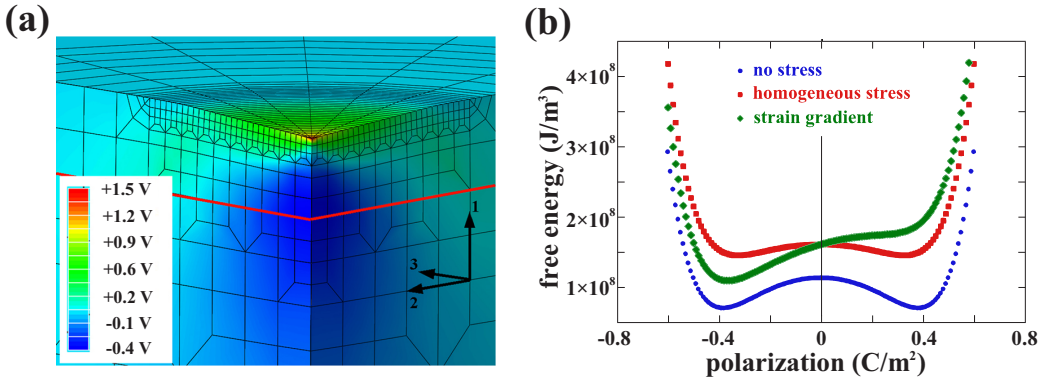

Figure 7.20: (a) Variation of the flexoelectric voltage in the film region under the tip, assuming a compressive uniaxial stress of 3.2 GPa, equivalent to 1 μN of force over a circular area of 10 nm in radius. The field is perpendicular to the voltage gradient and reaches a strength of ~2 MV/cm near the surface. (b) Free-energy calculations for the epitaxially clamped $BaTiO_3$ film without any tip pressure (blue curve), with homogeneous compressive stress of 3.2 GPa (red curve), and with the calculated flexoelectricity from the tip-induced strain gradient (green curve). Flexoelectricity skews the double well, forcing polarization switching toward the stable downward state.

To visualize the results and facilitate comparison with experiment, it is useful to introduce a concept of a "flexoelectric potential", V, whose gradient is the flexoelectric field: $E_3 \equiv \partial V/\partial x_3$. Comparing this with Eq. 7.9, we obtain the flexoelectric potential as:

$$V_3 = (\frac{\mu_{3311}}{\epsilon_{33}} e_{11} + \frac{\mu_{3322}}{\epsilon_{33}} e_{22}) + (\frac{\mu_{3333}}{\epsilon_{33}} e_{33}). \tag{7.10}$$

The flexoelectric potential under the tip, measured in Volts, is shown in Fig. 7.20. From this expression, flexoelectric potential is linearly proportional to strains, and strains are linearly proportional to stress, which gives a roughly linear relationship between flexoelectric potential and mechanical load applied to the tip, as we have

shown experimentally. Note that though Eq. 7.10 would imply that a homogeneous deformation also causes a non-zero voltage, this would however be constant across the film and would therefore have no physical consequence. Only potential differences matter, i.e. there is only a field if there is a potential *gradient*, which is the case when the induced deformation in inhomogeneous.

The flexoelectric field was also incorporated into free-energy calculations of the $BaTiO_3$ thin film epitaxially clamped on the $SrTiO_3$ substrate (Fig. 7.20(b)). Under a homogeneous compressive uniaxial stress [32], the height of the barrier separating the two energy minima is decreased, but the double well remains symmetric, and thus no specific polarity is favored, as expected from symmetry. Flexoelectricity, on the other hand, generates a polar bias consistent with the experimental observation of mechanical switching. When incorporated to the free energy, the flexoelectric bias destabilizes the positive side (upward-pointing polarization) of the double well and forces the switch to the downward-pointing polarization state, as observed. This is supported by PFM hysteresis loops measured during application of mechanical stress: the coercive bias has a negative shift as the tip pressure is increased.

For the loading force of 1000 nN, the calculated flexoelectric field reaches a maximum of 2 MV/cm, comparable with the intrinsic coercive field (theoretical) and that extracted from the piezo-electric hysteresis loops (experimental). Note that such a large flexoelectric field has been obtained in spite of our conservative choice of flexoelectric coefficients, supporting the feasibility of the flexoelectric switching mechanism. We stress that the Landau formalism provides an upper limit for the ideal (intrinsic) switching barrier; in practice, there will be defects that act as nucleation sites facilitating the switching at lower coercive fields. In real devices, therefore, the effective coercive field may be considerably lower than calculated here, meaning that the flexoelectric field will be capable of inducing switching at lower loads or larger

thicknesses than assumed here.

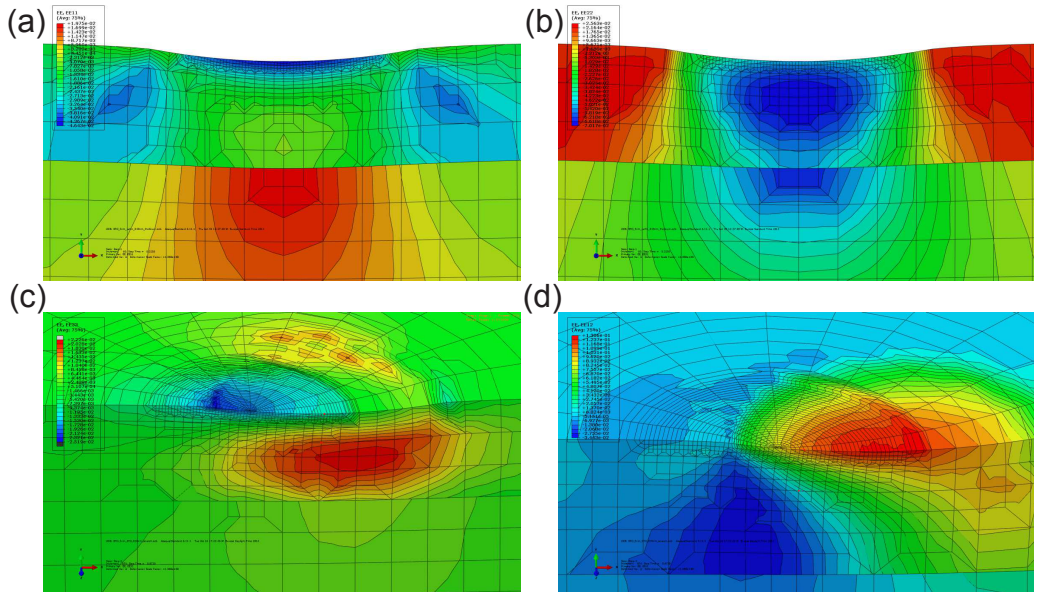

Figure 7.21: Finite element calculations of the strains distribution along the (a) x (e_{11}), (b) y (e_{22}), and (c) z (e_{33}) directions under static pressure from the AFM tip. (d) Finite element calculation map of the shear strain (e_{12}). There is a greater gradient when there is a sliding motion. In addition, the shear strains do not cancel each other.

In the dynamic regime, all the transverse, longitudinal and shear strains components have to be taken into consideration (Eq. 7.8). In addition to the normal force, there is a friction force in the tip sliding direction. The strain distribution is then asymmetric with respect to the tip moving direction due to the friction force. The shear strain then has much more significant contribution compared to just static pressing, making the high strain gradient penetrating even higher thicknesses. Fig. 7.21 shows an example of longitudinal and shear strain distribution maps from finite element calculation. There is a greater gradient when there is a sliding motion. An estimation shows that the flexoelectric potential generated in the dynamic regime is about 3 to 4 times of the one in static regime. However, in order to precisely calculate the flexoelectric potential, integration has to be over all three dimensional strain

components.

7.5 Conclusion

In conclusion, we have demonstrated that the strain gradient generated by the AFM tip pressing onto an ultrathin ferroelectric film can be used to switch the ferroelectric polarization in the ferroelectric film due to the flexoelectric effect. The observed effect of universal nature, which is demonstrated by mechanically-induced switching in other ferroelectrics. This effect has been used, for the first time, for deterministic domain control in ultrathin ferroelectric capacitors.

References

[1] P. Zubko, G. Catalan, and A. K. Tagantsev, Annu. Rev. Mater. Res. **43**, 387 (2013).

[2] S. M. Kogan, Sov. Phys. Solid. State **5**, 2069–2070 (1964).

[3] E. V. Bursian and O. I. Zaikovskii, Sov. Phys. Solid. State **10**, 1121–1124 (1968).

[4] J. F. Scott, J. of Chem. Phys. **48**, 874–878 (1968).

[5] A. K. Tagantsev, Phys. Rev. B **34**, 5883–5889 (1986).

[6] L. E. Cross, J. Mat. Sci. **41**, 53–63 (2006).

[7] W. Ma, Phys. Stat. Sol. (b) **245**, 761–768 (2008).

[8] H. Lu, C.-W. Bark, D. Esque de los Ojos, J. Alcala, C. B. Eom, G. Catalan, and A. Gruverman, Science **336**, 59–61 (2012).

[9] H. Lu, D. J. Kim, C. W. Bark, S. Ryu, C. B. Eom, E. Y. Tsymbal, and A. Gruverman, Nano Lett. **12**, 6289–6292 (2012).

[10] G. Zavala, J. H. Fendler, and S. Trolier-McKinstry, J. Appl. Phys. **81**, 7480 (1997).

[11] A. L. Kholkin, V. V. Shvartsman, A. Y. Emelyanov, R. Poyato, M. L. Calzada, and L. Pardo, Appl. Phys. Lett. **82**, 2127–2129 (2003).

[12] A. Gruverman, A. Kholkin, A. Kingon, and H. Tokumoto, Appl. Phys. Lett. **78**, 2751–2753 (2001).

[13] D. Lee, A. Yoon, S. Y. Jang, J.-G. Yoon, J.-S. Chung, M. Kim, J. F. Scott, and T. W. Noh, Phys. Rev. Lett. **107**, 057602 (2011).

[14] A. Gruverman, B. J. Rodriguez, A. I. Kingon, R. J. Nemanich, A. K. Tagantsev, J. S. Cross, and M. Tsukada, Appl. Phys. Lett. **83**, 728–730 (2003).

[15] G. Catalan, L. J. Sinnamon, and J. M. Gregg, J. Phys.: Cond. Mat. **16**, 2253–2264 (2004).

[16] G. Catalan, A. Lubk, A. H. Vlooswijk, E. Snoeck, C. Magen, A. Janssens, G. Rispens, G. Rijnders, D. H. Blank, and B. Noheda, Nature Mater. **10**, 963 (2011).

[17] M. S. Majdoub, P. Sharma, and T. Çağin, Phys. Rev. B **78**, 121407 (2008).

[18] C. B. Eom, R. J. Cava, R. M. Fleming, J. M. Phillips, R. B. Vandover, J. H. Marshall, J. W. P. Hsu, J. J. Krajewski, and W. F. Peck, Science **258**, 1766–1769 (1992).

[19] L. J. Belenky, X. Ke, M. Rzchowski, and C. B. Eom, J. Appl. Phys. **97**, 10J107 (2005).

[20] D. D. Fong, A. M. Kolpak, J. A. Eastman, S. K. Streiffer, P. H. Fuoss, G. B. Stephenson, C. Thompson, D. M. Kim, K. J. Choi, C. B. Eom, I. Grinberg, and A. M. Rappe, Phys. Rev. Lett. **96**, 127601 (2006).

[21] Y. Gaillard, A. Hurtado Macías, J. Muoz-Saldaa, M. Anglada, and G. Trápaga, J. Phys. D Appl. Phys. **42**, 085502 (2009).

[22] P. Vettiger, IEEE Trans. NanoTechnol. **1**, 39 (2002).

[23] V. Nagarajan, J. Junquera, J. Q. He, C. L. Jia, R. Waser, K. Lee, Y. K. Kim, S. Baik, T. Zhao, R. Ramesh, Ph. Ghosez, and K. M. Rabe, J. Appl. Phys. **100**, 051609 (2006).

[24] G. Catalan, J. Seidel, R. Ramesh, and J. F. Scott, Rev. Mod. Phys. **84**, 119 (2012).

[25] D. A. Bonnell, S. V. Kalinin, A. Kholkin, and A. Gruverman, MRS Bull. **34**, 648 (2009).

[26] V. Garcia, S. Fusil, K. Bouzehouane, S. Enouz-Vedrenne, N. D. Mathur, A. Barthélémy, and M. Bibes, Nature **460**, 81–84 (2009).

[27] W. Ma and L. E. Cross, Appl. Phys. Lett. **88**, 232902 (2006).

[28] P. Zubko, G. Catalan, A. Buckley, P. R. L. Welche, and J. F. Scott, Phys. Rev. Lett. **99**, 167601 (2007).

[29] H. Lu, X. Liu, J. D. Burton, C.-W. Bark, Y. Wang, Y. Zhang, D. J. Kim, A. Stamm, P. Lukashev, D. A. Felker, C. M. Folkman, P. Gao, M. S. Rzchowski, X. Q. Pan, C. B. Eom, E. Y. Tsymbal, and A. Gruverman, Adv. Mater. **24**, 1209 (2012).

[30] *http://en.wikipedia.org/wiki/Graphene.*

[31] S. Piskunov, E. Heifets, R.I. Eglitis, and G. Borstel, Comp. Mater. Sci. **29**, 165 (2004).

[32] A. Yu. Emelyanov, N. A. Pertsev, and A. L. Kholkin, Phys. Rev. B **66**, 214108 (2002).

[33] R. Maranganti and P. Sharma, Phys. Rev. B **80**, 054109 (2009).

[34] J. Hong, G. Catalan, J. F. Scott, and E. Artacho, J. Phys. Condens. Matter **22**, 112201 (2010).

Chapter 8

Mechanical Control of Resistive Switching in Ultrathin Ferroelectric Films

8.1 Introduction

Most of the nanoscale studies of the resistive switching phenomena including the TER effect [1] are based on electrical control of polarization using scanning probe microscopy (SPM) [2, 3, 4, 5, 6, 7, 8]. For experiments involving electrical poling by an SPM tip in ambient environment, there is always a concern that electrically induced changes in surface conditions, for example, due to redox chemical reactions or charge deposition, may significantly affect resistive switching measurements. Charge injection during switching pulse application may also take place [9] affecting the potential profile inside the ferroelectric barrier. This has raised questions regarding whether this surface modification is in fact the primary mechanism for the reported resistive switching effect as opposed to the mechanism based on the polarization-related change

in energy barrier between top and bottom electrodes. For example, redox reactions and associated band bending at the interfaces have been recently proposed as possible mechanisms for the TER effect in ultrathin ferroelectric films [10]. The main purpose of this chapter is to demonstrate that the nonvolatile TER effect in ultrathin (several nanometerthick) ferroelectric films can be induced by purely mechanical means and to show that this effect can be realized without any involvement of surface electrochemical processes commonly expected in SPM poling of oxide films. A comparison between electrically and mechanically induced TER effects allows the assessment of the surface charge influence on resistive switching.

Results described in this chapter have been published in ref. [11].

8.2 Mechanically-induced TER Effect in Ultrathin $BaTiO_3$ Films

A mechanically induced TER effect is facilitated by the flexoelectric switching of ferroelectric polarization [12] described in the previous chapter. As it has been found that the AFM tip-generated strain gradient can produce a flexoelectric field that is strong enough to switch polarization in a way similar to an external electric field, it seems natural to see if mechanical stress could be also used to control the resistive switching behavior. To explore the mechanically induced TER effect, we have used epitaxial single-crystalline ultrathin 12 u.c. (4.8 nm) $BaTiO_3$ films grown by pulsed laser deposition on atomically smooth TiO_2-terminated (001)-$SrTiO_3$ substrate with $SrRuO_3$ as a bottom electrode. It has been shown previously [13] that compressively strained $BaTiO_3$ films on $SrTiO_3$ substrates possess only out-of-plain polarization.

Preliminary testing of the samples by PFM shows that the as-grown $BaTiO_3$ films

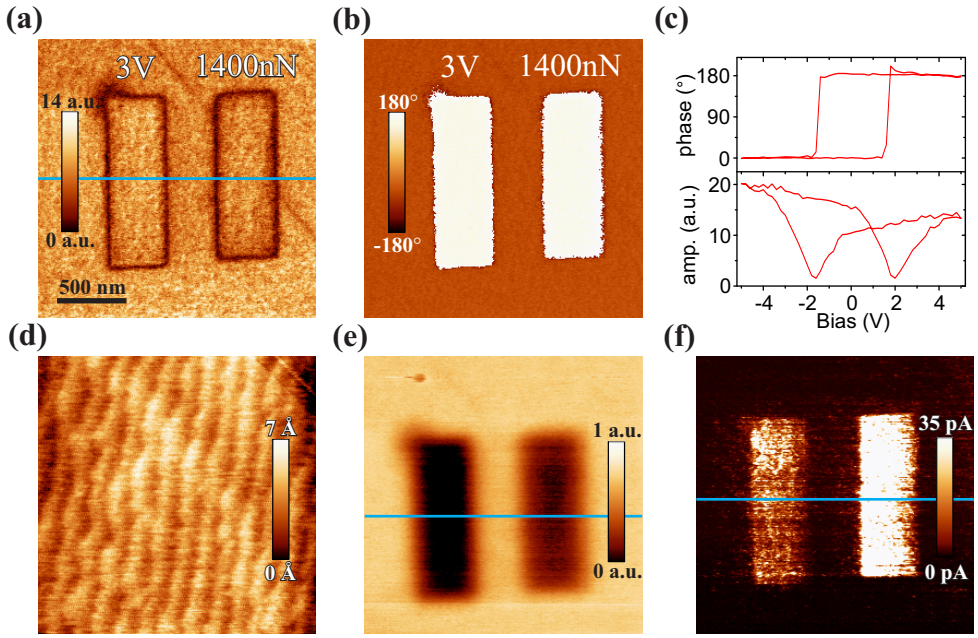

Figure 8.1: SPM data illustrating the mechanically and electrically induced TER effects. (a, b) PFM amplitude (a) and phase (b) images of the 4.8-nm-thick $BaTiO_3$ film after the generation of the downward-oriented domains by electrical poling (left) and mechanical loading force (right). A saturated amplitude signal indicates fully polarized states. (c) Local PFM hysteresis loops measured in the same $BaTiO_3$ film. (d) Topographic image of the same area acquired after mechanical writing showing that the film surface was not affected by the writing process. (e) EFM image taken at the same location as the PFM images. The EFM image was acquired with a dc read voltage of +2 V. Regions of dark contrast represent downward oriented domains and correspond to a positive surface screening charge. (f) Tunneling current map acquired in the C-AFM mode with a dc read bias 0.3 V at the same location as the PFM and EFM images. The bright contrast corresponds to a higher conductivity. Figure addapted from ref. [11]

are in a single-domain state with the upward (away from the substrate) polarization direction. These initial conditions turn out to be suitable for our studies as the tip-induced mechanical load can switch the polarization only from upward to downward direction [12]. Figure 8.1, (a) and (b) show the PFM amplitude and phase images, respectively, of two downward-oriented domains written in as-grown film: the left domain has been written with an electrically biased tip (+3 V) and a load of 20 nN

(which is a typical value for the PFM operation mode), whereas the right domain has been produced by scanning the film surface with a grounded tip while applying a mechanical load of 1400 nN. (Although it is difficult to precisely convert the applied mechanical load to equivalent potential, it had been shown earlier [12] that the load of 700 nN generated a voltage comparable with the coercive bias; thus it is natural to expect complete polarization reversal at a higher load of 1400 nN). After writing, PFM imaging of the resulting domain pattern has been carried out with the same tip at a contact loading force of 20 nN. Both domains exhibit a saturated PFM amplitude signal and 180° phase inversion, indicating a fully switched single domain state. Switchable polarization behavior is confirmed by the local PFM spectroscopic measurements (Fig. 8.1(c)), which show rather symmetric piezoelectric hysteresis loops with a coercive voltage of ~2.0 V (or coercive field of ~4 MV/cm). The topographic image of the film surface acquired after writing (Fig. 8.1(d)) does not show any sign of plastic surface deformation. No PFM signal relaxation several days after mechanical writing has been detected, suggesting strong polarization retention. A noteworthy feature of the mechanically written domain is that it is electrically erasable [12].

Additional analysis of the written domain pattern has been performed using electrostatic force microscopy (EFM) (Fig. 8.1(d)). Note that EFM is sensitive to the presence of the surface charge and thus can be used to assess the difference between surface charge density of electrically and mechanically produced domains. In the EFM imaging conditions used in our study, the dark contrast of the written domains corresponds to a positive surface charge. This is opposite to the negative bound polarization charge of the domains, suggesting that the signal detected by EFM is due to a surface charge that screens polarization of the downward-oriented domains. There is a clear disparity of the EFM signal between electrically written and mechanically written domains. A much darker contrast for the electrically produced domain indi-

cates a higher screening charge density. This effect could be due to the field-induced redox reaction resulting in deposition of extra charge in addition to the adsorption of ionic species from ambient [14].

The resistive switching behavior has been studied by simultaneous imaging of the electrically and mechanically written domains in the C-AFM mode. Figure 8.1(e) shows a current map where contrast variations correspond to changes in conductivity. It can be seen that both electrically and mechanically poled domains with downward polarization have higher conductivity in comparison to the as-grown $BaTiO_3$ film with upward polarization, which is indicative of the resistive switching effect. As no plastic surface deformation due to the tip-induced pressure has been observed, we can exclude a change in film thickness as a root cause for the observed TER. It can be concluded then that it is the change in the energy barrier height due to polarization reversal that lead to the electroresistance effect [15]. Also, the fact that the TER effect can be induced by mechanical pressure without any electrical bias application indicates that the electrochemical surface modification or charge injection as the main mechanisms of resistive switching in ferroelectrics can be ruled out.

Figure 8.2(a) summarizes the obtained results in the form of cross-section analysis of the PFM amplitude and EFM and C-AFM images: there is no discernible difference between the PFM images of electrically and mechanically written domains, while the EFM signal shows a clear difference, indicating a surface charge modification as a result of electric voltage application. As for the resistance change, it is interesting that mechanically induced TER is larger than the electrically induced TER. This observation is supported by local spectroscopic measurements (Fig. 8.2(b)): the resistance changes by 2300% for electrically poled domain versus 7300% resistance change for the mechanically written domain. Note that similar results have been obtained for mechanical writing carried out under open and short circuit boundary conditions

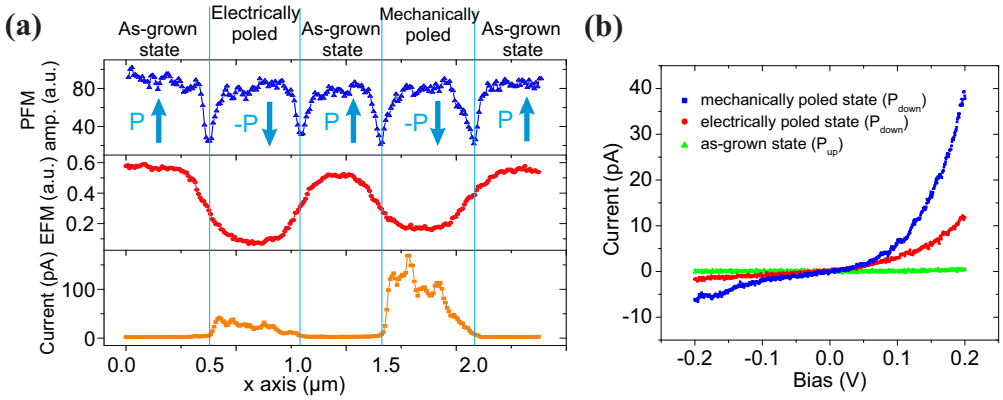

Figure 8.2: Comparative analysis of the mechanically and electrically induced TER effects. (a) Cross sections through the lines shown in the PFM amplitude, EFM, and current maps (Fig. 8.1, (a), (e), and (f), respectively). (b) Local I–V curves measured for the as-grown film area with upward polarization (green), electrically downward-switched domain (red), and mechanically downward-switched domain (blue). Figure addapted from ref. [11]

using insulating and grounded conductive tips, respectively. It should be also noted that scanning the surface with a tip under an increased load may result in partial removal of surface adsorbate layer, thereby affecting the comparison between conductivity of mechanically and electrically written domains. To address this issue, we first mechanically wrote a downward domain and then electrically switched it upward. This procedure created a domain with the same polarization as in the virgin film but with a cleaner surface. After that mechanical and electrical writing of the downward domains has been performed again as described above. It has been found that in this case mechanically written domain still exhibits a significantly stronger TER than the electrically poled domain, although the difference becomes smaller.

8.3 Modeling of the TER Effect

Our earlier studies [2] demonstrated that the significant enhancement of conductance with reversal of ferroelectric polarization from upward to downward state is largely

due to the electrostatic modulation of the potential step at the tip/BTO interface resulting in the change of the energy barrier across the $BaTiO_3$ layer. Figure 8.3 il-

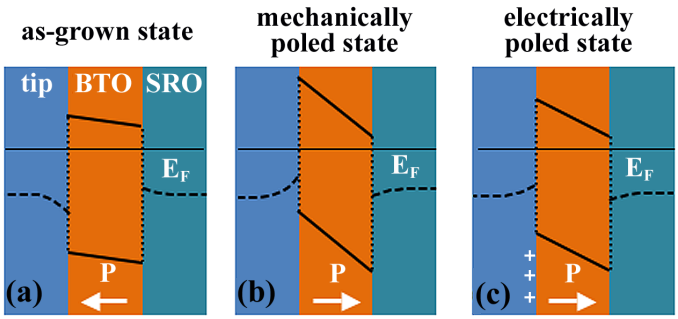

Figure 8.3: Schematic band diagrams of the FTJ formed by the $BaTiO_3$ (BTO) film sandwiched between the bottom $SrRuO_3$ (SRO) electrode and a conductive SPM tip: (a) for the as-grown upward polarization (toward the tip), (b,c) for the mechanically and electrically poled downward polarization (toward the bottom electrode), respectively. The dashed lines in the electrodes and tip regions indicate schematically a variation in the electrostatic potential. For the downward polarization the Fermi energy (solid horizontal line) lies farther from the conduction band of $BaTiO_3$, resulting in the enhanced conductance due to the decay constant increase with energy. Accumulation of an additional positive charge on the top surface when the polarization is switched electrically pushes the conduction band of $BaTiO_3$ down, resulting in the conductance decrease. Figure addapted from ref. [11]

lustrates the band alignment associated with polarization reversal. It can be seen that switching of the polarization direction toward the substrate pushes the conduction band up with respect to the Fermi energy thereby increasing conductance (Fig. 8.3 (a) and (b)). This behavior is due to the decay constant associated with the evanescent state responsible for tunneling in $BaTiO_3$, which increases with energy [16, 17]. A difference in conductance between electrically and mechanically written downward domains can be understood from the following consideration. Ferroelectric polarization screening of as-grown BTO film is realized through adsorption of charged species and dipolar molecules on the ferroelectric surface after it has been exposed to air [18]. Ferroelectric polarization reversal from upward to downward alters the screen-

ing charge on the surface of the newly written domains as confirmed by our EFM measurements. The higher screening charge density in the case of electrically written domain implies that there is a positive extra charge injected into the adsorbate layer, which likely "overscreens" the polarization charge. This extra charge may result from redox reactions driven by the electrical bias applied to the SPM tip. Accumulation of the additional positive charge on the ferroelectric surface pushes the conduction band of $BaTiO_3$ down altering the band alignment as shown in Fig. 8.3(c). This results in the reduced conductance of the electrically written domains in comparison with the domain produced by mechanical means.

8.4 Conclusion

In summary, we have experimentally demonstrated a mechanically induced tunneling electroresistance effect in ultrathin ferroelectric films. This effect is facilitated by flexoelectric switching of polarization due to the strain gradient developed under the SPM tip pressed against the film surface. Strain-mediated voltage-free generation of a stable, fully reversible and reproducible TER effect represents an important breakthrough on both conceptual and practical levels. From the conceptual point of view, it demonstrates mechanical control of electronic properties of ferroelectrics, which can be extended to other functional oxide materials. From the practical point of view, it opens the possibility for application in low-energy archive data storage devices with mechanical writing and electrical reading of data.

References

[1] E. Y. Tsymbal and H. Kohlstedt, Science **313**, 181 (2006).

[2] A. Gruverman, D. Wu, H. Lu, Y. Wang, H. W. Jang, C. M. Folkman, M. Y. Zhuravlev, D. Felker, M. Rzchowski, C.-B. Eom, and E. Y. Tsymbal, Nano Lett. **9**, 3539 (2009).

[3] V. Garcia, S. Fusil, K. Bouzehouane, S. Enouz-Vedrenne, N. D. Mather, A. Barthélémy, and M. Bibes, Nature **460**, 81 (2009).

[4] E. Y. Tsymbal, A. Gruverman, V. Garcia, M. Bibes, and A. Barthélémy, MRS Bull. **37**, 138 (2012).

[5] D. Pantel, S. Goetze, D. Hesse, and M. Alexe, Nat. Mater. **11**, 289 (2012).

[6] M. Hambe, A. Petraru, N. A. Pertsev, P. Munroe, V. Nagarajan, and H. Kohlstedt, Adv. Funct. Mater. **20**, 2436 (2010).

[7] P. Maksymovych, S. Jesse, P. Yu, R. Ramesh, A. P. Baddorf, and S. V. Kalinin, Science **324**, 1421 (2009).

[8] Y. W. Yin, M. Raju, W. J. Hu, X. J. Weng, X. G. Li, and Q. Li, J. Appl. Phys. **109**, 07D915 (2011).

[9] S. Buhlmann, E. Colla, and P. Muralt, Phys. Rev. B **72**, 214120 (2005).

[10] N. C. Bristow, M. Stengel, P. B. Littlewood, J. M. Pruneda, and E. Artacho, Phys. Rev. B **85**, 024106 (2012).

[11] H. Lu, D. J. Kim, C.-W. Bark, S. Ryu, C. B. Eom, E. Y. Tsymbal, and A. Gruverman, Nano Lett. **12**, 6289 (2012).

[12] H. Lu, C.-W. Bark, D. Esque de los Ojos, J. Alcala, C. B. Eom, G. Catalan, and A. Gruverman, Science **336**, 59 (2012).

[13] K. J. Choi, M. Biegalski, Y. L. Li, A. Sharan, J. Schubert, R. Uecker, P. Reiche, Y. B. Chen, X. Q. Pan, V. Gopalan, L.-Q. Chen, D. G. Schlom, and C. B. Eom, Science **306**, 1005 (2004).

[14] D. D. Fong, A. M. Kolpak, J. A. Eastman, S. K. Streiffer, P. H. Fuoss, G. B. Stephenson, C. Thompson, D. M. Kim, K. J. Choi, C. B. Eom, I. Grinberg, and A. M. Rappe, Phys. Rev. Lett. **96**, 127601 (2006).

[15] M. Y. Zhuravlev, R. F. Sabirianov, S. S. Jaswal, and E. Y. Tsymbal, Phys. Rev. Lett. **94**, 246802 (2005).

[16] J. P. Velev, C.-G. Duan, J. D. Burton, A. Smogunov, M. K. Niranjan, E. Tosatti, S. S. Jaswal, and E. Y. Tsymbal, Nano Lett. **9**, 427 (2009).

[17] D. Wortmann and S. Blügel, Phys. Rev. B **83**, 155114 (2011).

[18] R. V. Wang, D. D. Fong, F. Jiang, M. J. Highland, P. H. Fuoss, C. Thompson, A. M. Kolpak, J. A. Eastman, S. K. Streiffer, A. M. Rappe, and G. B. Stephenson, Phys. Rev. Lett. **102**, 47601 (2009).

Chapter 9

Ferroelectric Modulation of Magnetization in Ferroelectric/Ferromagnetic Heterostructures

9.1 Introduction

Multiferroic materials are a type of materials that exhibit more than one ferroic order parameter simultaneously, such as ferromagnetism, ferroelectricity and ferroelasticity, etc. One of the most appealing aspects of multiferroics is their so-called magnetoelectric coupling, where a magnetic field can tune the electric polarization and an electric field can tune the magnetization.

While the possibility of a magnetoelectric effect was first mentioned by Pierre Curie in 1894 [1] and predicted to exist in Cr_2O_3 in 1960 [2], until recently it was assumed that the external electric fields cannot significantly alter the properties of

magnetic materials. The effect was considered simply too small for any practical applications. The experimental observation of electrical modulation of magnetization in III-V magnetic semiconductors [3] sparked a surge of activity in search of other materials exhibiting magnetoelectric coupling. Breakthrough possibilities have been offered with the recent advances in fundamental understanding and experimental studies of coexistence of ferroelectric and ferromagnetic ordering in multiferroic materials [4, 5]. As single-phase room-temperature multiferroics are rare in nature (with Cr_2O_3 as a noticeable exception [6]), artificial multiferroic heterostructures made of ferroelectric and ferromagnetic phases have been extensively engineered and studied in search for large magnetoelectric coupling [7, 8, 9, 10]. Among the most attractive materials for practical implementation of multiferroic heterostructures and fundamental studies of magnetoelectric coupling are the doped lanthanum manganites $La_{1-x}A_xMnO_3$, (A = Ca, Sr, or Ba) [11]. These materials are characterized by a strong interplay between electron transport, magnetism, and crystal lattice distortions and a rich carrier-density-temperature phase diagram. A possibility of effective electrical modulation of carrier concentration and magnetic properties makes these materials extremely attractive for numerous applications in field-effect devices [12]. Modulation of carrier density in metallic manganite films can be realized by employing polarization ferroelectric materials as the gate electrodes [13]. The sensitivity of the magnetic state of manganites to electrical charge was predicted for $BaTiO_3/La_{1-x}Sr_xMnO_3$ (BTO/LSMO) interfaces [14] and experimentally explored using spin-dependent tunneling [15]. A number of theoretical and experimental studies [16, 17, 18, 19, 20, 21] attributed magnetoelectric coupling to the interplay between changes in magnetization and accumulation/depletion states at the ferroelectric-ferromagnetic interfaces, which is fundamentally different from the coupling mechanism in single phase materials.

In this chapter, we investigate modulation of magnetization by ferroelectric polarization reversal in ferroelectric-ferromagnetic heterostructures of $BaTiO_3$/(La,Sr)MnO_3 /$SrTiO_3$ (BTO/LSMO/STO). We find that the effect is limited to the BTO/LSMO interface but extends up to about 3 nm into the LSMO layer beyond the expected screening length of metallic LSMO. It is suggested that the latter effect is due to a metal-insulator transition occurring at the BTO/LSMO interface as a result of electrostatic doping.

Results described in this chapter have been published in ref. [22].

9.2 Materials and Methods

Pulsed laser deposition was used to grow atomically flat single-crystalline epitaxial $BaTiO_3$ films on TiO_2-terminated $SrTiO_3$ substrates with the $La_{0.67}Sr_{0.33}MnO_3$ films of variable thickness as bottom electrodes. It has been shown previously [23] that growing compressively strained $BaTiO_3$ films on $SrTiO_3$ substrates enhances the resulting polarization and aligns it normal to the surface. In our studies, thickness of $BaTiO_3$ was chosen to be 48 unit cells (~19 nm) to ensure stable and switchable polarization, and LSMO thickness varied in the range from 10 to 50 nm. Structural quality and ferroelectric properties of the grown heterostructures are very similar to those reported in our earlier studies [24]. The atomic force microscopy (AFM) topographic image of the surface morphology in Fig. 9.1(a) shows atomically flat terraces with one unit-cell high (~4 Å) steps indicating epitaxial structure of the $BaTiO_3$ films. Details on sample preparation can be found elsewhere [23].

Superconductivity quantum interference device (SQUID) magnetometer (MPMS, Quantum Design) and Kerr microscope based on longitudinal magnetooptical Kerr effect (MOKE) have been used to measure magnetization of LSMO films. MOKE

measurements have been performed by focusing the green (λ=532 nm) laser beam to the spot of less than 100 μm indiameter on the $BaTiO_3$ surface.

9.3 Large-scale Polarization Control in Ultrathin Ferroelectric Films

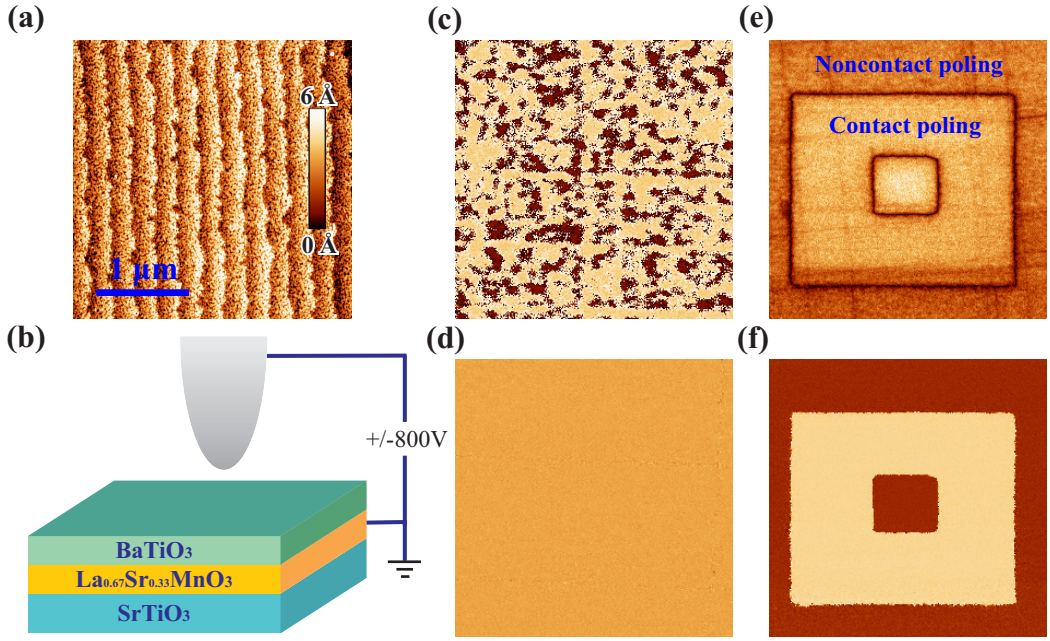

Figure 9.1: (a) AFM image of $BaTiO_3$ surface topography showing terraces and periodic steps with a unit-cell height. (b) Schematic illustration of non-contact macroscopic poling method: a large needle held at a dc bias of ±800V and at ~100 μm above sample surface scans the sample surface ($5\times5mm^2$) in high vacuum conditions. The step increment during scanning was 50 μm. (c) PFM phase image of the polydomain structure of the as-grown BTO film. (d) PFM phase image of the uniformly polarized BTO film after noncontact poling. (e), (f) PFM amplitude (e) and phase (f) images showing comparison between the macroscopic non-contact poling and poling by PFM. Central 2×2 μm^2 and 0.5×0.5 μm^2 squares have been produced by scanning with an AFM tip under +4 V/−4 V dc bias in contact mode, while an outer region shows the result of macroscopic non-contact poling. Saturated polarization has been obtained for both poling methods. Scan size is the same for all AFM/PFM images. Figure adapted from ref. [22].

Investigation of magnetic response by means of SQUID requires large-scale sample area poling (about several mm^2), which is difficult to accomplish if the ferroelectric film does not have a top electrode (for comparison, an AFM with a conductive probe can only pole an area of up to 150×150 μm^2 which might also take up to an hour of scanning). To overcome this problem, we have employed macroscopic non-contact probe poling technique. A Pt needle with the 20-μm-apex-curvature-radius held at a distance of about 100 μm above the BTO film surface and electrically biased at ±800V scanned the whole sample area in high vacuum conditions (4×10^{-9} Torr) as is schematically shown in Fig. 9.1(b). PFM analysis of several regions over the sample surface has been used to verify the result of non-contact poling.

Figure 9.1, (c) and (d) show 3×3 μm^2 PFM phase images of the BTO film before and after noncontact poling demonstrating that the polarization had been effectively switched from as-grown polydomain state to a single domain state. Figure 9.1, (e) and (f) show a comparison of the poling results by the macroscopic non-contact method and by PFM (in PFM, the BTO film has been poled by scanning the surface in contact with the PFM probe under a ±4V dc bias). It can be seen that both poling methods result in fully switched single-domain polarization states.

9.4 Electrical Modulation of Magnetization in BTO/LSMO/STO Heterostructures

SQUID measurements of the BTO/LSMO/STO heterostructures have been performed for both BTO polarization directions after verification of the results of large-scale noncontact poling by PFM. Cycles of the BTO films poling followed by the SQUID measurement have been carried out several times to ensure that magnetic response of

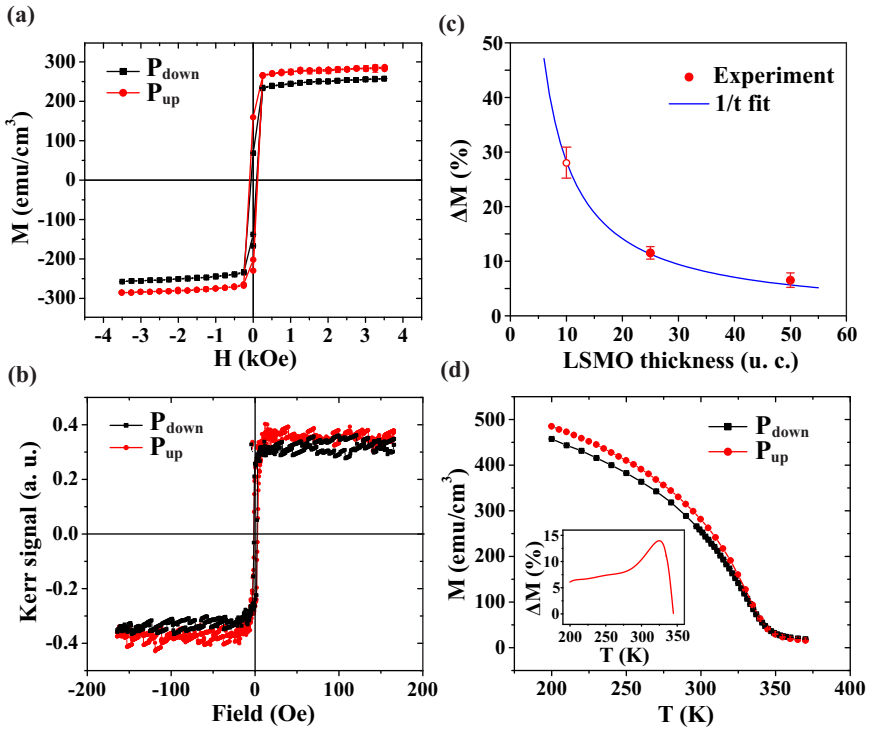

Figure 9.2: (a) In-plane M–H curves of BTO/LSMO(25 nm) heterostructure measured by SQUID at room temperature for upward and downward polarization directions in BTO. (b) In-plane M–H curve of BTO/LSMO(10 nm) heterostructure measured by MOKE at room temperature for upward and downward polarization directions in BTO showing the same trend as in (a). (c) Dependence of the relative change of magnetization ΔM on the LSMO layer thickness t. The open circle indicates a normalized data point. The solid curve is a fit to the $1/t$ function. (d) Temperature dependence of saturation magnetization of BTO/LSMO(25 nm) heterostructure for upward and downward BTO polarizations measured at 2500 Oe. The inset shows temperature dependence of the relative magnetization change ΔM. Figure adapted from ref. [22].

the LSMO layer is reproducible and not affected by possible artifacts, such as sample misalignment. Typical in-plane magnetization curves of LSMO acquired at room temperature for two antiparallel polarization states of the BTO film are shown in Fig. 9.2(a). It is seen that polarization reversal in BTO leads to a sizable change in the magnetic moment of the adjacent LSMO layer. For all studied samples, the magnetic moment of LSMO decreases as the BTO film is electrically switched from the

upward (away from the substrate) to downward (toward the substrate) polarization state.

To substantiate the results obtained by SQUID, additional measurements by local MOKE measurements have been performed using the same samples. Ferroelectric poling of two regions of approximately 100×100 μm^2 of the BTO film have been carried out using a conductive PFM probe in contact with the surface by applying a dc bias of ±5V, followed by MOKE measurements of in-plane magnetization (using surface topographic markers the laser spot was focused on exactly the same regions where polarization reversal had been performed). The results in Fig. 9.2(b) indicate the same trend as those in Fig. 9.2(a): LSMO magnetization decreases when the polarization in the BTO layer is switched from the upward to downward direction.

Further, we studied the relative change in saturated magnetization, $\Delta M = (M(P_{up}) - M(P_{down}))/M(P_{down})$, as a function of LSMO thickness (Fig. 9.2(c)). It should be mentioned that both upward and downward polarization states in the BTO film were found to be stable for the 25- and 50-nm-thick LSMO layers, while for the 10-nm-thick LSMO layer, only upward polarization was found to be stable. Attempts to switch the BTO film downward in this case resulted in formation of the polydomain structure with the Pdown/Pup ratio of approximately 1/2 (most likely due to spontaneous backswitching). This effectively means that only 1/3 of the total downward polarization state had contributed to the magnetization change. By taking into account this correction, which reflects non-complete downward poling, the resulting relative magnetization change ΔM was estimated to be about 27% (without this correction the measured ΔM value was ~9%).

Figure 9.2(d) shows a temperature dependence of saturated magnetization in the BTO/LSMO(25 nm)/STO heterostructure measured at a constant magnetic field 2500 Oe. No noticeable change in the Curie temperature with polarization reversal

has been observed. The temperature dependence of ΔM (see the inset in Fig. 9.2(d)) shows that the polarization-induced change in magnetization peaks in the vicinity of the Curie temperature and decreases as temperature decreases.

Data in Fig. 9.2(c) show that the relative change in magnetization ΔM becomes more pronounced as the LSMO thickness decreases. The thickness dependence of ΔM can be fitted well to the t_m/t function, where t is the LSMO layer thickness and t_m is the fitting parameter. This suggests an interface mechanism behind the observed magnetization modulation by polarization reversal, i.e., that the magnetization change in LSMO is limited to a thin layer at the BTO/LSMO interface. The fit allows us to estimate the effective layer thickness at the BTO/LSMO interface where the magnetization change occurs. Assuming that within this layer the reversal of ferroelectric polarization completely destroys magnetism, we can interpret t_m as the thickness of this layer. From the fit we find that t_m is approximately 2.9 nm.

9.5 Phenomenological Modeling

The observed effect is in qualitative agreement with our first-principles calculations performed using the plane-wave pseudopotential method [25]. Reversal of the ferroelectric polarization leads to a change in the accumulation/depletion charge built up on the LSMO side of the interface. We find that all of the electronic screening is limited to an accumulation/depletion of majority spin electrons, which leads to a significant change in magnetic moment near the interface. In bulk, $La_{0.67}Sr_{0.33}MnO_3$ has a magnetization of 3.67 μ_B/Mn, whereas the average Mn moment varies significantly in the first 2–3 unit-cells near the interface with BTO, depending on the polarization orientation. For the BTO polarization pointing towards the BTO/LSMO the interface, for example, the magnetic moments on the Mn sites are essentially the same as

they are in the bulk [14], leading to a near complete absence of electronic screening. On the other hand, for the BTO polarization pointing away from this interface, the negative surface polarization charge from the BTO leads to a significant depletion of majority spin electrons in the first 2–3 unit-cells of LSMO: the first Mn layer at the interface is reduced by ~0.45 μ_B, the second is reduced by ~0.2 μ_B, and the third is reduced by ~0.05 μ_B. This corresponds to an effective penetration depth of the magnetoelectric response on the order of 0.8–1.2 nm in our zero temperature calculations, which in qualitative agreement with our experimental results.

Quantitatively, however, the experimentally observed magnetoelectric effect is significantly larger in magnitude than that predicted theoretically. Also, the thickness of the ferroelectrically modulated magnetic layer estimated from the experimental data is much larger than theoretically predicted (~3 nm versus ~1 nm, respectively), which cannot be explained solely within the model assuming uniform and constant metallicity of LSMO at the BTO/LSMO interface. Below, we propose a qualitative model, which explains our experimental data based on the metal-insulator transition at the LSMO interface induced by the ferroelectric polarization.

The screening charge at the ferroelectric-manganite interface produces carrier depletion or accumulation in LSMO near the interface, analogous with chemical doping. Since x in the $La_{1-x}Sr_xMnO_3$ chemical formula reflects the substitution of trivalent La with divalent Sr and is an effective measure of holes concentration, we can consider the effect of electric field as a corresponding shift in the LSMO phase diagram [11] (Fig. 9.3(a)) to the right, if a negative polarization charge is to be screened, or to the left, if positive polarization charge is to be screened, relative to the starting point of $x = 0.33$. It can be seen from the diagram that while the rightward shift keeps the LSMO layer in the metallic state, the leftward shift can lead to a metal-insulator transition. The presence of the metal-insulator transition occurring locally, within the

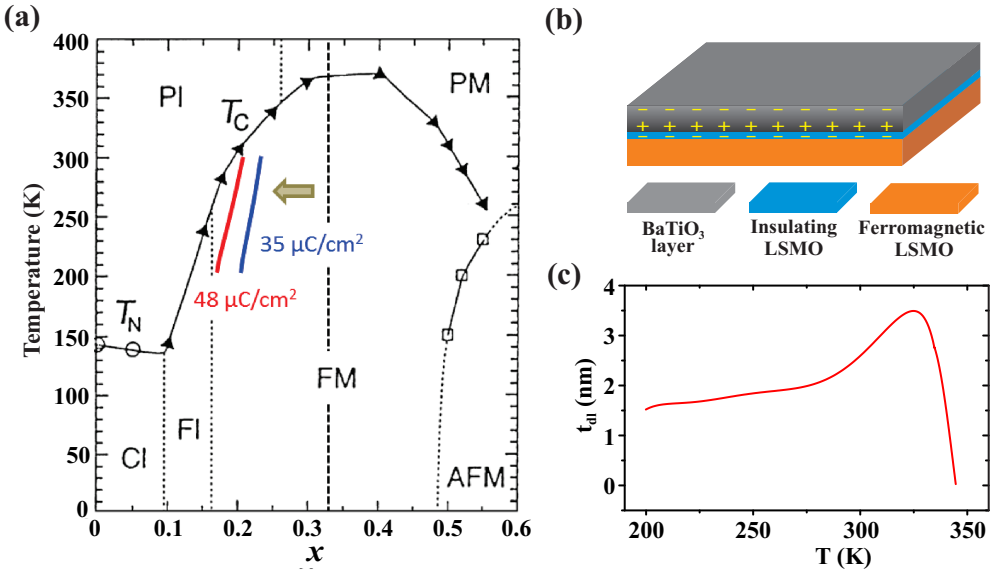

Figure 9.3: (a) Temperature-composition phase diagram of LSMO showing ferromagnetic metal (FM), paramagnetic insulator (PI), ferromagnetic insulator (FI), and paramagnetic metal (PM) phases. Also shown are calculations of the shift of the phase boundary between insulating and metallic states for two possible $BaTiO_3$ polarization values. Polarization screening shifts the effective charge concentration x at the interface: the leftward shift leads to metal-insulator transition while the rightward shift keeps the system in the metallic state. (b) Schematic illustration of the metal-insulator phase transition in LSMO due to accumulation of screening charges at the BTO/LSMO interface. (c) Temperature dependence of the thickness of the magnetically modulated layer in LSMO. Figure adapted from ref. [22].

screening length at the LSMO interface, would inevitably move the screening region deeper into the bulk LSMO (Fig. 9.3(b)). For example, assuming that the strained BTO has the polarization of 48 $\mu C/cm^2$, and all the screening charge is accumulated within 2.5 unit cells of LSMO (as in our theoretical calculations), the total doping (both chemical and electrostatic) within the screening region becomes $x \approx 0.13$, which lies deep in the paramagnetic insulator region at room temperature in the phase diagram of LSMO (Fig. 9.3(a)). This suggests that the screening region expands beyond that found for the metallic phase of LSMO (Fig. 9.3(b)). This effect is expected to be more pronounced in the vicinity of T_C, where the difference in free energy between

the metal and insulating states for the LSMO film is minimal.

In order to correlate our experimental results with the phase diagram of LSMO, we have calculated the occurrence of the metal-insulator phase transition based on our experimental data for the polarization-induced change in magnetization shown in the inset of Fig. 9.2(d). Assuming as before that within the layer of thickness tm ferroelectric polarization reversal completely destroys magnetism, we can calculate t_m as a function of temperature ((Fig. 9.3(c)). Using this temperature dependence and known values of the polarization charge for BTO we can find the phase boundary between the metal and insulator regions in the phase diagram simply by estimating the amount of doping level in the layer of thickness t_m as a function of temperature. The estimated equivalent changes in the holes concentrations (change in x) that are required to accommodate all the polarization charge are shown in (Fig. 9.3(a) for two $BaTiO_3$ polarization values: experimentally measured [26] value of 35 $\mu C/cm^2$ and predicted in our first-principles calculations value of 48 $\mu C/cm^2$. There is a clear correlation between the bulk phase diagram of LSMO and the predicted metal-insulator phase boundaries.

9.6 Conclusion

In summary, we have observed large (>10%) roomtemperature electrical modulation of magnetization in ferroelectric/ferromagnetic $BaTiO_3/La_{0.67}Sr_{0.33}MnO_3/SrTiO_3$ heterostructures induced by polarization reversal in $BaTiO_3$. The relative magnetization change is inversely proportional to the LSMO layer thickness, indicating that the effect is limited to a thin (~3 nm) LSMO layer at the BTO/LSMO interface. The thickness of this layer and the magnitude of magnetization change are significantly larger than those predicted by first-principle calculations at zero temperature. The experimental

data can be qualitatively explained using a model based on a polarization-induced metal-insulator transition in the LSMO layer near the interface.

References

[1] M. P. Curie, J. de Phys., 3e série, t. III **3**, 393 (1894).

[2] E. Dzyaloshinskii, Sov. Phys. JETP **10**, 628629 (1960).

[3] H. Ohno, D. Chiba, F. Matsukura, T. Omiya, E. Abe, T. Dietl, Y. Ohno, and K. Ohtani, Nature **408**, 944 (2000).

[4] W. Eerenstein, N. D. Mathur, and J. F. Scott, Nature **442**, 759 (2006).

[5] N. A. Spaldin, S.-W. Cheong, and R. Ramesh, Phys. Today **64**, 9 (2011).

[6] X. He, Y. Wang, N. Wu, A. N. Caruso, E. Vescovo, K. D. Belashchenko, P. A. Dowben, and Ch. Binek, Nat. Mater. **9**, 579 (2010).

[7] M. Fiebig, J. Phys. D **38**, R123 (2005).

[8] K. F. Wang, J.-M. Liu, and Z. F. Ren, Adv. Phys. **58**, 321 (2009).

[9] J. Ma, J. Hu, Z. Li, and C.-W. Nan, Adv. Mater. **23**, 1062 (2011).

[10] J. P. Velev, S. S. Jaswal, and E. Y. Tsymbal, Philos. Trans. R. Soc. A **369**, 3069 (2011).

[11] E. Dagotto, T. Hotta, and A. Moreo, Phys. Rep. **344**, 1 (2001).

[12] C. H. Ahn, J. M. Triscone, and J. Mannhart, Nature **424**, 1015 (2003).

[13] X. Hong, J.-B. Yau, J. D. Hoffman, Y. Bason, L. Klein, and C. H. Ahn, Phys. Rev. B **74**, 174406 (2006).

[14] J. D. Burton and E. Y. Tsymbal, Phys. Rev. B **80**, 174406 (2009).

[15] V. Garcia, M. Bibes, L. Bocher, S. Valencia, F. Kronast, A. Crassous, X. Moya, S. Enouz-Vedrenne, A. Gloter, D. Imhoff, C. Deranlot, N. D. Mathur, S. Fusil, K. Bouzehouane, and A. Barthélémy, Science **327**, 1106 (2010).

[16] C. H. Ahn, A. Bhattacharya, M. D. Ventra, J. N. Eckstein, C. D. Frisbie, M. E. Gershenson, A. M. Goldman, I. H. Inoue, J. Mannhart, A. J. Millis, A. F. Morpurgo, D. Natelson, and J.-M. Triscone, Rev. Mod. Phys. **78**, 1185 (2006).

[17] C.-G. Duan, J. P. Velev, R. F. Sabirianov, Z. Zhu, J. Chu, S. S. Jaswal, and E. Y. Tsymbal, Phys. Rev. Lett. **101**, 137201 (2008).

[18] J. M. Rondinelli, M. Stengel, and N. A. Spaldin, Nat. Nanotechnol. **3**, 46 (2008).

[19] M. K. Niranjan, J. D. Burton, J. P. Velev, S. S. Jaswal, and E. Y. Tsymbal, Appl. Phys. Lett. **95**, 052501 (2009).

[20] C. A. F. Vaz, J. Hoffman, C. H. Ahn, and R. Ramesh, Adv. Mater. **22**, 2900 (2010).

[21] C. A. F. Vaz, J. Hoffman, Y. Segal, J. W. Reiner, R. D. Grober, Z. Zhang, C. H. Ahn, and F. J. Walker, Phys. Rev. Lett. **104**, 127202 (2010).

[22] H. Lu, T. A. George, Y. Wang, I. Ketsman, J. D. Burton, C.-W. Bark, S. Ryu, D. J. Kim, J. Wang, C. Binek, P. A. Dowben, A. Sokolov, C.-B. Eom, E. Y. Tsymbal, and A. Gruverman, Appl. Phys. Lett. **100**, 232904 (2012).

[23] K. J. Choi, M. Biegalski, Y. L. Li, A. Sharan, J. Schubert, R. Uecker, P. Reiche, Y. B. Chen, X. Q. Pan, V. Gopalan, L.-Q. Chen, D. G. Schlom, C. B. Eom, Science **306**, 1005 (2004).

[24] A. Gruverman, D. Wu, H. Lu, Y. Wang, H. W. Jang, C. M. Folkman, M. Y. Zhuravlev, D. Felker, M. Rzchowski, C.-B. Eom, and E. Y. Tsymbal, Nano Lett. **9**, 3539 (2009).

[25] P. Giannozzi, S. Baroni, N. Bonini, M. Calandra, R. Car, C. Cavazzoni, D. Ceresoliet, G. L. Chiarotti, M. Cococcioni, I. Dabo et al., J. Phys.: Condens. Matter **21**, 395502 (2009).

[26] H. Lu, X. Liu, J. D. Burton, C.-W. Bark, Y. Wang, Y. Zhang, D. J. Kim, A. Stamm, P. Lukashev, D. A. Felker, C. M. Folkman, P. Gao, M. S. Rzchowski, X. Q. Pan, C.-B. Eom, E. Y. Tsymbal, and A. Gruverman, Adv. Mater. **24**, 1209 (2012).

Chapter 10

Summary and Future Work

10.1 Summary

The work presented in this dissertation is mainly focused on the study of ferroelectric heterostructures using scanning probe mictroscopy (SPM) techniques. It can be classified into three parts: (i) polarization-coupled resistive switching behavior in ferroelectric tunnel junctions (FTJs), (ii) mechanical switching of ferroelectric polarization in ultrathin ferroelectrics and ferroelectric heterojunctions, and (iii) magnetoelectric coupling in ferroelectric/ferromagnetic heterostructures.

In the first part, we have successfully demonstrated the correlation between ferroelectric polarization orientation and the tunneling conductance—the tunneling electroresistance (TER) effect. We have investigated three different methods for enhancement of polarization retention in FTJs: (i) interface engineering for modification of atomic termination sequences, (ii) use of metal electrodes for more effective screening of depolarizing field, and (iii) interface engineering by introducing a polar molecular layer at the electrode-ferroelectric interface.

Stable and switchable ferroelectric polarization has been achieved in all these

structures, demonstrating a feasibility of operational FTJ devices for practical applications in ferroelectric memory and logic devices. Moreover, we have demonstrated not only bistable, but continuously tunable resistance states in $Co/BaTiO_3/(La,Sr)MnO_3$ tunnel junctions—an effect referred to as memristive behavior. The observed memristive behavior is attributed to the field-induced charge redistribution at the ferroelectric/electrode interface, resulting in the modulation of the interface barrier height. Also, we have demonstrated enhancement of the TER effect by using an interfacial polar layer at the graphene/ferroelectric interface.

Next, we have demonstrated that the strain gradient generated by an ultra-sharp AFM tip could be used to switch the ferroelectric polarization in the ferroelectric film due to the flexoelectric coupling between polarization and strain gradient. Voltage-free control of ferroelectric polarization thus becomes possible. We also showed that pure mechanical force can be used to control resistive switching in FTJs, which represents a new paradigm for voltage-free control of electronic properties of nanoscale ferroelectrics and, more generally, complex oxide materials.

Finally, we have demonstrated that the field effect of ferroelectrics could be used to tune the magnetic properties of a ferromagnetic film. Magnetoelectric coupling between ferroelectrics and ferromagnetics are of interests for potential applications in voltage control of magnetism or vice versa. We showed a large (>10%) modulation of magnetization in the ferromagnetic layer upon ferroelectric polarization reversal in $BaTiO_3/(La,Sr)MnO_3$ heterostructures.

10.2 Future Work

10.2.1 Ferroelectric tunnel junctions

Development of novel electronic devices and memories requires high efficiency, high density, high operation frequency, long retention and low energy consumption. There is still a long way to go to achieve optimal performance in a real device FTJs. The resistance states of the FTJs rely on the polarization states of the ultrathin ferroelectric barriers. To optimize the operational speed of the FTJ, polarization switching dynamics need to be further investigated in a device structure FTJ. Polarization switching dynamics in hundred-nm-thick ferroelectric capacitors have been investigated by means of PFM at the sub-100 ns time range. However, in FTJs, the ferroelectric film has a thickness of only several nanometers and leakage current due to electron tunneling becomes a critical problem for polarization switching. Investigation of the switching dynamics and ultimate speed with which electroresistace effect can be realized represent a scientifically rich and technologically important research direction.

Polarization relaxation is another issue in realization of the FTJ devices. Memory applications generally require data retention over several years. The effective screening of the depolarizing field in ultrathin ferroelectric films and polarization stability become a serious challenge in FTJs and require further studies.

Another direction is development of ferroelectric tunnel memristors (FTMs) where tunable and programmable resistance states can be realized. FTMs can be realized in two ways: polarization controlled FTMs and interface controlled FTMs. For the first type, the high and low resistance states in an FTJ are controlled by the gradual changes in the fraction of switched polarization. Partially switched polarization generates an intermediate resistance state between high and low resistance states.

For the second type, resistance tuning is controlled by charge accumulation at the ferroelectric/electrode interface. Investigation of the role of interface is crucial for realizing programmable FTM devices.

10.2.2 Mechanical polarization switching

The polarization switching dynamics might be fundamentally different for voltage controlled and mechanically controlled processes. Investigation of the mechanical force induced polarization switching dynamics provides a way for understanding the flexoelectric effect at the nanoscale. We have only shown in this dissertation that mechanical writing generates much smaller domains. Spatial and temporal scaling of mechanical switching requires further studies.